Molecular Templating Growth of Silicon Phthalocyanine Based Organic Thin Film Transistors

By

Raluchukwu Ewenike

Thesis Submitted to The University of Ottawa in Partial Fulfillment of The Requirements for The
Master of Applied Science in Chemical Engineering

Chemical and Biological Engineering
Faculty of Engineering
University of Ottawa

MASc in Chemical Engineering (2024)

FACULTY: Faculty of Engineering

DEPARTMENT: Chemical and Biological Engineering

INSTITUTION: University of Ottawa

TITLE: Molecular Templating Growth of Silicon Phthalocyanine Based Organic Thin Film Transistors

AUTHOR: Raluchukwu Berkley Ewenike, BASc. (Chemical Engineering)

SUPERVISOR: Dr. Benoît H Lessard, P.Eng., M.Eng., Ph. D

PAGES : 120

Abstract

Molecular template growth (MTG) has recently shown to be a promising method for the fabrication of highly crystalline semiconductor films by enabling precise control over film properties such as the growth morphologies, molecular orientation, surface properties and crystallinity. The use of para-sexiphenly (*p*-6P) has already been shown in literature as a promising template for the fabrication of high-quality disk-like metal phthalocyanines (MPcs) while showing improved device performance when incorporated into the organic thin film transistor (OTFTs). Silicon phthalocyanines (R_2-SiPc) are a class of MPc that has axial groups which make it deviate from the traditional disk like morphology, and therefore new template molecules may be required for MTG. In this thesis we explore the use of novel molecules as template layers in the development of R_2-SiPc based OTFTs. We begin by implementing a fully fluorinated *p*-6P (*p*-6PF) as a template layer for the fabrication of bis (pentafluoro phenoxy) silicon phthalocyanine (F_{10}-SiPc) OTFTs. This template layer was selected to target the fluorine-fluorine interaction between the semiconductor and the dielectric interface. First, we optimized device performance by varying the deposition conditions of the template. After which we further characterized F_{10}-SiPc on *p*-6P and *p*-6PF where we show that *p*-6PF is a superior template material for the fabrication of R_2-SiPc. Next, we incorporated F_{10}-SiPc on a range of surface including bare SiO_2, *p*-6PF, *p*-6P and 4 novel template layers that were synthesized to deviate from the traditional *p*-6P by providing a varying degree of fluorination and structural shapes. This was done to investigate the influence of the structural properties of the template layer on resulting OTFTs performance. We perform characterization of the films using grazing incident wide angle x-ray scattering and polarized Raman microscopy to quantify the molecular orientation of the F_{10}-SiPc relative to substrate as a function of template layer. Overall, this thesis shows the need for carefully material selection, paring and optimization of template deposition condition in other to yield high performance in OTFTs.

Abstrait

La croissance de modèles moléculaires (MTG) s'est récemment révélée être une méthode prometteuse pour la fabrication de films semi-conducteurs hautement cristallins en permettant un contrôle précis des propriétés des films telles que les morphologies de croissance, l'orientation moléculaire, les propriétés de surface et la cristallinité. L'utilisation du para-sexiphenly (*p*-6P) a déjà été démontrée dans la littérature comme un modèle prometteur pour la fabrication de phtalocyanines métalliques en forme de disque (MPcs) de haute qualité, tout en montrant des performances améliorées du dispositif lorsqu'elles sont incorporées dans le transistor à couches minces organiques (OTFT). Les phtalocyanines de silicium (R_2-SiPc) sont une classe de MPc qui possède des groupes axiaux qui la font diverger de la morphologie traditionnelle en forme de disque, et par conséquent de nouvelles molécules modèles peuvent être nécessaires pour le MTG. Dans cette thèse, nous explorons l'utilisation de nouvelles molécules comme couches modèles dans le développement d'OTFT basés sur R_2-SiPc. Nous commençons par mettre en œuvre un *p*-6P entièrement fluoré (*p*-6PF) comme couche modèle pour la fabrication d'OTFT de bis (pentafluorophénoxy) silicium phtalocyanine (F_{10}-SiPc). Cette couche modèle a été sélectionnée pour cibler l'interaction fluor-fluor entre le semi-conducteur et l'interface diélectrique. Tout d'abord, nous avons optimisé les performances du transistor en faisant varier les conditions de dépôt de les molécules. Après quoi, nous avons caractérisé le F_{10}-SiPc sur *p*-6P et *p*-6PF, où nous montrons que le *p*-6PF est un matériau modèle supérieur pour la fabrication de R_2-SiPc. Ensuite, nous avons incorporé du F_{10}-SiPc sur une gamme de surfaces comprenant du SiO_2 base, *p*-6PF, du *p*-6P et 4 nouvelles couches modèles qui ont été synthétisées pour s'écarter du *p*-6P traditionnel en fournissant un degré variable de fluoration et de formes structurelles. Cela a été fait pour étudier l'influence des propriétés structurelles de la couche modèle sur les performances des OTFT résultants. Nous effectuons la caractérisation des films en utilisant la diffusion rasante des rayons X à grand angle et la microscopie Raman polarisée pour quantifier l'orientation moléculaire du F_{10}-SiPc par rapport au substrat en fonction de la couche modèle. Dans l'ensemble, cette thèse montre la nécessité d'une

sélection minutieuse des matériaux et d'une optimisation des conditions de dépôt des modèles pour obtenir des performances élevées dans les OTFT.

Acknowledgments

First, I would express my deepest gratitude to my supervisor Dr. Benoît Lessard who accepted me as an undergraduate student and allowed me to pursue my graduate studies. I am grateful for all this all his encouragement, advice, support, and brainstorm science doodles that has helped as a student and researcher.

I am also thankful to Benjamin King (now Dr), who mentored and trained me at the beginning of my program. Beyond assisting me physically in the laboratory, I am grateful for his availability whenever I was confused about the concepts of my work. I also extend my thanks to Rosemary Cranston and Halynne Lamontagne for their teaching and responsiveness to my questions.

To the current members and alumni of the Lessard Research Group, some whom I may have never met, I am grateful for the successful laboratory environment you have created, which has enabled me to conduct my research effectively. Special thanks to Joseph Manion for creating a creative, clean, and organized lab space for me and my colleagues. I am thankful for all the collaborators who have contributed synthesis and characterization to aid in my work.

I express my heartfelt gratitude to my family, Juliet, and Felix, Nicole, Warren and Taza. Although it's been seven years since I have been with you physically. Your love and support from afar have meant the world to me. A special thank you goes to Juliet for being the best example in my life. Thank you for your unwavering support and trust in my pursuit of a master’s degree.

Thank you to my thesis committee for your time and consideration of this report.

Table of Contents

List of Figures

List of Tables

List of Key Abbreviations

AFM	Atomic force microscopy
BGTC	Bottom-gate top-contact
CuPc	Copper phthalocyanine
F_{10}-SiPc	Bis(pentafluorophenoxy) silicon phthalocyanine
F_{16}-CuPc	Hexadecylfluoro copper phthalocyanine
GIWAXS	Grazing-incidence wide-angle X-ray scattering
$I_{on/off}$	On/off current
I_{SD}	Source-drain current
MISFETs	Metal-insulated -semiconductor field-effect transistors
MOSFETs	Metal-oxide -semiconductor field-effect transistors
MPcs	Metal phthalocyanines
MTG	Molecular template growth
OLEDs	Organic light emitting diodes
OPVs	Organic photovoltaics
OSCs	Organic semiconductors
OTFTs	Organic thin film transistor
OTS	Octyl(trichloro) silane
p-6P	Para-sexiphenyl
p-6PF	Per fluorinated para-sexiphenyl
PVD	Physical vapor deposition
PXRD	Powder X-ray diffraction
R_2SiPc	Silicon phthalocyanine
SAM	Self-assembled monolayer
SiO_2	silicon dioxide
TFTs	Thin film transistor
TGA	Thermogravimetric analysis
V_{GS}	Gate-source voltage
V_{GS}	Source-drain voltage
V_T	Threshold voltage

WEG	Weak epitaxial growth
XRD	X-ray diffraction
γ^d	Dispersive component of the surface energy
γ^p	Polar component of the surface energy
γ^{tot}	Total surface energy
μ	Field effect mobility
μ_e	Electron field effect mobility
μ_h	Hole field effect mobility

Chapter 1. Introduction

1.1 Overview

Organic electronics are devices which are fabricated using carbon-based semiconductor.[1,2] Organic electronics have gained significant interest both industrially and academically with the development of organic light emitting diodes (OLEDs) by Van Skyle and Ching Tan Wang in 1987 who effectively demonstrated the emission of light from a thin film using low voltage.[3] Several other organic electronic applications have also received increasing attention such as organic photovoltaics (OPV)[4,5] and organic thin film transistors (OTFTs)[6] as they present a potential for low energy manufacturing, light weight and flexible electronic devices, which is challenging with conventional silicon based electronics.[7–9] OTFTs are very similar to traditional metal-insulated-semiconductor field-effect transistors (MISFETs) where they act as logic gate operators or electrical binary switch. OTFTs are basic electrical elements which are used from simple to complex circuits and some recent examples are their use in electronic paper[10], sensors[11,12], radio frequency identification cards[13] (RFIDs). As sensors, OTFTs have been used for the detection of chemical and biological analytes such as humidity[14], tetrahydrocannabinol[3215] (THC), cannabidiol[16] (CBD), carbon dioxide[17] (CO_2), ammonia[18] (NH_3), deoxyribonucleic acid[19] (DNA) and more.

Although OTFTs are a very promising technology they are far from replacing conventional MISFETs in modern day electronic device such as laptops and computers. One of the major reasons is that state of the art OTFTs can not be operated at high enough switching speeds and do not possess enough charge carriers as inorganic semiconductors.[20,21] In addition to increased absolute performance there is also a need to increased device consistency; the consistent manufacturing of OTFTs is challenging as even the smallest changes in molecular structure lead to significant fluctuation in electrical characteristics. Interface engineering between various functional layers has proven to be a reproducible way to control and improve the performance and reliability of OTFTs based electronic devices.[2,22–25]

This is because the interface of the layers in these organic electronic devices play a crucial role in the transfer/transport of charges within the homogenous layers or

adjoining interfaces. The goal of this thesis is therefore to develop high performance OTFTs through the design of novel interfacial materials and films.

1.2 Organic Thin Film Transistors

An OTFT is a three terminal device that has four functional materials which can be arranged into different geometries and architectures as required by the manufacturing challenges or the final application.[26] **Figure 1.1** shows the device architecture of a bottom-gate top contact (BGTC) OTFT which is the primary structure used in this thesis and the operational input and output signals used in an OTFT. When a bias is applied across the source and drain electrode we observe an injection, transport, and extraction of charges between the source and the drain electrode through the organic semiconductor. The charge transport does not take place (negligible amount of current is flowing) when the device is "off". As a gate-source voltage bias (V_{GS}) is applied an electric field polarizes the dielectric/gate insulator layer which leads to the accumulation of charge carriers at the interface. At a critical $V_{GS,}$ known as the threshold voltage (V_T), there is enough carriers at the interface leading to a flow of current (I_{SD}) between the source and the drain. This allows the V_{GS} to be used as a tool in controlling the accumulation of charge carries that can be used in the OTFT. The dielectric layer is also responsible for the insulation of the semiconductor from the gate electrode to avoid current leakage from the gate to the OSC.[27,28]

The operation of OTFTs can be split into two modes of operation which are commonly named as the enhancement mode (device is considered "off" at $V_{GS} = 0$) and depletion mode (device is considered "on" at $V_{GS} = 0$). The use of enhancement mode TFTs is more predominant over the depletion mode because in depletion mode the device is always switched on leading to more power consumption and would typically require a higher V_{GS} to turn off the device.[29] The V_{GS} can be used to control the charge transfer type of the OTFT, the use of a positive (+) bias for the V_{GS} and V_{SD} will lead to a *n*-type transistor (electron transfer) and the use of a negative (-) voltage bias will leading to a *p*-type transistor (electron transfer). However, the semiconductor materials ability to transfer either holes or electron depends on its molecular structure. Most organic semiconductors are better when used in *p*-type operation, others when used in *n*-type operation, and less

commonly observed, some materials can perform ambipolar charge transfer (holes and electrons) working in both *p* and *n*-type operation.[30,31] Most reported organic semiconductors demonstrate predominantly *p*-type operation, this is due to the inherent instability of *n*-type performance which involves a material with available delocalized electrons which are susceptible to reactions with oxygen and moisture in the air.[32,33] Hence significant research efforts are focused on the development and synthesis of new molecules for stable n-type performance in air.[34,35] While *p*-type operation is less susceptible to air and moisture, it does not mean its impervious, this is why OTFTs characterized in air versus oxygen free environment such as a nitrogen or argon filled glovebox will influence the performance.[36]

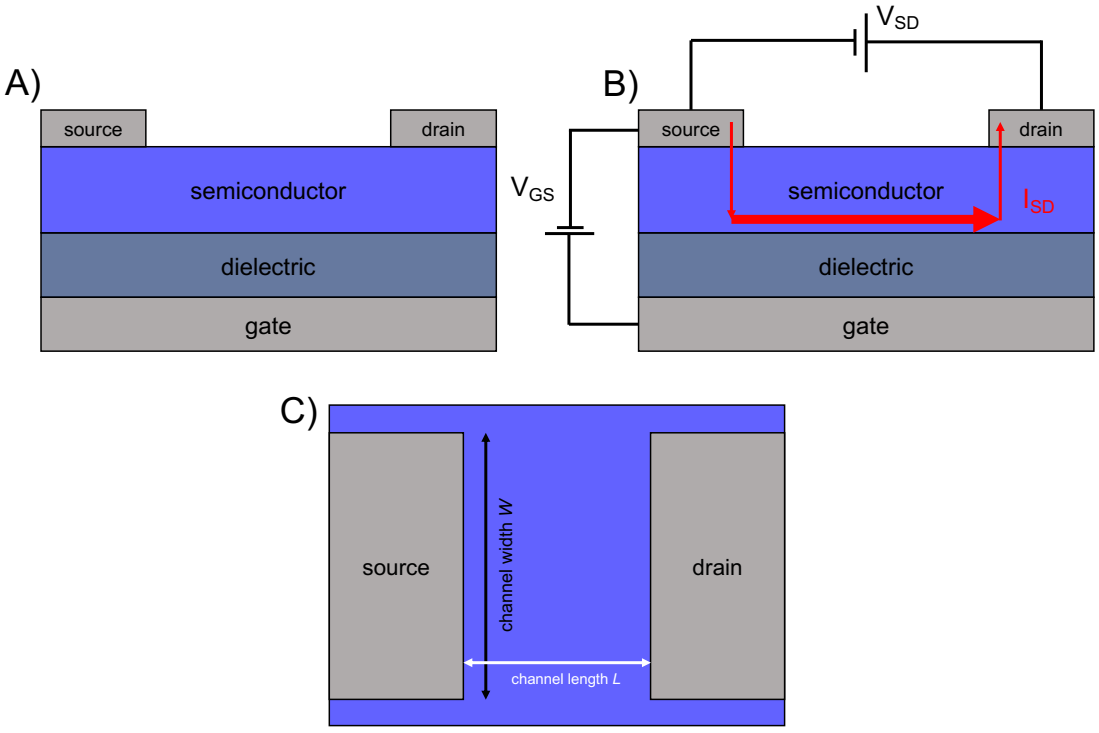

Figure 1.1. *Schematic diagram of the cross-sectional view of a A) bottom-gate top-contact (BGTC) organic thin film transistor (OTFTs). B) Diagram of the operation of an OTFT, where the source drain voltage (V_{SD}) and gate source voltage (V_{GS}) is used to transfer the output signal current (I_{SD}) – the output signal is controlled with the input signal the gate source voltage that creates an electric field in the dielectric layer. C) Top view of an OTFT showing the definition of channel length (L) and width (W).*

1.2.1 Electrical Characterization of OTFTs

The development of OTFTs has brought a need for researchers to characterize and compare the effectiveness of devices fabricated around the world.[37] As TFTs are an integral part of the circuit that are currently used in modern day electronics such as computer, laptops and phones it is important to measure the advantage of using specific semiconductors or device structures over another. OTFT are commonly characterized electrically using the compact direct current (DC) MOSFET model.[30] This is a model that is used for the characterization of MOSFETs however due to the similar operational behaviour this model has been adopted in the for the characterization of OTFTs. Although it is important to note that the performance of an OTFT is also affected by factors such as field effect dependent mobility (μ), current leakage[38], contact resistance[39], charge traps[40], OSC/dielectric interface chemistry[41,42], and device architecture[43,44], which make the use of the MOSFET model a good initial characterization but not ideal.

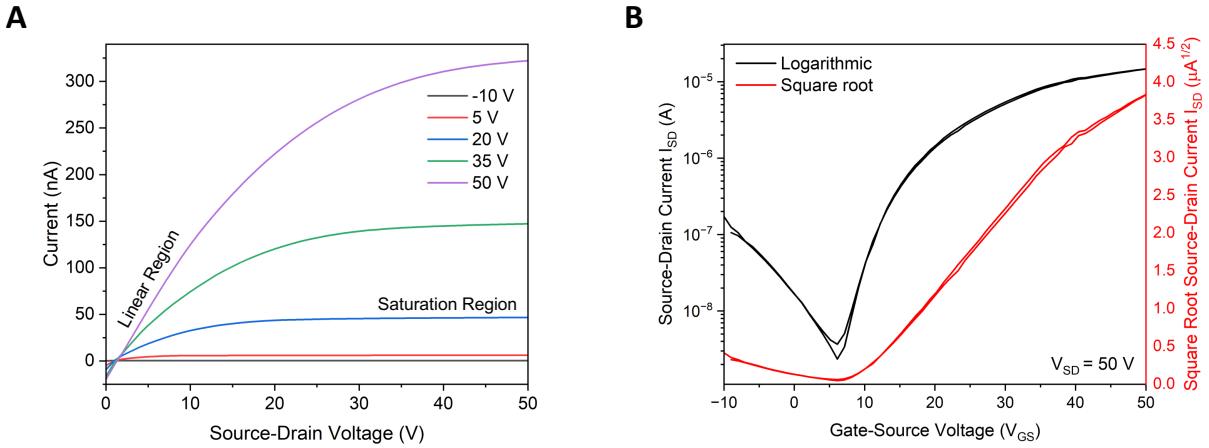

Figure 1.2. *Sample output curve of A) BGTC F_{10}-SiPc OTFT obtained by sweeping V_{SD} from (0 to 50 V) and holding a constant V_{GS} at intervals of 10 V from (-10 to 50 V). B) Sample transfer curve BGTC F_{10}-SiPc OTFT obtained by sweeping V_{GS} from (-10 to 50 V) and holding a constant V_{GS} at 50 V. The black line shows the transfer curve on a logarithmic scale and the red line shows the linearize transfer curve line and used to estimate V_T and μ.*

Other models have been proposed to account for the non-ideal behaviour of OTFTs such as the change drift model that accounts for the fact that the field-effect mobility is overestimated due to the override gate voltage bias (V_{GS}) hence the terms "field effect".[30,45] In a recent study, Dallaire et al. introduced a novel Organic Virtual-

Source Emission Diffusion (OVSED) model for predicting the behavior of n-type semiconductors, specifically poly{[N,N′-bis(2-octyldodecyl)-naphthalene-1,4,5,8-bis(dicarboximide)-2,6-diyl]-alt-5,5′-(2,2′-bithiophene)} (P(NDI2OD-T2)). To address this, various metallic interlayers, such as chromium and manganese with different thickness, were incorporated between the semiconductor and gold contacts during fabrication. Among these interlayers, a 10 nm thick manganese interlayer demonstrated optimal device performance, exhibiting the lowest contact resistance. The study shows superiority of OVSED model over the MOSFETs model, in using V_G and gate-dependent contact resistance (R_C), to accurately characterize and estimate device transfer characteristics.

The use of these models allows for the estimation of electrical performance parameters that are typically used to compare and characterize the OTFTs such as the μ, V_T and on/off current ratio ($I_{on/off}$). The μ is defined as the charge carrier velocity per unit of electric field (cm^2/Vs). This can be further be interpreted as how fast the charge carrier (either hole or electron) can be transported through the semiconductor from the source to the drain electrode. High V_{GS} is typically required for TFTs that are being used for electronics because this allows them to process information and data at a faster speed hence the term “processing speed”.[30] The V_T is minimum voltage required to switch on a transistor for an enhancement mode operating an OTFT and for a depletion mode operation this would be the maximum voltage required to switch off the transistor. In the enhancement mode operation, the V_T is the voltage at which the electric field applied in the dielectric as accumulated enough chargers at the interface of the semiconductor/dielectric to allow charge to flow through the organic semiconductor. This parameter can be seen as the switch for the device hence the ability to control the operation of the device is highly dependent on this parameter. This parameter is also highly affected by factors such as the dielectric material being used (inorganic or organic), dielectric surface treatment, channel length (L), the capacitance and thickness of the dielectric layer.[46–48] The $I_{on/off}$ is described as the ratio of current in the on state to the off state and is typically reported in an order of magnitude (10^X). These common electrical parameters are commonly used to described an OTFT superior, if this has a higher μ, lower V_T or higher $I_{on/off}$.

The estimation of these electrical parameters is typically determined with the use of the characterization curves such as output and transfer curves. **Figure 1.2** shows a typical output curve and transfer curve of an n-type OTFT. The output curve is obtained by sweeping the V_{SD} and holding a constant V_{GS} at different values. The output curve of an OTFT can be separated in two regions which are the linear and saturation region. In the linear regime the OTFTs is acting like a variable resistor where and increase in V_{SD} results in a proportional increase in the potential/current (I_{SD}) in the device. In the saturation region of the OTFT operation, further increase in the V_{SD} does not lead to an increase in the I_{SD} in the device. The pinching-off state is the transition between the saturation region and the linear region and its where $V_{SD} = V_{GS} - V_T$..[49] (**Figure 1.1**. **Figure 1.2 (A)** also shows the non-ideal behaviour of an OTFTs due to gate current leakage leading the output curve to have non-zero output current although the output V_{SD} is current at zero.

The use of compact DC MOSFET model helps in estimating the μ, V_T, *and* $I_{on/off}$ from the transfer curve. The MOSFET model expresses the linear and saturation regime in the transfer curve using **Equation 1.1** and **1.2** respectively.

$$I_{SD} = \frac{W}{L}\,\mu\,C_i\left((V_{GS} - V_T)\,V_{SD} - \frac{V_{SD}^2}{2}\right); Linear\ region\ (V_{SD} < V_{GS} - V_T) \qquad \textbf{Equation 1.1}$$

$$I_{SD} = \frac{W}{2\,L}\,\mu\,C_i\,(V_{GS} - V_T)^2; Saturation\ region\ (V_{SD} \geq V_{GS} - V_T) \qquad \textbf{Equation 1.2}$$

Where W and L are the channel width and length (**Figure 1.1**) and C_i represent the capacitance density of the dielectric layer per unit area. The V_T can be estimated using the x-intercept of the linearized transfer curve for the linear and saturation region using **Equation 1.3** and **1.4** respectively. μ can be estimated from both the linear and saturation region which can be estimated using the slope of the linearized transfer curve. However, depending on the region, μ can be estimated using **Equation 1.5** and **1.6** for the linear and saturation region, respectively.

$$V_T = V_{SD}\,(x\ intercept) - \frac{V_{SD}}{2}; Linear\ region \qquad \textbf{Equation 1.3}$$

$$V_T = V_{SD}\,(x\ intercept); Saturation\ region \qquad \textbf{Equation 1.4}$$

$$\mu = \frac{L}{W\, C_i\, V_{DS}} \cdot \frac{d\sqrt{I_{SD}}}{dV_{GS}}; Linear\ region$$ ***Equation 1.5***

$$\mu = \frac{2\,L}{W\, C_i} \cdot \frac{d\sqrt{I_{SD}}}{dV_{GS}}; Saturation\ region$$ ***Equation 1.6***

1.2.2 Charge Transport in Organic Semiconductor

The ability of carbon-based semiconductor to transfer a charge through molecules is inherently different from traditional semiconductors. The ability for conjugated polymer and small molecules to act as a semiconductor is due to the presence of the sp^2-hybridised linear carbon chains with a sp^2-$2p_z$ configuration for double bonds. **Figure 1.3 (A)** shows the sp^2 hybridization of two carbon atoms and the bonding of p_z orbitals. The overlapping of the p_z orbital form a π bond and the alignment of π bond within molecules of the same compounds is known as π-π bond alignment of the molecules. The delocalized electron density surrounding the molecular planes are primarily responsible for the transport of charger with the molecules. This is why the better alignment of the π-π bonds in the organic semiconductors in a vertical or horizontal orientation leads to better charge transfer properties in OLEDs and OTFTs, respectively. **Figure 1.3 (B)** shows how by increasing the amount of p_z orbital leads to increased amount of energy states which has the consequence of reducing the energy gap between the occupied and unoccupied energy levels. Electrons with the highest energy in the ground state occupied the highest occupied molecular orbital (*HOMO*) and excited electrons with the lowest energy occupy the lowest unoccupied molecular orbital (*LUMO*). The difference in the energy level between the HOMO and LUMO is referred to the energy gap (E_g). The HOMO and LUMO are analogous to the conduction and valance band as commonly referred to in inorganic semiconductors.

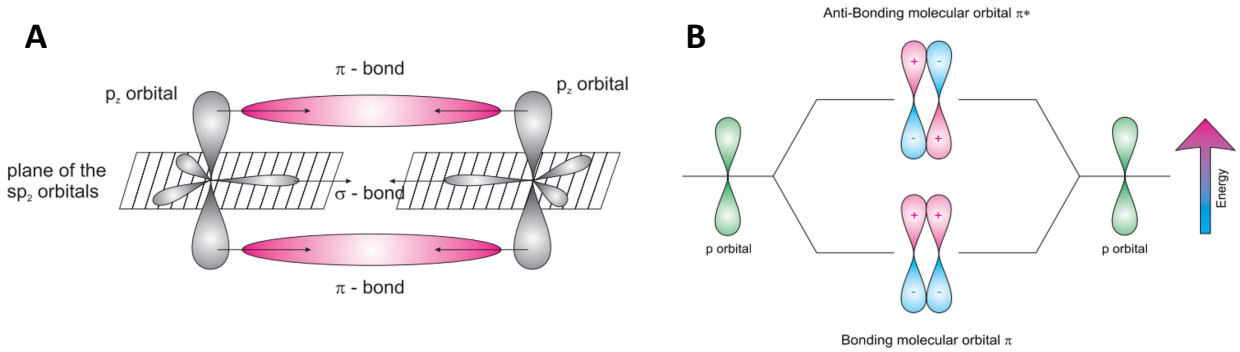

Figure 1.3. *Diagram of the A) sp^2 hybridization of two carbon atoms and B) Bonding of p_z orbitals. Figures adapted from Reference 37 Copyright The institution of Engineering and Technology 2017.*

The movement of charge through molecules occurs through the transfer of energy and spatial shifts among various molecular states, as charges move from one molecule to another. Energy levels are spatially distributed within the molecules of an organic semiconductor, creating a transport resistance or barrier that charge carriers must overcome through tunneling in order for transport to take place. Charge carriers within the semiconductor exhibit strong interactions with the molecule itself and any defects present in the semiconductor film, such as surface roughness, doping density, dipole formation, growth morphological disorders, and chemical impurities. These interactions significantly impact charge transport within the organic semiconductor and are typically managed through modifications to the dielectric/semiconductor interface.

The influence of an insulator extends beyond merely affecting the morphology of an active layer due to the polarization effect. It profoundly influences the distribution of charge carriers, surface potential, and the motion of carriers within the conducting channel. Researchers have established various relationships between modifying the characteristic features of the dielectric/semiconductor interface and the resulting device performance. The engineering of the dielectric/semiconductor interface will be further discussed in **Section 1.4**.

1.3 Metal Phthalocyanine as OSCs

Metal phthalocyanines (MPc) are organic dye molecules discovered in 1907 by accident at South Metropolitan Gas Company in London. The first patent for the compound was issued to Dandridge Drescher and Thomas of Scottish Dyes Ltd in 1929.

The vibrant blue to green colour of the compounds has allowed them to be historically used as the pigments, inks, and dyes for the colouring of clothes, paints, and plastics.[50,51]. MPcs also exhibit excellent chemical, mechanical and thermal stability which has facilitated their commercial production over the years and expanded their applications.[52] The chemical structure of a metal phthalocyanines (MPcs) consist of a metal/metalloid central atom chelated by four isoindole groups connected with nitrogen atoms. **Figure 1.4** shows the chemical structure of an MPc highlighting the central atom (M) and the reactive sites (peripheral position (R_1), bay position (R_2) and axial position (R_3)). The oxidation state of the central atom defines whether there are 0,1 or 2 axial bonds. The combination of over 70 central metal/metaloid atoms and the 16 reactive sites allows for a variety of MPc complexes with different physical and chemical properties. MPcs also have the ability to form highly ordered thin films which has allowed them to be incorporated as semiconductors for the fabrication of organic electronic device such as OPVs, OLEDs and OTFTs.[53–55] Generally, the fabrication of OTFTs with MPcs as the OSC has yielded p-type transistors such as copper phthalocyanine (CuPc), Titanium (IV) oxide phthalocyanine (TiOPc), Magnesium phthalocyanine (MgPc), Lead(II) phthalocyanine (PbPc), Vanadium(IV) oxide phthalocyanine (VOPc), and Tin(II) phthalocyanine (SnPc).[36,56–58]

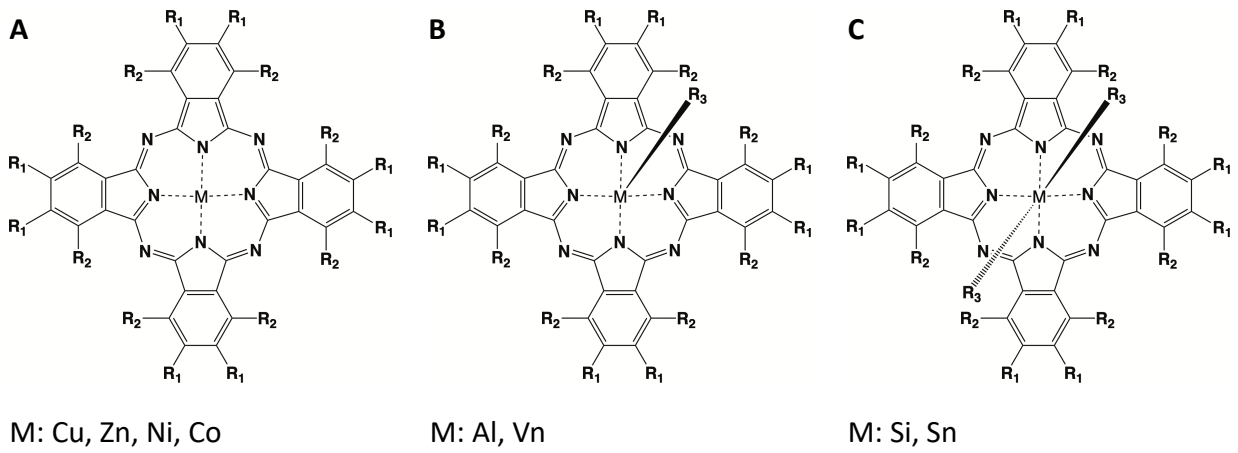

Figure 1.4. *General chemical structures for A) Divalent metal phthalocyanines B) Trivalent metal phthalocyanines and (C) Tetravalent metal phthalocyanines.*

The solubility of MPcs in organic solvents has allowed them to be fabricated through solution processing techniques such as spin coating and blading coating.[59] The reactive site and central atom also play a role in the solubility of the MPc. For instance, bulky peripheral groups or polar substituents can disrupt π-π stacking and enhance solubility by promoting favorable interactions with the solvent molecules.[60,61] Solution processing of small molecules into large area films with uniform thickness and roughness is however very challenging. The thermal stability of MPcs enables the formation of thin films through physical vapour deposition (PVD). PVD is a process where the material is heated under high vacuum ($<10^{-6}$ torr) where it sublimes, and the plume of vapour condenses on the substrate creating a film. The rate of deposition is controlled by controlling the heating power being applied to the source and the thickness of the film is typically measured by a quartz crystal microbalance (QCM). PVD enables the controlled deposition of uniform large area films with predictable roughness and thickness.

1.3.1 Silicon Phthalocyanine

Silicon phthalocyanines (R_2-SiPcs) are MPcs that possess two axial substituents due to the tetravalent nature of the central Si atom. The axial reactive site (R_3) provides advantageous tuning of the molecules leading to functionalization with chemical groups such as silanes, phenols and carboxylic acids leading to changes in the optical and electrochemical properties of the molecule. Additionally, when integrated into OTFTs most R_2-SiPcs preferentially transfer electrons (n-type) which is also unique for an MPc. R_2-SiPc were first incorporated into the fabrication of organic electronics for photovoltaic measurements and after three decades were incorporated as a ternary additive for the fabrication a poly(3-hexylthiophene):phenyl-C61-butyric acid methyl ester (P3HT:PC61BM) bulk heterojunction (BHJ) OPV device where it provided additional absorption at 685 nm and effectively increased the power conversion efficiency (PCE) of the device by 25%.[62] R_2-SiPcs have been used to fabricate of *n*-type and ambipolar OTFTs and have also been incorporated into the fabrication of gas-sensor based OTFTs.[18,25] Melville et al first report of R_2-SiPc as semiconductor in OTFTs where they report the use of a benzoate, 1-napthoate and 9-anthronate axially substituted R_2-SiPcs where they further optimized the dielectric/semiconductor interface and deposition

temperature to yield a maximum of μ_e of 1.2 ×10^{-2} cm^2/Vs with an octadecyl trichlorosilane (ODTS) treated surface where the substrate was heated to 200 ºC during the deposition.[63]

Melville et al also reported the ambipolarity and air stability of using bis (pentafluoro phenoxy) silicon phthalocyanine (F_{10}-SiPc) in the fabrication of OTFTs leading to excellent device μ_e of up to 0.54 cm^2/Vs which was an order of magnitude greater than the F_{16}-CuPc which is one of the most commonly used *n*-type MPc in OTFTs.[64] F_{10}-SiPc has yielded one of the best *n*-type performing R_2-SiPc based OTFTs with average electron mobilities (μ_e) of 0.14 cm^2/Vs and threshold voltages (V_T) of 10.4 V.[25,41]

1.4 Dielectric Semiconductor Interface Engineering

The interface between the dielectric and semiconductor plays an important role in the function and operation of OTFTs. This is primarily because the first 2-6 monolayers of the semiconductor deposited onto the dielectric surface are responsible for facilitating charge transport within the organic semiconductor channel.[65–68] How the semiconductor sticks or starts to grow on the surface will dictate the device parameters such as μ and V_T. Typically, four main methods are used to enhance device performance through modifications to this interface: 1) reduction in charge carrier trap by smoothing dielectric layer; which minimizes conductive paths to the gate electrode,[69] 2) tuning of molecular orientation and packing structure of the semiconductor; by changing of dielectric layer surface energy characteristics,[41,70] 3) use of a low dielectric constant dielectric layer; to minimize dipolar disorder at the interface,[66,71] and 4) use of high carrier concentration through the use of an interfacial monolayer or polymer electrolyte dielectric; to increase the density of charge carriers at the interface.[2,72] Among these approaches, the first two are the most commonly and routinely reported in the literature.

To achieve desired modifications in surface properties of the dielectric layer prior to the deposition of organic semiconductor, self-assembled monolayers (SAMs) serve as an effective tool. It is important to note that SAMs have also found functionality for modification of the electrodes in bottom contact configuration. This is because the semiconductor is also deposited on the source and drain electrodes, so SAM can be used to stop absorption of the organic material into the metal electrodes and to tune the work

function of the metal. A study conducted by Boudient et al.[73] demonstrated the characterization of 10 different SAM-modified source-drain electrodes with n-type semiconductor and N,N-dialkylsubstituted-(1,7&1,6)-dicyanoperylene-3,4:9,10-bis(dicarboximide) derivative (N1400), and two p-type semiconductors, poly[9,9-dioctyl-fluorene co-N-(4-butylphenyl)-diphenylamine] (TFB) and 6,13-bis(triisopropylsilylethynyl) pentacene, where they observed changes in the contact angle and the work function of the metal. They did not find any correlation between the SAM-modified electrode work functions and mobility and attributed the changes in the mobility to be dependent on the semiconductor. However, they were able to find a correlation between the contact resistance and the work function of the electrode for all semiconductors used in the study.[73] SAMs are primarily classified into silane and phosphonic acid (PA)-based molecules. **Figure 1.5** shows the chemical structure of commonly used organosilanes, and PA based SAMs used on SiO_2. Silane-based compounds show a preference for binding with hydroxyl groups on silicon-based dielectric layers, forming Si-O-Si covalent bonds. Conversely, PA-based molecules are better suited for modifying other inorganic dielectric layers, forming P-O-M covalent bonds (where 'M' denotes the metal on the inorganic dielectric).[68]

The processing of SAMs can be achieved through both vapour and solution-based reactions, with reaction conditions playing a pivotal role in determining SAM quality. Various factors such as carbon chain length, as well as functionalization with aromatic rings and fluorenes, contribute to the structure of SAMs, ultimately impacting surface properties, device performance and molecular orientation packing. For example, Walter and co-worker. illustrated the influence of relative humidity on the growth of octadecyltrichlorosilane (OTS) SAMs and its subsequent effect on the surface wettability of the dielectric layer. This resulted in enhanced μ of p-type semiconductor P-BTDT (phenylbenzo[d,d]thieno[3,2-b;4,5-b]dithiophene) within an optimal relative humidity range of 55−60%.[42] In another case, King et al. observed changes in the total surface energy of modified dielectric layers using various SAMs such as OTS, octadecyl(trichlorosilane) (ODTS), trichloro(3,3,3-trifluoropropyl)silane (FPTS), and phenyltrichlorosilane (PhTS). They noted that a closer match in total surface energy between the dielectric layer and the semiconductor resulted in enhanced electron μ for

F_{10}-SiPc based OTFTs. Additionally, the use of OTS resulted in the most improved molecular orientation of F_{10}-SiPc, thereby yielding the best device μ and V_T.[41]

SAM surface modification of dielectrics has proven to be beneficial; however, this method still shows limitations that draws back certain advantages typically associated with organic electronic devices over inorganic counterparts. For instance, the fabrication of highly flexible and stretchable devices necessitates an ultrahigh density of SAMs, which is unattainable through thermodynamic self-assembly processes.[68] To overcome these challenges, polymer dielectrics have been used by researchers to retain these advantages.[74] Polymer dielectrics offer several benefits, including solution processability; facilitating incorporation into roll-to-roll industrial fabrication [75], flexibility, stretchability, biodegradable and biocompatible electronic devices.[76,77] Nevertheless, the use of polymer dielectrics introduces additional complexity into the fabrication of OTFTs. Polymer dielectrics are also influenced by various chemical properties such as glass transition temperature [78], solvent concentration [79], molecular weight [80], and molecular packing.[81] Polymer dielectrics also suffer from the formation of rough film surfaces compared to inorganic dielectrics fabricated using e-beam and sputtering techniques. These factors collectively contribute to the surface properties of the polymer and consequently impacting device performance. In this thesis, surface dielectric modification was performed using a relatively recent technique known as molecular template growth (MTG), employing novel templating molecules, which will be further discussed in Section 1.4.2.

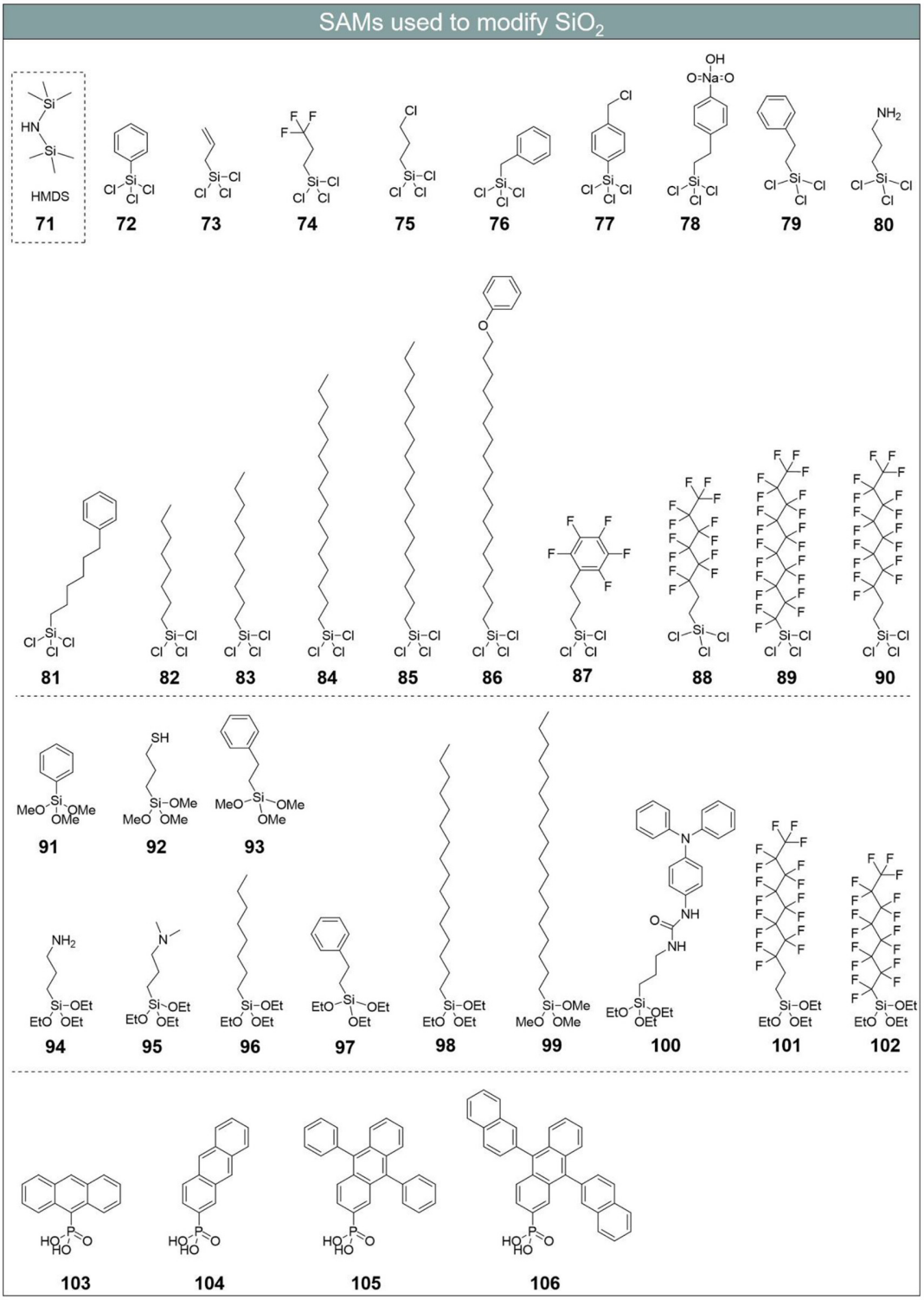

Figure 1.5. *Chemical structure of SAMs used on SiO_2. Most common organosilanes (71-102) and phosphonic acid (PA)-based molecules (103-106). Figures adapted from Reference 56. Copyright American Chemical Society 2020.68*

1.4.2 Molecular Template Growth (MTG)

MTG is a significant advancement in thin film fabrication, offering precise control over molecular properties such as orientation, morphologies, crystallinity, electronic structures, and surface characteristics of thin films. This technique typically involves the PVD of a monolayer or bilayer of organic molecules or inorganic materials onto an amorphous substrate prior to depositing the semiconductor film (overlayer). The four main categories of MTG are used in organic electronics and optoelectronics are graphene/graphene oxide-based, acene-based, perylene-based, and multiphenyl- or multithiophene-based.[82] MTG enables favourable growth of semiconductor films because there is a stronger molecule-molecular π-π interaction compared to interlayer molecule or molecule-substrate interactions. Consequently, these methods offer the flexibility to adjust the primary orientation (π-π stacking) of the semiconductor, either face-on or edge-on, significantly influencing charge transport.[83] **Figure 1.6** shows typical diagrams of an OTFT and vertical organic field effect transistors (VOFETs) with their preferred π-π stacking alignment.

In OTFTs, the preferred orientation for the π-π bonds of the OSC is parallel (edge-on) to the substrate, aligning with the direction of charge transport from the source to the drain electrode. Conversely, for VOFETs, where charge transport occurs perpendicular to the source-to-drain electrode, a face-on orientation of the semiconductor is advantageous for device performance.

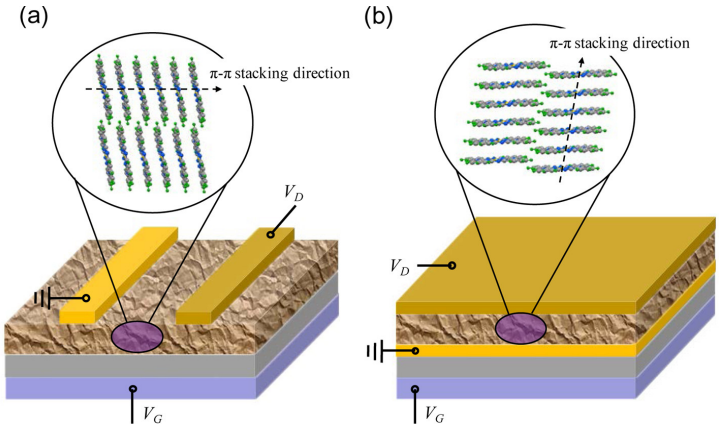

Figure 1.6. *Schematic diagram of an a) OTFT and b) VOFETs with the direction of charge transport and preferred molecular orientation and π-π stacking direction. Figure adapted from Reference 82. Copyright American Chemical Society 2015.*

The use of MTG as a dielectric surface modification tool offers an interplay of various interaction such as molecule−substrate, intermolecular, intramolecular π−π interaction, dipole-dipole interactions. It is crucial to recognize that the growth of the OSC on the template layer can manifest as both in commensurate and incommensurate epitaxial processes.[82] In certain instances, the interaction between the template layer and the overlayer predominantly exhibits a commensurate epitaxial relationship, while in others, an incommensurate epitaxial relationship prevails. This balance of interactions characterizes what is known as weak epitaxial growth (WEG), describing the relationship between both commensurate and incommensurate growth phenomena.

1.4.1 Multiphenyl and Multithiophene Based MTG in OTFTs

WEG typically uses multiphenyl and multithiophene where an ultrathin film of the rod-like molecules is deposited as a template layer for the deposition of rod-like or disklike organic semiconductors.[84] Notably, in literature, sexithiophene (*α*-6P) and para-sexiphenyl (*p*-6P) are frequently utilized as template molecules for WEG of organic semiconductors and metal phthalocyanines (MPcs) (Figure 1.7). The incorporation of these templates has demonstrated significant enhancements in device performance compared to MPcs fabricated directly on bare SiO_2 substrates without any template layer. **Table 1** highlights the improvements observed in the μ and V_T of MPc-based OTFTs fabricated using *p*-6P as a template layer compared to those on bare SiO_2 substrates. Reports have shown that MPc-based OTFTs fabricated with a template layer exhibit superior μ and V_T compared to OTFTs fabricated on surfaces treated with OTS, a well-established surface treatment for OTFT fabrication. For instance, in the study by Song et al.[41] SnOPc/*p*-6P OTFTs demonstrated μ and V_T values of 0.44 cm^2/Vs and 37 V, respectively, outperforming SnOPc OTFTs fabricated on both bare SiO_2 and OTS-treated substrates, which exhibited μ and V_T values of 0.001 cm^2/Vs and 80 V, and 0.07 cm^2/Vs

and 70 V, respectively.[85]

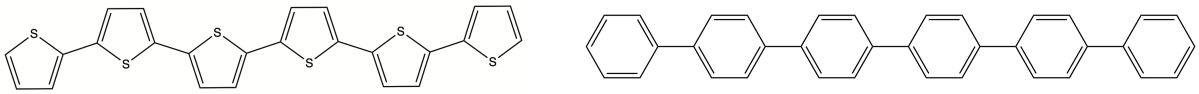

***α*-6P** ***p*-6P**

Figure 1.7. *Chemical Structure of rod-like template layer sexithiophene (α-6P) and para-sexiphenyl (p-6P)*

Table 1.1. *Electrical parameters of MPc OTFTs fabricated using WEG and on bare SiO_2*

		μ (cm^2/Vs)		V_T (V)		
template layer	MPcs	WEG method	bare SiO_2	WEG method	bare SiO_2	ref
p-6P	CuPc	0.1	0.02	– 16.0	– 17.0	86
p-6P	F_{16}-CuPc	0.27	0.042	16.4	7.3	87,88
p-6P	ZnPc	0.32	0.022	~ – 1.0	~ – 1.0	89
p-6P	VOPc	1.0	0.006	~ 9.0	– 14.7	57,90
p-6P	SnOPc	0.4	0.001	37.0	80.0	85

Optimizing the deposition conditions of the template layer is crucial for fabricating highly crystalline semiconductor films, with substrate temperature during deposition and deposition time being the two key factors typically optimized. Altering the substrate temperature during deposition induces significant changes in the growth morphologies of the template layer. The growth process of organic molecules typically involves several steps: (1) nuclei formation, (2) adsorption of new molecules onto nuclei, (3) diffusion and aggregation of adsorbed molecules, and (4) merging of islands.[82] During the diffusion and aggregation step, new molecules tend to locate energetic sites for growth, and changes in substrate temperature alter the available diffusion energy for molecules during this process. Consequently, the domain sizes of the template layer exhibit a direct correlation with temperature.[91] The growth morphology of *p*-6P has been extensively studied in literature. At a substrate deposition temperature of 25 ºC, *p*-6P forms compact-quadrangle islands. As the temperature increases, *p*-6P transitions to compact-polygon islands, followed by the formation of islands with dendritic structures, and ultimately fractal islands.[92] The mechanisms governing the growth morphology of *p*-6P vary at different

temperature ranges. At higher temperatures (> 60°C), growth is primarily controlled by diffusion and aggregation, whereas at lower temperatures (≤ 60°C) this changed. The optimal substrate deposition temperature was found to be 180°C. At this temperature, *p*-6P forms larger domains with lower island densities, facilitating the fabrication of high-quality OSC films.[92]

Changes in the deposition time directly influences the thickness and surface coverage of the template layer. Typically, maximizing the surface coverage of the template on the substrate is preferred to enhance the templating effect on the semiconductor film. However, it's important to note that the growth of the second monolayer commences before the full coverage of the first monolayer, potentially resulting in a less smooth surface, which can adversely affect charge transport in OTFTs.[93]

For example, a study done by Gu et al. investigated CuPc/*p*-6P OTFTs fabricated with varying thicknesses of *p*-6P (0, 0.8, 1.6, 2.4, and 3 monolayers, ML). They observed an increase in μ with increasing thicknesses of *p*-6P; however, a decrease in μ was observed when going from 2.4 ML (μ = 0.184 cm^2/Vs) to 3 ML (μ = 0.063 cm^2/Vs). The study attributed this decrease in μ to the limiting charge transfer properties of *p*-6P, which, at greater thicknesses will behave like a semiconductor.[86] Although it is possible for the template layer to also be a semiconductor that could potentially play a role in charge transport typical the energy level of these material (HUMO and LUMO) are not close to work function of metals and only an ultra-thin layer is required so they have a very negligible role in charge transport in OTFTs.

1.5 Thin Film Characterization

Organic electronics undergoes continuous advancement through the synthesis of novel materials, the design of innovative device structures, the use of various fabrication and processing techniques. This combination techniques and strategies makes it challenging to definitively assert the superiority of one technique or material over another solely based on electrical characterization. Consequently, researchers employ a combination of diverse thin-film characterization techniques to comprehensively understand the properties thin films. These techniques help with the determination of molecular orientation, analysis of film topology and surface roughness, as well as

exploration of micro and nano-scale properties, all of which significantly influence and correlate with the electrical performance of organic electronic devices.

1.5.1 Atomic Force Microscopy (AFM)

AFM is a valuable technique for characterizing thin films, offering insights into surface texture, shapes, and roughness across various materials. AFM operates primarily in two contact modes: contact and tapping. In this thesis, tapping mode AFM was utilized due to its gentler imaging approach, which minimizes potential damage to soft and heterogeneous surfaces like those found in organic semiconductors, self-assembled layers, and polymers.[94] Tapping mode AFM uses a cantilever with a small sharp tip, controlled by a piezoelectric actuator to maintain a constant separation between probes and the sample. By using a consistent resonant frequency, tapping mode AFM intermittently interacts with the sample during imaging, offering significant advantages for imaging organic thin films. Understanding the growth and nucleation of organic films is crucial, typically starting with the first and second monolayers.[95] Investigating various growth morphologies of semiconductors on different dielectric surfaces helps understand the impact of grain boundaries and sizes within OSCs and also help to draw conclusions on the impact of different fabrication conditions, such as temperature, deposition rate, and spin-coating speed, for both thermally evaporated and solution-processed films.[60]

1.5.2 X-ray Scattering

The use of X-ray techniques, such as Powder X-ray Diffraction (PXRD) and Grazing Incidence Wide-Angle X-ray Scattering (GIWAXS), has significantly contributed to advancing our understanding of the crystallographic and chemical properties of thin films. Variations in film fabrication conditions, such as dielectric surface modifications and other fabrication parameters, play a crucial role in influencing thin film crystallinity and, consequently, device performance.[95] These X-ray methods provide non-destructive analysis by irradiating the thin film with an incident X-ray beam and measuring reflection and scattering angles using detectors. PXRD is commonly employed in characterizing OTFTs, offering insights into polycrystalline film structures and crystal sizes.[96] Conversely, synchrotron based GIWAXS has emerged as a valuable tool for probing the nano-scale

film properties, such as crystal orientation, lattice parameters, and relative crystallinity, although requiring significantly higher energy for operation compared to PXRD.[97,98] In summary, these techniques help to analyse variations in crystallinity and structural characteristics, which help in the optimization of thin film-based devices.

1.5.4 Raman Microscopy

Raman microscopy stands as a powerful spectroscopy tool used to analyse the chemical structure, polymorphism, crystallinity, and molecular interactions within thin films. By probing vibrational and rotational frequency modes using lasers within the visible, near-infrared, or near-ultraviolet range, coupled with microscope lenses, this technique offers non-destructive analysis. It uses distinct vibrational modes and assesses their relative intensities, enabling precise characterization.[99,100] Unlike PXRD, Raman microscopy provides insights into local changes within a film, rather than just a local average, offering information on both amorphous and crystalline films. In contrast, XRD primarily offers data on polycrystalline or crystalline films. Polarized Raman microscopy has helped researchers in the analysis of molecular orientation in thin films, particularly for metal phthalocyanines (MPcs) like CoPc, CuPc, ZnPc, and MgPc.[101] Recent advancements, by Cranston et al.[102], showed the first use of polarized Raman microscopy on determining the molecular angle R_2-SiPc films. This study showed the impact of deposition methods and post-deposition thermal annealing on the properties bis(tri-n-propylsilyl oxide) SiPc ((3PS)2-SiPc).[102]

1.6 Scope of Thesis

This thesis will focus on the fabrication and characterization of thermally evaporated BGTC F_{10}-SiPc OTFTs using a range of templating materials with similar structures to that of (*p*-6P) featuring different functional groups and structure shapes. From the beginning to conclusion, the thesis shows the need to carefully select the deposition time, substrate temperature during deposition and the pair of template layer and semiconductor. Additionally, the use of various thin film characterization techniques enables conclusions to be drawn from thin film microstructures to help understand the differing templating effects and electrical performances in OTFTs.

In **Chapter 2**, I examined the use of fluorinated para-sexiphenyl (*p*-6PF) as a template layer for fabricating F_{10}-SiPc OTFTs. This chapter shows primarily the impact of varying deposition condition of *p*-6PF on growth morphology, surface coverage and device performance. Upon optimization F_{10}-SiPc/*p*-6PF OTFTs resulted in similar μ in comparison to the use of an OTS treated surface and superior performance compared to devices fabricated on bare SiO_2 and *p*-6P. The use of AFM, XRD and GIWAXs was used to determine film properties such as the crystallinity, surface roughness and molecular orientation of F_{10}-SIPc film of *p*-6PF. Also, showing the superiority of *p*-6PF as a template layer for R_2-SiPc OTFTs in comparison to *p*-6P. In conclusion this chapter highlights the need to optimize fabrication conditions for any pair of semiconductor and dielectric surface treatment techniques.

In **Chapter 3**, To further show the influence of the choice of template layer and template deposition condition, F_{10}-SiPc OTFTs were fabricated and characterized using six different layers under identical template deposition conditions. The template layer were chosen to possess similar properties to *p*-6P with varying structure shapes that deviate from a linear rod-like molecule and the addition of various functional groups such as different number of fluorine atoms. These template layers help to better understand the relationship between the structure properties of the template layer and device performance. Raman microscopy was used to develop molecular orientation surface maps. Additionally, GIWAXS was also used to validate and characterize the molecular orientation of F_{10}-SiPc films on the different template layers. The results shows that the fluorine-fluorine interactions between the semiconductor and template layer improve the device μ and the use of box structure template layer lead to and significant reduction in device μ and molecular angle of F_{10}-SiPc in respect to the substrate.

In **Chapter 4**, I summarize the main findings and offer suggestions on how WEG could further enhance the development of TFTs. I also discuss ongoing efforts related to organic thin film inverters and the use of WEG for the fabrication of VOFETs.

References

(1) Zhu, H.; Shin, E.; Liu, A.; Ji, D.; Xu, Y.; Noh, Y. Printable Semiconductors for Backplane TFTs of Flexible OLED Displays. *Advanced functional materials* **2020**, *30* (20), 1904588-n/a.
(2) Ma, H.; Yip, H.-L.; Huang, F.; Jen, A. K.-Y. Interface Engineering for Organic Electronics. *Advanced Functional Materials* **2010**, *20* (9), 1371–1388. https://doi.org/10.1002/adfm.200902236.
(3) Forrest, S. R.; Thompson, M. E. Introduction: Organic Electronics and Optoelectronics. *Chem. Rev.* **2007**, *107* (4), 923–925. https://doi.org/10.1021/cr0501590.
(4) Kippelen, B.; Brédas, J.-L. Organic Photovoltaics. *Energy Environ. Sci.* **2009**, *2* (3), 251–261. https://doi.org/10.1039/B812502N.
(5) Faure, M. D. M.; Lessard, B. H. Layer-by-Layer Fabrication of Organic Photovoltaic Devices: Material Selection and Processing Conditions. *Journal of Materials Chemistry C* **2021**, *9* (1), 14–40. https://doi.org/10.1039/d0tc04146g.
(6) Klauk, H. Organic Thin-Film Transistors. *Chem. Soc. Rev.* **2010**, *39* (7), 2643–2666. https://doi.org/10.1039/B909902F.
(7) Fukuda, K.; Takeda, Y.; Mizukami, M.; Kumaki, D.; Tokito, S. Fully Solution-Processed Flexible Organic Thin Film Transistor Arrays with High Mobility and Exceptional Uniformity. *Scientific Reports* **2014**, *4* (1), 3947. https://doi.org/10.1038/srep03947.
(8) Ren, H.; Cui, N.; Tang, Q.; Tong, Y.; Zhao, X.; Liu, Y. High-Performance, Ultrathin, Ultraflexible Organic Thin-Film Transistor Array Via Solution Process. *Small* **2018**, *14* (33), 1801020. https://doi.org/10.1002/smll.201801020.
(9) Azarova, N. A.; Owen, J. W.; McLellan, C. A.; Grimminger, M. A.; Chapman, E. K.; Anthony, J. E.; Jurchescu, O. D. Fabrication of Organic Thin-Film Transistors by Spray-Deposition for Low-Cost, Large-Area Electronics. *Organic Electronics* **2010**, *11* (12), 1960–1965. https://doi.org/10.1016/j.orgel.2010.09.008.
(10) Fujisaki, Y.; Koga, H.; Nakajima, Y.; Nakata, M.; Tsuji, H.; Yamamoto, T.; Kurita, T.; Nogi, M.; Shimidzu, N. Transparent Nanopaper-Based Flexible Organic Thin-Film Transistor Array. *Advanced Functional Materials* **2014**, *24* (12), 1657–1663. https://doi.org/10.1002/adfm.201303024.
(11) Lin, P.; Yan, F. Organic Thin-Film Transistors for Chemical and Biological Sensing. *Advanced Materials* **2012**, *24* (1), 34–51. https://doi.org/10.1002/adma.201103334.
(12) King, B.; Lessard, B. H. Review of Recent Advances and Sensing Mechanisms in Solid-State Organic Thin-Film Transistor (OTFT) Sensors. *J. Mater. Chem. C* **2024**. https://doi.org/10.1039/D3TC03611A.
(13) Rotzoll, R.; Mohapatra, S.; Olariu, V.; Wenz, R.; Grigas, M.; Dimmler, K.; Shchekin, O.; Dodabalapur, A. Radio Frequency Rectifiers Based on Organic Thin-Film Transistors. *Applied Physics Letters* **2006**, *88* (12), 123502. https://doi.org/10.1063/1.2186384.
(14) Yin, M.-J.; Li, Z.-R.; Lv, T.-R.; Yong, K.-T.; An, Q.-F. Low-Voltage Driven Flexible Organic Thin-Film Transistor Humidity Sensors. *Sensors and Actuators B: Chemical* **2021**, *339*, 129887. https://doi.org/10.1016/j.snb.2021.129887.
(15) Comeau, Z. J.; Rice, N. A.; Harris, C. S.; Shuhendler, A. J.; Lessard, B. H. Organic Thin-Film Transistors as Cannabinoid Sensors: Effect of Analytes on Phthalocyanine

Film Crystallization. *Advanced Functional Materials* **2022**, *32* (7). https://doi.org/10.1002/adfm.202107138.
(16) Lamontagne, H. R.; Comeau, Z. J.; Cranston, R. R.; Boileau, N. T.; Harris, C. S.; Shuhendler, A. J.; Lessard, B. H. Chloro Aluminum Phthalocyanine-Based Organic Thin-Film Transistors as Cannabinoid Sensors: Engineering the Thin Film Response. *Sensors & diagnostics* **2022**, *1* (6), 1165–1175. https://doi.org/10.1039/D2SD00071G.
(17) Rullyani, C.; Sung, C.-F.; Lin, H.-C.; Chu, C.-W. Flexible Organic Thin Film Transistors Incorporating a Biodegradable CO2-Based Polymer as the Substrate and Dielectric Material. *Scientific Reports* **2018**, *8* (1), 8146. https://doi.org/10.1038/s41598-018-26585-0.
(18) King, B.; Moorthy, S. G.; Lesniewska, E.; Meunier-Prest, R.; Bouvet, M.; Lessard, B. H. Modulating the Majority Charge Carrier Type and Performance of Organic Heterojunction Ammonia Sensors by Increasing Peripheral Fluorination of the Silicon Phthalocyanine Sublayer. *Sensors and Actuators B: Chemical* **2024**, *408*, 135507. https://doi.org/10.1016/j.snb.2024.135507.
(19) Yan, F.; Mok, S. M.; Yu, J.; Chan, H. L. W.; Yang, M. Label-Free DNA Sensor Based on Organic Thin Film Transistors. *Biosensors and Bioelectronics* **2009**, *24* (5), 1241–1245. https://doi.org/10.1016/j.bios.2008.07.030.
(20) Wang, L.; Yoon, M.-H.; Lu, G.; Yang, Y.; Facchetti, A.; Marks, T. J. High-Performance Transparent Inorganic–Organic Hybrid Thin-Film n-Type Transistors. *Nature Materials* **2006**, *5* (11), 893–900. https://doi.org/10.1038/nmat1755.
(21) Reese, C.; Roberts, M.; Ling, M.; Bao, Z. Organic Thin Film Transistors. *Materials Today* **2004**, *7* (9), 20–27. https://doi.org/10.1016/S1369-7021(04)00398-0.
(22) Liu, D.; Miao, Q. Recent Progress in Interface Engineering of Organic Thin Film Transistors with Self-Assembled Monolayers. *Mater. Chem. Front.* **2018**, *2* (1), 11–21. https://doi.org/10.1039/C7QM00279C.
(23) Aghamohammadi, M.; Rödel, R.; Zschieschang, U.; Ocal, C.; Boschker, H.; Weitz, R. T.; Barrena, E.; Klauk, H. Threshold-Voltage Shifts in Organic Transistors Due to Self-Assembled Monolayers at the Dielectric: Evidence for Electronic Coupling and Dipolar Effects. *ACS Appl. Mater. Interfaces* **2015**, *7* (41), 22775–22785. https://doi.org/10.1021/acsami.5b02747.
(24) Zhang, H.; Guo, X.; Hui, J.; Hu, S.; Xu, W.; Zhu, D. Interface Engineering of Semiconductor/Dielectric Heterojunctions toward Functional Organic Thin-Film Transistors. *Nano Lett.* **2011**, *11* (11), 4939–4946. https://doi.org/10.1021/nl2028798.
(25) Melville, O. A.; Grant, T. M.; Lochhead, K.; King, B.; Ambrose, R.; Rice, N. A.; Boileau, N. T.; Peltekoff, A. J.; Tousignant, M.; Hill, I. G.; Lessard, B. H. Contact Engineering Using Manganese, Chromium, and Bathocuproine in Group 14 Phthalocyanine Organic Thin-Film Transistors. *ACS Applied Electronic Materials* **2020**, *2* (5), 1313–1322. https://doi.org/10.1021/acsaelm.0c00104.
(26) Koch, N. Organic Electronic Devices and Their Functional Interfaces. *ChemPhysChem* **2007**, *8* (10), 1438–1455. https://doi.org/10.1002/cphc.200700177.
(27) Chandar Shekar, B.; Lee, J.; Rhee, S.-W. Organic Thin Film Transistors: Materials, Processes and Devices. *Korean Journal of Chemical Engineering* **2004**, *21* (1), 267–285. https://doi.org/10.1007/BF02705409.
(28) Kumar, B.; Kaushik, B. K.; Negi, Y. S. Perspectives and Challenges for Organic Thin Film Transistors: Materials, Devices, Processes and Applications. *Journal of*

Materials Science: Materials in Electronics **2014**, *25* (1), 1–30. https://doi.org/10.1007/s10854-013-1550-2.

(29) Luna, A.; Obregon, O.; Sosa-Sanchez, J. L.; Dominguez, M. A. Depletion-Type Organic Thin-Film Transistors Based on Solution-Processed Iron Phthalocyanines Fabricated on Plastic Substrates. *Bulletin of Materials Science* **2022**, *45* (1), 20. https://doi.org/10.1007/s12034-021-02607-y.

(30) Brijesh Kumar, B. K. K.; Negi, Y. S. Organic Thin Film Transistors: Structures, Models, Materials, Fabrication, and Applications: A Review. *Polymer Reviews* **2014**, *54* (1), 33–111. https://doi.org/10.1080/15583724.2013.848455.

(31) Ren, Y.; Yang, X.; Zhou, L.; Mao, J.-Y.; Han, S.-T.; Zhou, Y. Recent Advances in Ambipolar Transistors for Functional Applications. *Advanced Functional Materials* **2019**, *29* (40), 1902105. https://doi.org/10.1002/adfm.201902105.

(32) Zhang, C.; Zhu, X. N-Type Quinoidal Oligothiophene-Based Semiconductors for Thin-Film Transistors and Thermoelectrics. *Advanced Functional Materials* **2020**, *30* (31), 2000765. https://doi.org/10.1002/adfm.202000765.

(33) Griggs, S.; Marks, A.; Bristow, H.; McCulloch, I. N-Type Organic Semiconducting Polymers: Stability Limitations, Design Considerations and Applications. *J. Mater. Chem. C* **2021**, *9* (26), 8099–8128. https://doi.org/10.1039/D1TC02048J.

(34) Sui, Y.; Deng, Y.; Du, T.; Shi, Y.; Geng, Y. Design Strategies of N-Type Conjugated Polymers for Organic Thin-Film Transistors. *Mater. Chem. Front.* **2019**, *3* (10), 1932–1951. https://doi.org/10.1039/C9QM00382G.

(35) Gao, X.; Hu, Y. Development of N-Type Organic Semiconductors for Thin Film Transistors: A Viewpoint of Molecular Design. *J. Mater. Chem. C* **2014**, *2* (17), 3099–3117. https://doi.org/10.1039/C3TC32046D.

(36) Boileau, N. T.; Melville, O. A.; Mirka, B.; Cranston, R.; Lessard, B. H. P and N Type Copper Phthalocyanines as Effective Semiconductors in Organic Thin-Film Transistor Based DNA Biosensors at Elevated Temperatures. *RSC Advances* **2019**, *9* (4), 2133–2142. https://doi.org/10.1039/c8ra08829b.

(37) Fayez, M.; Morsi, K. M.; Sabry, M. N. OTFTs Compact Models: Analysis, Comparison, and Insights. *IET Circuits, Devices & Systems* **2017**, *11* (5), 409–420. https://doi.org/10.1049/iet-cds.2016.0439.

(38) Jia, H.; Pant, G. K.; Gross, E. K.; Wallace, R. M.; Gnade, B. E. Gate Induced Leakage and Drain Current Offset in Organic Thin Film Transistors. *Organic Electronics* **2006**, *7* (1), 16–21. https://doi.org/10.1016/j.orgel.2005.10.003.

(39) Waldrip, M.; Jurchescu, O. D.; Gundlach, D. J.; Bittle, E. G. Contact Resistance in Organic Field-Effect Transistors: Conquering the Barrier. *Advanced Functional Materials* **2020**, *30* (20), 1904576. https://doi.org/10.1002/adfm.201904576.

(40) Sun, Y.; Zhang, L.; Ahmed, Z.; Chan, M. Characterization of Interface Trap Dynamics Responsible for Hysteresis in Organic Thin-Film Transistors. *Organic Electronics* **2015**, *27*, 192–196. https://doi.org/10.1016/j.orgel.2015.09.011.

(41) King, B.; Radford, C. L.; Vebber, M. C.; Ronnasi, B.; Lessard, B. H. Not Just Surface Energy: The Role of Bis(Pentafluorophenoxy) Silicon Phthalocyanine Axial Functionalization and Molecular Orientation on Organic Thin-Film Transistor Performance. *ACS Appl. Mater. Interfaces* **2023**, *15* (11), 14937–14947. https://doi.org/10.1021/acsami.2c22789.

(42) Walter, S. R.; Youn, J.; Emery, J. D.; Kewalramani, S.; Hennek, J. W.; Bedzyk, M. J.; Facchetti, A.; Marks, T. J.; Geiger, F. M. In-Situ Probe of Gate Dielectric-Semiconductor Interfacial Order in Organic Transistors: Origin and Control of Large Performance Sensitivities. *J. Am. Chem. Soc.* **2012**, *134* (28), 11726–11733. https://doi.org/10.1021/ja3036493.

(43) Agarwal, I.; Agrawal, A.; Gupta, N. Organic Thin Film Transistors: Device Architecture, Material Selection and Modelling. In *2021 IEEE Madras Section Conference (MASCON)*; 2021; pp 1–5. https://doi.org/10.1109/MASCON51689.2021.9563536.

(44) Mittal, P.; Yadav, S.; Negi, S. Advancements for Organic Thin Film Transistors: Structures, Materials, Performance Parameters, Influencing Factors, Models, Fabrication, Reliability and Applications. *Materials Science in Semiconductor Processing* **2021**, *133*, 105975. https://doi.org/10.1016/j.mssp.2021.105975.

(45) Marinov, O.; Deen, M. J.; Zschieschang, U.; Klauk, H. Organic Thin-Film Transistors: Part I—Compact DC Modeling. *IEEE Transactions on Electron Devices* **2009**, *56* (12), 2952–2961. https://doi.org/10.1109/TED.2009.2033308.

(46) Possanner, S. K.; Zojer, K.; Pacher, P.; Zojer, E.; Schürrer, F. Threshold Voltage Shifts in Organic Thin-Film Transistors Due to Self-Assembled Monolayers at the Dielectric Surface. *Advanced Functional Materials* **2009**, *19* (6), 958–967. https://doi.org/10.1002/adfm.200801466.

(47) Pak, K.; Seong, H.; Choi, J.; Hwang, W. S.; Im, S. G. Synthesis of Ultrathin, Homogeneous Copolymer Dielectrics to Control the Threshold Voltage of Organic Thin-Film Transistors. *Advanced functional materials* **2016**, *26* (36), 6574–6582. https://doi.org/10.1002/adfm.201602585.

(48) Facchetti, A.; Yoon, M.-H.; Marks, T. J. Gate Dielectrics for Organic Field-Effect Transistors: New Opportunities for Organic Electronics. *Advanced Materials* **2005**, *17* (14), 1705–1725. https://doi.org/10.1002/adma.200500517.

(49) Agarwal, A. K.; Agarwal, R.; Mazhari, B. Channel Pinchoff Near Drain in Top Contact Organic Thin-Film Transistor. *IEEE Electron Device Letters* **2015**, *36* (9), 947–949. https://doi.org/10.1109/LED.2015.2459379.

(50) Sevim, A. M.; Ilgün, C.; Gül, A. Preparation of Heterogeneous Phthalocyanine Catalysts by Cotton Fabric Dyeing. *Dyes and Pigments* **2011**, *89* (2), 162–168. https://doi.org/10.1016/j.dyepig.2010.10.008.

(51) Dahlen, M. A. The Phthalocyanines A New Class of Synthetic Pigments and Dyes. *Ind. Eng. Chem.* **1939**, *31* (7), 839–847. https://doi.org/10.1021/ie50355a012.

(52) Cranston, R. R.; Lessard, B. H. Metal Phthalocyanines: Thin-Film Formation, Microstructure, and Physical Properties. *RSC Advances* **2021**, *11* (35), 21716–21737. https://doi.org/10.1039/d1ra03853b.

(53) Melville, O. A.; Lessard, B. H.; Bender, T. P. Phthalocyanine-Based Organic Thin-Film Transistors: A Review of Recent Advances. *ACS Applied Materials and Interfaces* **2015**, *7* (24), 13105–13118. https://doi.org/10.1021/acsami.5b01718.

(54) Vebber, M. C.; Rice, N. A.; Brusso, J. L.; Lessard, B. H. Thermodynamic Property-Performance Relationships in Silicon Phthalocyanine-Based Organic Photovoltaics. *ACS Applied Energy Materials* **2022**, *5* (3), 3426–3435. https://doi.org/10.1021/acsaem.1c04013.

(55) Pearson, A. J.; Plint, T.; Jones, S. T. E.; Lessard, B. H.; Credgington, D.; Bender, T. P.; Greenham, N. C. Silicon Phthalocyanines as Dopant Red Emitters for Efficient Solution Processed OLEDs. *Journal of Materials Chemistry C* **2017**, *5* (48), 12688–12698. https://doi.org/10.1039/c7tc03946h.

(56) Song, C.; Li, Y.; Gao, C.; Zhang, H.; Chuai, Y.; Song, D. An OTFT Based on Titanium Phthalocyanine Dichloride: A New p-Type Organic Semiconductor. *Materials Letters* **2020**, *270*, 127666. https://doi.org/10.1016/j.matlet.2020.127666.

(57) Li, L.; Tang, Q.; Li, H.; Hu, W. Molecular Orientation and Interface Compatibility for High Performance Organic Thin Film Transistor Based on Vanadyl Phthalocyanine. *J. Phys. Chem. B* **2008**, *112* (34), 10405–10410. https://doi.org/10.1021/jp800879g.

(58) Lin, X.; Wang, D.; Xu, L. Preparation and Operating Characteristics Analysis for High-Speed PbPc Organic Thin Film Transistors with Cut-off Frequency of 77 kHz. *Journal of Materials Science: Materials in Electronics* **2021**, *32* (7), 9223–9230. https://doi.org/10.1007/s10854-021-05587-1.

(59) Rella, R.; Capone, S.; Siciliano, P.; Spadavecchia, J.; Ciccarella, G. Spin-Coated Thin Films of Different Metal Phthalocyanines and Porphyrin-Phthalocyanine Blend for Optochemical Sensors of Volatile Organic Compounds. In *Second European Workshop on Optical Fibre Sensors*; Lopez-Higuera, J. M., Culshaw, B., Eds.; SPIE, 2004; Vol. 5502, pp 435–438. https://doi.org/10.1117/12.566796.

(60) Cranston, R. R.; King, B.; Dindault, C.; Grant, T. M.; Rice, N. A.; Tonnelé, C.; Muccioli, L.; Castet, F.; Swaraj, S.; Lessard, B. H. Highlighting the Processing Versatility of a Silicon Phthalocyanine Derivative for Organic Thin-Film Transistors. *Journal of Materials Chemistry C* **2022**, *10* (2), 485–495. https://doi.org/10.1039/d1tc05238a.

(61) Lessard, B. H. The Rise of Silicon Phthalocyanine: From Organic Photovoltaics to Organic Thin Film Transistors. *ACS Applied Materials and Interfaces* **2021**, *13* (27), 31321–31330. https://doi.org/10.1021/acsami.1c06060.

(62) Vebber, M. C.; Grant, T. M.; Brusso, J. L.; Lessard, B. H. Bis(Trialkylsilyl Oxide) Silicon Phthalocyanines: Understanding the Role of Solubility in Device Performance as Ternary Additives in Organic Photovoltaics. *Langmuir* **2020**, *36* (10), 2612–2621. https://doi.org/10.1021/acs.langmuir.9b03772.

(63) Melville, O. A.; Grant, T. M.; Lessard, B. H. Silicon Phthalocyanines as N-Type Semiconductors in Organic Thin Film Transistors. *Journal of Materials Chemistry C* **2018**, *6* (20), 5482–5488. https://doi.org/10.1039/c8tc01116h.

(64) Melville, O. A.; Grant, T. M.; Mirka, B.; Boileau, N. T.; Park, J.; Lessard, B. H. Ambipolarity and Air Stability of Silicon Phthalocyanine Organic Thin-Film Transistors. *Advanced Electronic Materials* **2019**, *5* (8). https://doi.org/10.1002/aelm.201900087.

(65) DiBenedetto, S. A.; Facchetti, A.; Ratner, M. A.; Marks, T. J. Molecular Self-Assembled Monolayers and Multilayers for Organic and Unconventional Inorganic Thin-Film Transistor Applications. *Advanced Materials* **2009**, *21* (14–15), 1407–1433. https://doi.org/10.1002/adma.200803267.

(66) Sun, X.; Di, C.; Liu, Y. Engineering of the Dielectric–Semiconductor Interface in Organic Field-Effect Transistors. *J. Mater. Chem.* **2010**, *20* (13), 2599–2611. https://doi.org/10.1039/B921449F.

(67) Park, Y. D.; Lim, J. A.; Lee, H. S.; Cho, K. Interface Engineering in Organic Transistors. *Materials Today* **2007**, *10* (3), 46–54. https://doi.org/10.1016/S1369-7021(07)70019-6.
(68) Chen, H.; Zhang, W.; Li, M.; He, G.; Guo, X. Interface Engineering in Organic Field-Effect Transistors: Principles, Applications, and Perspectives. *Chem. Rev.* **2020**, *120* (5), 2879–2949. https://doi.org/10.1021/acs.chemrev.9b00532.
(69) Paterson, A. F.; Mottram, A. D.; Faber, H.; Niazi, M. R.; Fei, Z.; Heeney, M.; Anthopoulos, T. D. Impact of the Gate Dielectric on Contact Resistance in High-Mobility Organic Transistors. *Advanced Electronic Materials* **2019**, *5* (5), 1800723. https://doi.org/10.1002/aelm.201800723.
(70) Cranston, R. R.; Vebber, M. C.; Berbigier, J. F.; Rice, N. A.; Tonnelé, C.; Comeau, Z. J.; Boileau, N. T.; Brusso, J. L.; Shuhendler, A. J.; Castet, F.; Muccioli, L.; Kelly, T. L.; Lessard, B. H. Thin-Film Engineering of Solution-Processable n-Type Silicon Phthalocyanines for Organic Thin-Film Transistors. *ACS Applied Materials and Interfaces* **2021**, *13* (1), 1008–1020. https://doi.org/10.1021/acsami.0c17657.
(71) Tang, W.; Li, J.; Zhao, J.; Zhang, W.; Yan, F.; Guo, X. High-Performance Solution-Processed Low-Voltage Polymer Thin-Film Transistors With Low- k /High- k Bilayer Gate Dielectric. *IEEE Electron Device Letters* **2015**, *36* (9), 950–952. https://doi.org/10.1109/LED.2015.2462833.
(72) Mills, T.; Kaake, L. G.; Zhu, X.-Y. Polaron and Ion Diffusion in a Poly(3-Hexylthiophene) Thin-Film Transistor Gated with Polymer Electrolyte Dielectric. *Applied physics. A, Materials science & processing* **2009**, *95* (1), 291–296.
(73) Boudinet, D.; Benwadih, M.; Qi, Y.; Altazin, S.; Verilhac, J.-M.; Kroger, M.; Serbutoviez, C.; Gwoziecki, R.; Coppard, R.; Le Blevennec, G.; Kahn, A.; Horowitz, G. Modification of Gold Source and Drain Electrodes by Self-Assembled Monolayer in Staggered n- and p-Channel Organic Thin Film Transistors. *Organic electronics* **2010**, *11* (2), 227–237.
(74) Wang, Y.; Huang, X.; Li, T.; Li, L.; Guo, X.; Jiang, P. Polymer-Based Gate Dielectrics for Organic Field-Effect Transistors. *Chem. Mater.* **2019**, *31* (7), 2212–2240. https://doi.org/10.1021/acs.chemmater.8b03904.
(75) Koutsiaki, C.; Kaimakamis, T.; Zachariadis, A.; Papamichail, A.; Kamaraki, C.; Fachouri, S.; Gravalidis, C.; Laskarakis, A.; Logothetidis, S. Efficient Combination of Roll-to-Roll Compatible Techniques towards the Large Area Deposition of a Polymer Dielectric Film and the Solution-Processing of an Organic Semiconductor for the Field-Effect Transistors Fabrication on Plastic Substrate. *Organic Electronics* **2019**, *73*, 231–239. https://doi.org/10.1016/j.orgel.2019.06.010.
(76) Singh, R.; Lin, Y.-T.; Chuang, W.-L.; Ko, F.-H. A New Biodegradable Gate Dielectric Material Based on Keratin Protein for Organic Thin Film Transistors. *Organic Electronics* **2017**, *44*, 198–209. https://doi.org/10.1016/j.orgel.2017.02.024.
(77) Raghuwanshi, V.; Saxena, P.; Rahi, S.; Mahato, A. K.; Varun, I.; Tiwari, S. P. Solution-Processed Flexible Organic Field-Effect Transistors with Biodegradable Gelatin as the Dielectric Layer: An Approach Toward Biodegradable Systems. *ACS Appl. Electron. Mater.* **2020**, *2* (10), 3373–3379. https://doi.org/10.1021/acsaelm.0c00648.
(78) Kim, C.; Facchetti, A.; Marks, T. J. Probing the Surface Glass Transition Temperature of Polymer Films via Organic Semiconductor Growth Mode,

Microstructure, and Thin-Film Transistor Response. *J. Am. Chem. Soc.* **2009**, *131* (25), 9122–9132. https://doi.org/10.1021/ja902788z.

(79) Roberts, M. E.; Queraltó, N.; Mannsfeld, S. C. B.; Reinecke, B. N.; Knoll, W.; Bao, Z. Cross-Linked Polymer Gate Dielectric Films for Low-Voltage Organic Transistors. *Chem. Mater.* **2009**, *21* (11), 2292–2299. https://doi.org/10.1021/cm900637p.

(80) Merari Masillamani, A.; Orgiu, E.; Samorì, P. Effect of the Molecular Weight of the Polymer Gate Dielectric on the Performances of Solution-Processed Ambipolar OTFTs. *J. Mater. Chem. C* **2013**, *1* (46), 7725–7730. https://doi.org/10.1039/C3TC31080A.

(81) Ji, D.; Xu, X.; Jiang, L.; Amirjalayer, S.; Jiang, L.; Zhen, Y.; Zou, Y.; Yao, Y.; Dong, H.; Yu, J.; Fuchs, H.; Hu, W. Surface Polarity and Self-Structured Nanogrooves Collaboratively Oriented Molecular Packing for High Crystallinity toward Efficient Charge Transport. *J. Am. Chem. Soc.* **2017**, *139* (7), 2734–2740. https://doi.org/10.1021/jacs.6b12153.

(82) Yang, J.; Yan, D.; Jones, T. S. Molecular Template Growth and Its Applications in Organic Electronics and Optoelectronics. *Chem. Rev.* **2015**, *115* (11), 5570–5603. https://doi.org/10.1021/acs.chemrev.5b00142.

(83) Yang, J.; Yan, D. Weak Epitaxy Growth of Organic Semiconductor Thin Films. *Chem. Soc. Rev.* **2009**, *38* (9), 2634–2645. https://doi.org/10.1039/B815723P.

(84) Lizhen Huang; Chengfang Liu; Bo Yu; Jidong Zhang; Yanhong Geng; Donghang Yan. Evolution of 2,5-Bisbithiophene Thin Films and Its Effect on the Weak Epitaxy Growth of ZnPc. *The journal of physical chemistry. B* **2010**, *114* (14), 4821.

(85) Song, D.; Zhu, F.; Yu, B.; Huang, L.; Geng, Y.; Yan, D. Tin (IV) Phthalocyanine Oxide: An Air-Stable Semiconductor with High Electron Mobility. *Applied Physics Letters* **2008**, *92* (14), 143303. https://doi.org/10.1063/1.2903486.

(86) Gu, W.; Hu, Y.; Zhu, Z.; Liu, N.; Zhang, J.; Wang, J. Preparing Highly Ordered Copper Phthalocyanine Thin-Film by Controlling the Thickness of the Modified Layer and Its Application in Organic Transistors. *Solid-State Electronics* **2013**, *89*, 101–104. https://doi.org/10.1016/j.sse.2013.07.008.

(87) Shao, X.; Wang, S.; Li, X.; Su, Z.; Chen, Y.; Xiao, Y. Single Component P-, Ambipolar and n-Type OTFTs Based on Fluorinated Copper Phthalocyanines. *Dyes and Pigments* **2016**, *132*, 378–386. https://doi.org/10.1016/j.dyepig.2016.05.020.

(88) Yan, X.; Wang, J.; Wang, H.; Wang, H.; Yan, D. Improved N-Type Organic Transistors by Introducing Organic Heterojunction Buffer Layer under Source/Drain Electrodes. *Applied Physics Letters* **2006**, *89* (5), 053510. https://doi.org/10.1063/1.2227714.

(89) Wang, H.; Zhu, F.; Yang, J.; Geng, Y.; Yan, D. Weak Epitaxy Growth Affording High-Mobility Thin Films of Disk-Like Organic Semiconductors. *Advanced materials (Weinheim)* **2007**, *19* (16), 2168–2171. https://doi.org/10.1002/adma.200602566.

(90) Wang, H.; Song, D.; Yang, J.; Yu, B.; Geng, Y.; Yan, D. High Mobility Vanadyl-Phthalocyanine Polycrystalline Films for Organic Field-Effect Transistors. *Applied Physics Letters* **2007**, *90* (25), 253510. https://doi.org/10.1063/1.2751103.

(91) Virkar, A. A.; Mannsfeld, S.; Bao, Z.; Stingelin, N. Organic Semiconductor Growth and Morphology Considerations for Organic Thin-Film Transistors. *Advanced Materials* **2010**, *22* (34), 3857–3875. https://doi.org/10.1002/adma.200903193.

(92) Yang, J.; Wang, T.; Wang, H.; Zhu, F.; Li, G.; Yan, D. Ultrathin-Film Growth of Para-Sexiphenyl (I): Submonolayer Thin-Film Growth as a Function of the Substrate Temperature. *J. Phys. Chem. B* **2008**, *112* (26), 7816–7820. https://doi.org/10.1021/jp711455u.

(93) Yang, J.; Wang, T.; Wang, H.; Zhu, F.; Li, G.; Yan, D. Ultrathin-Film Growth of Para-Sexiphenyl (II): Formation of Large-Size Domain and Continuous Thin Film. *The journal of physical chemistry. B* **2008**, *112* (26), 7821–7825. https://doi.org/10.1021/jp711457p.

(94) Aliofkhazraei, M.; Ali, N. 7.09 - AFM Applications in Micro/Nanostructured Coatings. In *Comprehensive Materials Processing*; Hashmi, S., Batalha, G. F., Tyne, C. J. V., Yilbas, B., Eds.; Elsevier: Oxford, 2014; pp 191–241. https://doi.org/10.1016/B978-0-08-096532-1.00712-3.

(95) Wen, Y.; Liu, Y.; Guo, Y.; Yu, G.; Hu, W. Experimental Techniques for the Fabrication and Characterization of Organic Thin Films for Field-Effect Transistors. *Chem. Rev.* **2011**, *111* (5), 3358–3406. https://doi.org/10.1021/cr1001904.

(96) Andrei A. Bunaciu, E. gabriela U.; Aboul-Enein, H. Y. X-Ray Diffraction: Instrumentation and Applications. *Critical Reviews in Analytical Chemistry* **2015**, *45* (4), 289–299. https://doi.org/10.1080/10408347.2014.949616.

(97) Steele, J. A.; Solano, E.; Hardy, D.; Dayton, D.; Ladd, D.; White, K.; Chen, P.; Hou, J.; Huang, H.; Saha, R. A.; Wang, L.; Gao, F.; Hofkens, J.; Roeffaers, M. B. J.; Chernyshov, D.; Toney, M. F. How to GIWAXS: Grazing Incidence Wide Angle X-Ray Scattering Applied to Metal Halide Perovskite Thin Films. *Advanced Energy Materials* **2023**, *13* (27), 2300760. https://doi.org/10.1002/aenm.202300760.

(98) Mahmood, A.; Wang, J.-L. A Review of Grazing Incidence Small- and Wide-Angle X-Ray Scattering Techniques for Exploring the Film Morphology of Organic Solar Cells. *Solar RRL* **2020**, *4* (10), 2000337. https://doi.org/10.1002/solr.202000337.

(99) Xu, B.; Mao, N.; Zhao, Y.; Tong, L.; Zhang, J. Polarized Raman Spectroscopy for Determining Crystallographic Orientation of Low-Dimensional Materials. *J. Phys. Chem. Lett.* **2021**, *12* (31), 7442–7452. https://doi.org/10.1021/acs.jpclett.1c01889.

(100) Wood, S.; Hollis, J. R.; Kim, J.-S. Raman Spectroscopy as an Advanced Structural Nanoprobe for Conjugated Molecular Semiconductors. *Journal of physics. D, Applied physics* **2017**, *50* (7), 73001-.

(101) Szybowicz, M.; Bała, W.; Fabisiak, K.; Paprocki, K.; Drozdowski, M. The Molecular Structure Ordering and Orientation of the Metallophthalocyanine CoPc, ZnPc, CuPc, and MgPc Thin Layers Deposited on Silicon Substrate, as Studied by Micro-Raman Spectroscopy. *Journal of Materials Science* **2011**, *46* (20), 6589–6595. https://doi.org/10.1007/s10853-011-5607-4.

(102) Cranston, R. R.; Lanosky, T. D.; Ewenike, R.; Mckillop, S.; King, B.; Lessard, B. H. Polarized Raman Microscopy to Image Microstructure Changes in Silicon Phthalocyanine Thin-Films. *Small Science n/a* (n/a), 2300350. https://doi.org/10.1002/smsc.202300350.

Chapter 2. Toward Weak Epitaxial Growth of Silicon Phthalocyanines: How the Choice of the Optimal Templating Layer Differs from Traditional Phthalocyanines

This chapter was published in the journal “ACS Applied Electronic Materials”: Ewenike, R. B.; King, B.; Battaglia, A. M.; Quezada Borja, J. D.; Lin, Z. S.; Manion, J. G.; Brusso, J. L.; Kelly, T. L.; Seferos, D. S.; Lessard, B. H. Toward Weak Epitaxial Growth of Silicon Phthalocyanines: How the Choice of the Optimal Templating Layer Differs from Traditional Phthalocyanines. A*CS Appl. Electron. Mater.* 2023, 5, 12, 7023–7033.

Context

Our group has experience developing OTFTs based on F10-SiPc which is fluorinated semiconductor. Templating layers such as *p*-6P were found to work well with phthalocyanines but we hypothesized that using a fluorinated template for WEG would lead to favourable F-F interactions with the semiconductor leading to better OTFTs. Our collaborators synthesized para-sexiphenly (*p*-6PF), as a template layer molecule that was fully fluorinated. This template layer was selected because previously in our group we have reported improved OTFT μ through fluorine-fluorine interactions between the SAM and solution processed SiPc. To begin, the optimization of *p*-6PF deposition we decided to use similar deposition rate, thicknesses and substrate temperature that has been reported for the deposition of *p*-6P. We then fabricated F_{10}-SiPc OTFTs with a range of template thicknesses and substrate temperature during deposition.

Contributions

In this work, I synthesised F_{10}-SiPc, fabricated all OTFTs and characterized all devices. I performed the contact angle and PXRD measurements. Benjamin King (now Dr.) trained and mentored me in OTFT fabrication and characterization. Dr. Sonia Lin synthesised *p*-6PF and final purification through train sublimation was performed by Dr. Benjamin King and me. Alicia Battaglia and Dr. Joseph Manion performed AFM measurements and I interpreted the images. David Borja performed and interpreted all GIWAXS data. I wrote the manuscript and with major inputs and suggestion from Dr. Joseph Manion and Dr.

Benoit Lessard. The manuscript was reviewed by all co-authors before peer-review submission.

Abstract

Weak epitaxial growth typically utilizes oligomeric or polymeric phenyls or thiophenes as a templating layer to improve the deposition of metal phthalocyanines (MPc) and other disk-like molecules. In this study, we report the use of per-fluorinated para-sexiphenyl(*p*-6PF) as a templating layer, for the fabrication of bis (pentafluorophenoxy) silicon phthalocyanine (F_{10}-SiPc)-, copper phthalocyanine (CuPc)-, and per fluorinated copper phthalocyanine (F_{16}-CuPc) – based organic thin-film transistors (OTFTs). By optimizing the deposition time and substrate temperature during deposition, we were able to control the surface coverage, roughness, and growth morphology of *p*-6PF leading to F_{10}-SiPc OTFTs with *n*-type mobilities (μ) of 0.14 $cm^2V^{-1}s^{-1}$. In comparison, using CuPc and F16-CuPc with *p*-6PF led to mobilities of 0.009 (holes) and 0.012 $cm^2V^{-1}s^{-1}$ (electrons), respectively. In contrast, an unfluorinated para-sexiphenyl (*p*-6P) templating layer demonstrates inferior performance as a template for F_{10}-SiPc while proving to be more effective for CuPc and F_{16}-CuPc. Atomic force microscopy and powder X-ray diffraction suggest that higher surface coverage of the *p*-6PF layer increased the grain sizes and crystallinity of F_{10}-SiPc. Grazing-incidence wide-angle X-ray scattering shows improved crystallinity of F_{10}-SiPc on *p*-6PF over *p*-6P and vice versa for F_{16}-CuPc. Overall, these results demonstrate that *p*-6PF is a promising templating candidate for F_{10}-SiPc-based OTFTs and that the choice of the templating layer needs to be optimized for the semiconductor.

2.1 Introduction

Organic thin film transistors (OTFTs) have emerged as a promising alternative to conventional metal-oxide-semiconductor field-effect transistors (MOSFETs) for developing next generation electronics due to their relatively low-cost and low-energy manufacturing requirements.[1–5] OTFTs are ideal candidates for applications including electronic paper, gas sensors, wearable/stretchable technology, and smart packaging. [6–11] Though already promising further improvements to efficiency, stability and cost are needed to realize the full potential of this technology. High performance OTFTs require optimization of their individual layer (semiconductor and dielectric morphology),

dielectric/semiconductor, and metal/semiconductor interfaces which all play crucial roles in charge generation and transport.[12–18]

Metal phthalocyanines (MPc) are a class of organic molecules that typically contain a central transition metal atom in a four membered isoindole macro-cycle.[19] Their chemical and thermal stability, combined with their ability to absorb both infrared and visible light, has made them a preferred material for use in dyes, pigments, and photovoltaic applications.[20–22] Most common MPcs are divalent disk-like molecules which yield air-stable p-type OTFTs.[23] Silicon phthalocyanines are a unique class of phthalocyanines that have shown excellent n-type performance in OTFT.[24,25] The presence of the tetravalent silicon atom enables axial substitution of the central atom, which provides an additional handle for molecule tunability and solid state engineering.[15,26] Beyond the functionality and properties of these molecules the deposition conditions, and resulting thin film characteristics are critical to the final device performance and must be carefully selected.[27]

Molecular template growth (MTG) has emerged as a viable method for improving the quality of semiconductor films in OTFTs, offering controllable surface and interlayer properties that enhance film morphology, molecular electronic behaviour , and tune molecular orientations of the semiconductor.[28,29] Weak epitaxial growth (WEG), a subclass of MTG, typically uses a para-sexiphenyl (*p*-6P) or para-sexithiophene (α-6T) dielectric template layers for the deposition of organic semiconductors.[28,30,31] At an atomic scale these rod-like molecules possess a significantly smoother surface relative to amorphous silicon dioxide (SiO_2) substrates.[32] The crystal formation of template layers is influenced by both chemical structure and deposition conditions, particularly through variations in deposition rate and substrate temperature during deposition.[33–36] Previous studies have demonstrated that increasing the deposition temperature of *p*-6P induces a change in its growth morphology, subsequently affecting the quality and size of the template domains.[37] The chemical structure of the template layer can also influence film formation. In a previous study partial terminal fluorination of *p*-6P to form a derivative called 6P-F_4 ($C_{36}H_{22}F_4$), significantly enhanced layer-to-layer growth and thin film formation.[38] To increase the effectiveness of template layers for the WEG of MPcs it is

crucial to optimize both the template chemical structure and the deposition conditions of template layers.

In organic electronics the ability to control molecule structural properties such as the molecular orientation at layer interfaces is crucial for device performance and application.[39,40] In OTFTs an edge-on molecular orientation of the semiconductors parallel to the substrate improves π-π stacking alignment, and ultimately charge transport. The use of *p*-6P for the WEG growth of some disk-like MPcs such as Tin (IV) phthalocyanine oxide (SnOPc), vanadyl-phthalocyanine (VOPc), zinc phthalocyanine (ZnPc), CuPc and F_{16}-CuPc has been shown to improve edge-on molecular orientation of these semiconductors and subsequently device mobility.[30,41–44] The use of *p*-6P as a template for the deposition of CuPc and F_{16}-CuPc has significantly improved charge mobilities compared to CuPc and F_{16}-CuPc deposited on a self-assembled monolayer (SAM) of octyl trichlorosilane (OTS) or bare silicon dioxide (SiO_2).[45,46] However, when employing *p*-6P as a template layer for F_{10}-SiPc-based OTFTs, it has been observed that edge-on π-π stacking is less pronounced compared to F_{10}-SiPc deposited on OTS.[47] It has been shown that use of a low surface energy dielectric modifier, such as OTS, typically yields greater charge mobility in OTFTs.[48–51] The hydrophobic surface promotes the diffusion of the organic semiconducting layer during film growth, resulting in the formation of larger grains which ultimately improves device performance.[52] It has also been reported that matching the total surface energy (γ_s^{tot}) of the modified dielectric layer while maximizing the dispersive surface energy (γ_s^{d}) and minimizing the polar surface energy (γ_s^{p}) can also increase device performance in molecular single-crystal OTFTs.[47,53]

In this study, we show the impact of deposition conditions on a template layer (*p*-6PF) on the resulting electrical performance of F_{10}-SiPc OTFTs. To optimize surface coverage of *p*-6PF varying target thicknesses and substrate temperature during deposition were explored and the resulting template films were used for fabrication and characterization of three metal phthalocyanines bottom-gate top-contact (BGTC) OTFTs, (**Figure 2.1**). The *p*-6PF deposition conditions that yielded the highest measured mobilities for F_{10}-SiPc OTFTs were then used to prepare CuPc and F_{16}-CuPc OTFTs. Atomic force microscopy (AFM) and powder X-ray diffraction (PXRD) were performed on F_{10}-SiPc/*p*-6PF bilayers with different combinations of *p*-6PF thicknesses and deposition

temperatures. The AFM and PXRD analysis allowed for differentiation of distinct growth morphologies and surface coverages of *p*-6PF at different temperatures while providing insights into the film morphology, crystallinity, grain sizes, and boundaries of F_{10}-SiPc films on *p*-6PF. Contact angle measurements were done on dielectric modifiers (OTS, *p*-6P, and *p*-6PF) and the MPcs (F_{10}-SiPc, CuPc, and F_{16}-CuPc) used in this study to show the impact of surface energy on device performance. The use of grazing incidence wide-angle X-ray scattering (GIWAXS) measurements were performed on F_{16}-CuPc and F_{10}-SiPc films with *p*-6P and *p*-6PF as template layers to investigate film structure and correlate to device mobility. GIWAXs provides insight to why *p*-6P significantly enhances the OTFT mobility of F_{16}-CuPc, but not F_{10}-SiPc, while *p*-6PF improves OTFT mobility of F_{10}-SiPc but not F_{16}-CuPc. Overall, these results show that the *p*-6P templating layer is favourable for planar MPcs but that F_{10}-SiPc OTFTs are improved with a fluorinated templating layer.

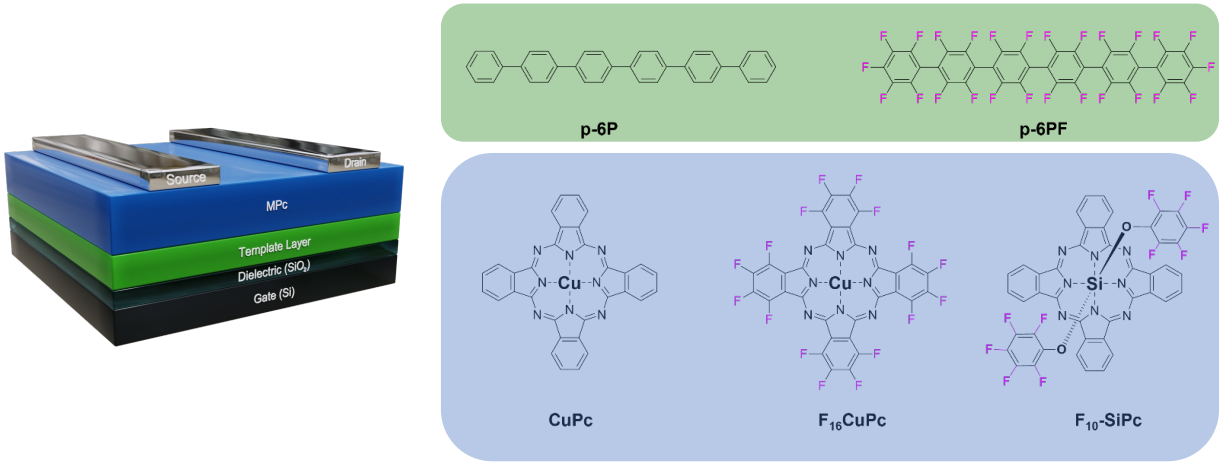

Figure 2.1. *Schematic diagram and chemical structures for the BGTC OTFT device, including the template layer (p-6PF or p-6P) and the organic semiconductor layers (CuPc, F_{16}-CuPc, or F_{10}-SiPc).*

2.2 Results and Discussion

The templating effect of *p*-6PF for WEG of F_{10}-SiPc is studied using a heterojunction bilayer (F_{10}-SiPc/ *p*-6PF) into OTFTs. (as outlined in the Experimental Section). Silver electrodes with a manganese interlayer were chosen for F_{10}-SiPc devices, to reduce the contact resistance.[54] **Table 2.1** summarizes the electrical performance of the devices, including the average field-effect mobility (μ), threshold voltage (V_t), on-off current ratio, substrate temperature during deposition, and target thickness of *p*-6PF. We

deposited *p*-6PF on SiO_2 coated silicon wafers at varying substrate temperatures (25, 100, 150, or 180°C) and to three target thicknesses (2, 4, or 8 nm) as determined by a quartz crystal microbalance (QCM) followed by deposition of F_{10}-SiPc films at ambient temperature. All devices were compared to a control with no *p*-6PF layer. The maximum average mobility measured with a *p*-6PF template layer was 0.14 $cm^2\ V^{-1}\ s^{-1}$ for the devices with 8 nm of *p*-6PF deposited at a substrate temperature of a 100°C. This measured mobility is in the same order of magnitude as previously reported when using OTS, which is known to be a SAM to achieve high performance F_{10}-SiPc based OTFTs.[47,55]

Table 2.1. *Electrical characteristics of metal phthalocyanine OTFTs with a p-6PF layer deposited at different thicknesses and temperatures.*

metal phthalocyanine	*p*-6PF substrate temperature during deposition (°C)	template thickness (nm)	μ [$10^{-2}\ cm^2\ V^{-1}\ s^{-1}$] [a]	V_t [V] [a]	$I_{on/off}$ [b]	n[c]
F_{10}-SiPc	–[d]	0	1.69 ± 0.8	13.2 ± 1.9	10^4	39
F_{10}-SiPc	25	2	1.40 ± 0.6	18.6 ± 1.4	10^4	37
F_{10}-SiPc	25	4	2.20 ± 9.6	13.3 ± 2.0	10^4	32
F_{10}-SiPc	25	8	12.4 ± 1.7	14.6 ± 1.3	10^3	36
F_{10}-SiPc	100	2	0.34 ± 0.1	11.3 ± 5.1	10^5	33
F_{10}-SiPc	100	4	2.15 ± 1.1	10.9 ± 2.8	10^5	39
F_{10}-SiPc	100	8	14.10 ± 3.1	10.4 ± 2.4	10^3	38
F_{10}-SiPc	150	2	2.30 ± 0.7	12.3 ± 2.4	10^5	37
F_{10}-SiPc	150	4	6.50 ± 1.7	14.0 ± 2.1	10^5	33
F_{10}-SiPc	150	8	0.88 ± 0.6	14.4 ± 5.8	10^5	70
F_{10}-SiPc	180	2	0.44 ± 0.2	18.5 ± 4.1	10^5	36
F_{10}-SiPc	180	4	0.87 ± 0.6	7.10 ± 7.4	10^4	37
CuPc[*]	25	8	0.90 ± 0.2	-7.50 ± 2.5	10^3	35
F_{16}-CuPc	25	8	1.20 ± 0.9	3.10 ± 2.6	10^3	40

μ^a and V_t^a were calculated average values n-type devices except for CuPc* which reports a p-type semiconductor. $I_{on/off}^b$ values were calculated based on the median. n^c represents the number of OTFTs used for average and median calculation. ^{d} represents the F_{10}-SiPc device fabricated on bare SiO_2.

From the mobility measured for OTFTs with different *p*-6PF deposition thicknesses it is clear that the performance of F_{10}-SiPc devices is related to the target thickness of *p*-6PF. However, the results (**Table 2.1**) also demonstrate that substrate temperature has a significant impact on the efficacy of the template layer. To increase the effectiveness of the template layer good surface coverage is required to reduce effect of the amorphous substrate during deposition of the semiconductor by providing a smoother surface and a stronger interaction to organic molecules.[28,56] It is worth noting that these materials do not form a perfect monolayer. In certain instances, a 2nd monolayer may commence its growth before the 1st monolayer reaches completion, and occasionally, the formation of a 3rd monolayer may initiate when the second layer is only halfway formed.[37,57] The significant increase in mobilities of F_{10}-SiPc OTFTs with varying *p*-6PF thicknesses, deposited at 25 and 100°C, show a clear trend of increased mobility with increasing thickness of *p*-6PF, particularly highlighted by the substantial improvements observed at a target thickness of 8 nm (**Figure 2.2 and 2.3D**). In contrast, when *p*-6PF was deposited at 150°C F_{10}-SiPc OTFT mobility increased with template thickness from 2 to 4 nm, followed by a significant decrease in mobility to below the control devices at 8 nm (**Figure 2.4D**). Furthermore, films deposited at 25 and 100°C, showed decreased V_t at thicknesses of 2 nm to 4 nm, with 2 nm resulting in the highest V_t at both temperatures (**Figure 2.2 and 2.3E**). The V_t of devices prepared on *p*-6PF deposited at 150°C. did not show any significant change with changes to the thickness of *p*-6PF (**Figure 2.4E**).

Atomic force microscopy (AFM) was used to analyse the effect of substrate deposition temperature on the growth morphology of *p*-6PF and the resulting film morphologies of the F_{10}-SiPc/*p*-6PF bilayer. Furthermore, AFM and powdered X-ray diffraction (PXRD) were used to characterize the effect of target thickness on the surface coverage of *p*-6PF, the resulting F_{10}-SiPc/*p*-6PF films textures and the crystallinity of F_{10}-SiPc deposited on *p*-6PF. The growth pattern of *p*-6PF was found to be influenced by the substrate

temperature during deposition, similar to observations reported in literature for *para*-sexiphenyl (*p*-6P).[37] The *p*-6PF template layer is clearly visible underneath the F_{10}-SiPc film when a 2 nm layer of *p*-6PF was deposited on the substrate at 25 °C it exhibited a rod-like island morphology (**Figure 2.2A**). By increasing thickness to 4 nm and 8 nm (**Figure 2.2B and C**), the rod-like islands widened, and the domain boundaries decreased. Furthermore, at elevated temperatures of 100 and 150 °C during deposition rounder and more compact island were observed, indicating that increasing the substrate temperature during deposition alters the growth morphology of *p*-6PF. However, there is a slight difference in the growth morphology of *p*-6PF at substrate temperature of 100 and 150 °C during deposition. Specifically, at 100 °C *p*-6PF formed dendritic islands (**Figure 2.9**) which continued to grow and coalesce with neighboring islands, as seen for 2, 4 and 8 nm in **Figure 2.3 A-C** respectively. At a deposition temperature of 150°C *p*-6PF formed island similar to those observed at 100°C but without the dendrites as seen in **Figure 2.4 A-C**. Deposition performed at 180 °C showed no visible features of *p*-6PF underneath the F_{10}-SiPc film (**Figure 2.10**). This observation leads us to conclude that at this temperature *p*-6PF was not able to condense on the substrate and no *p*-6PF film was formed. This behaviour is not surprising, as it is typical for the physical vapour deposition (PVD) processes to cause molecules to re-evaporate from the surface due to the significantly lower heat of vaporization per atom compared to the bulk molecules.[58] The results emphasize that altering the deposition temperature of the template layer can induce favorable changes in the growth morphology, leading to larger grain sizes of the template film. However, it is crucial to carefully select deposition temperatures that are conducive not only to the formation of the template film but also for the WEG of the MPc.

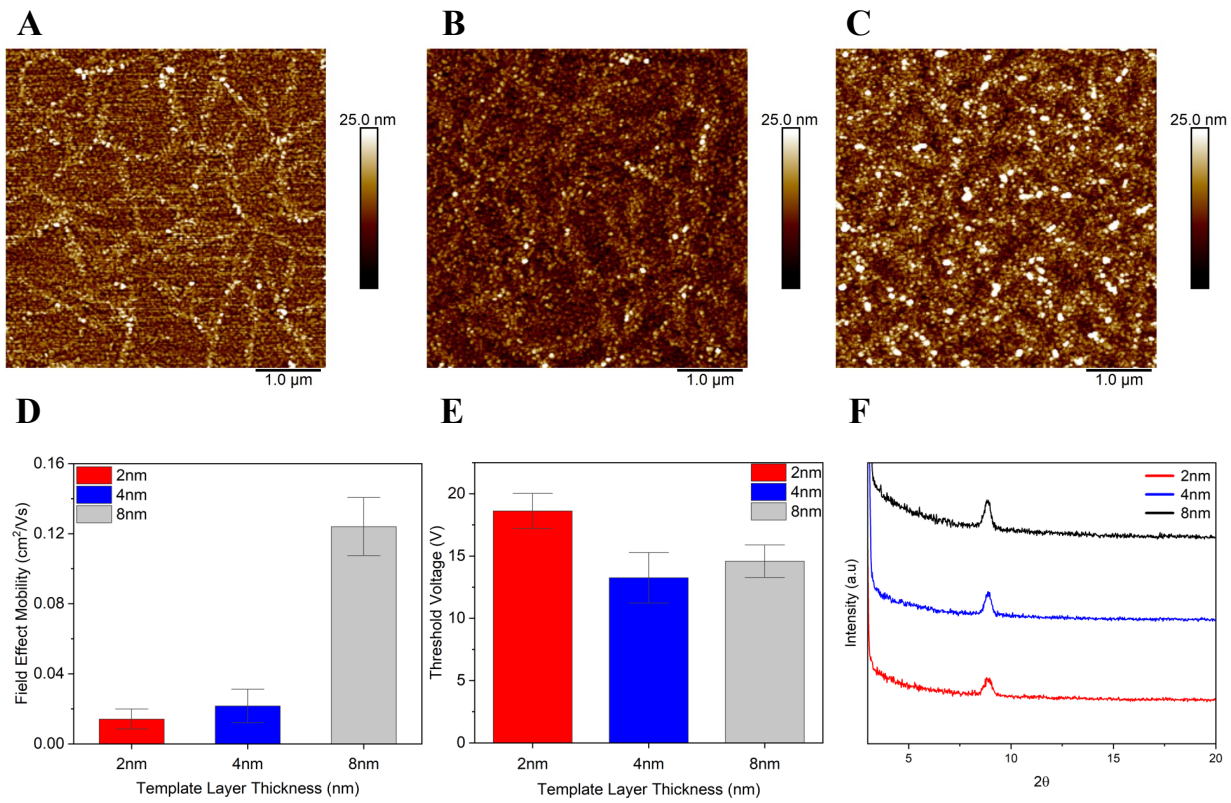

Figure 2.2. *Atomic force microscopy images of (A) 2, (B) 4 and (C) 8 nm of p-6PF deposited at 25 °C. Average saturation region (D) mobility (cm^2/Vs), (E) threshold voltage (V) and (F) PXRD of F_{10}-SiPc OTFTs with different thicknesses of the p-6PF deposited at 25°C.*

The AFM observations at 180°C led to further study on the effect of surface coverage on not only device performance but also the crystallinity of our semiconductor with increasing target thickness of *p*-6PF. The underperformance of OTFTs prepared with a *p*-6PF deposition temperature of 180°C can be attributed to non-existent surface coverage of *p*-6PF, resulting in mobilities worse than those of the control (**Table 2.1**). PXRD measurements illustrate that as the target thickness of *p*-6PF increased at deposition temperatures of 25, 100, and 150°C, the crystallinity of the F_{10}-SiPc film also increased as shown in **Figure 2.2F, 2.3F, and 2.4F** respectively. The increased peak intensities indicate the formation of more ordered and crystalline F_{10}-SiPc films, which correlates with the observed increase in mobility. However, despite the increase in PXRD peak intensity from a target thickness of 4 to 8 nm at a deposition temperature of 150 °C, the device mobility did not show a corresponding improvement. AFM images of the 8 nm *p*-6PF deposited at 150°C (**Figure 2.4C**) reveal very high peaks with height variations

exceeding 100 nm after the deposition of F_{10}-SiPc. This rough surface is unsuitable for forming effective charge carrier paths, thereby negatively impacting device performance. Height profiles and 3D AFM images of 8 nm F_{10}-SiPc deposited at 25, 100, and 150°C (**Figure 2.11**) revealed significantly smoother surfaces for deposition temperatures of 25 and 100°C. This shows although surface coverage is crucial for the templating effect of the semiconductor other factors such as surface roughness also play a prominent role in determining device performance.

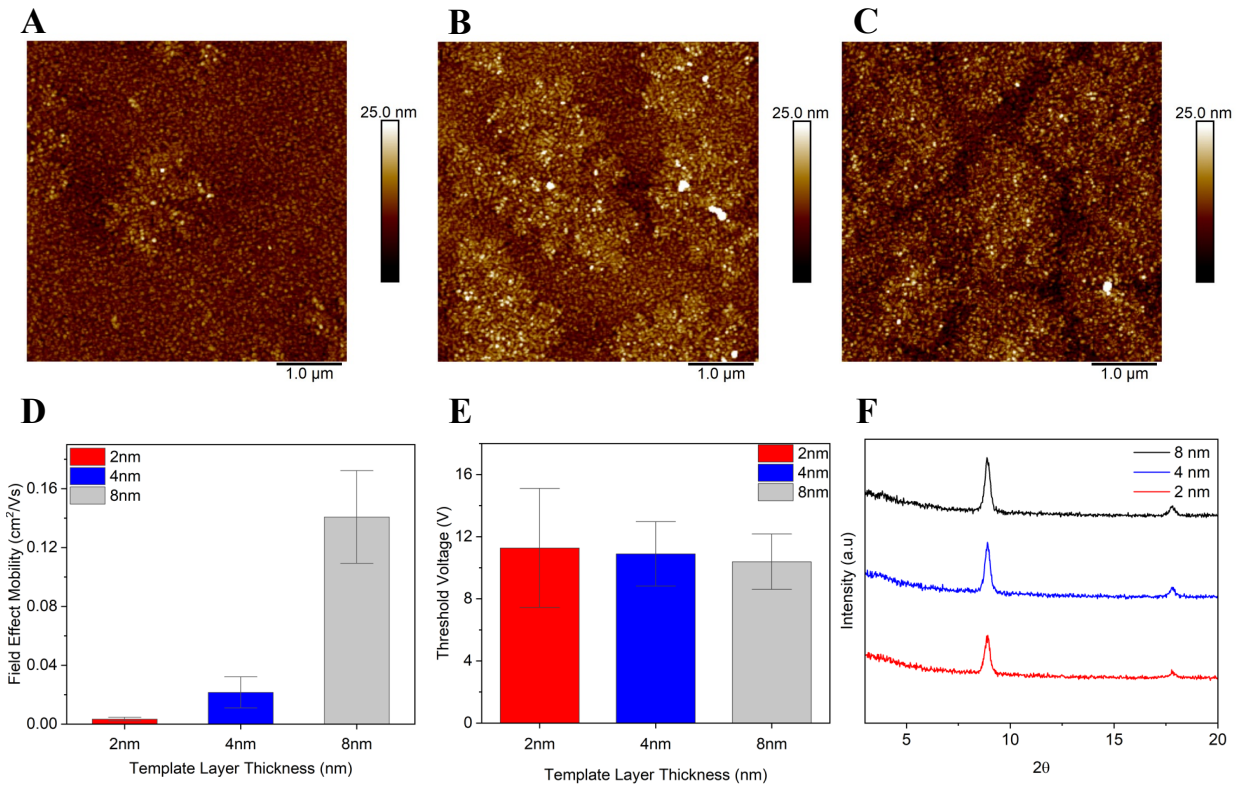

Figure 2.3. *Atomic force microscopy images of (A) 2, (B) 4 and (C) 8 nm of p-6PF deposited at 100 °C. Average saturation region (D) mobility (cm^2/Vs), (E) threshold voltage (V) and (F) PXRD of F_{10}-SiPc OTFTs with different thicknesses of the p-6PF deposited at 100°C.*

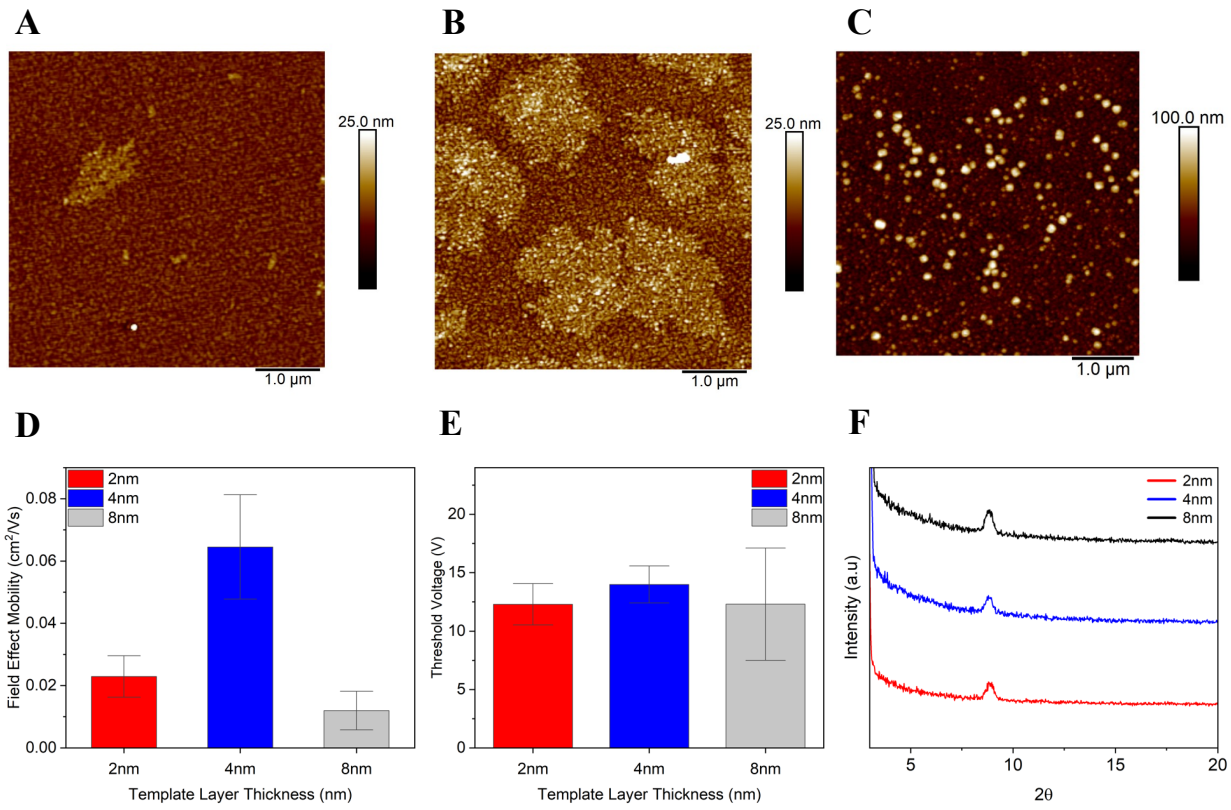

Figure 2.4. *Atomic force microscopy images of (A) 2, (B) 4 and (C) 8 nm of p-6PF deposited at 150 °C. Average saturation region (D) mobility (cm^2/Vs), (E) threshold voltage (V) and (F) PXRD of F_{10}-SiPc OTFTs with different thicknesses of the p-6PF deposited at 150°C.*

Based on these results, we used the optimized *p*-6PF deposition conditions to fabricate CuPc and F_{16}-CuPc based OTFTs, which yielded carrier charge mobilities of 0.009 (hole) and 0.012 (electron) $cm^2\ V^{-1}\ s^{-1}$, respectively (**Table 2.1**). OTFTs made using un-fluorinated *p*-6P as the templating layer have been reported to have significantly greater charge mobilities closer to 0.18 and 0.27 $cm^2\ V^{-1}\ s^{-1}$ for CuPc and F_{16}-CuPc respectively.[43,44,59,60] Using *p*-6PF as the template layer for F_{16}-CuPc resulted in OTFTs with mobilities on the same order of magnitude as those reported in literature for F_{16}-CuPc made with OTS. CuPc-based OTFT devices fabricated using *p*-6PF also yield charge mobility on the same order of magnitude of CuPc fabricated with OTS and bare SiO_2.[45,61] These results suggest that *p*-6PF is an effective templating layer for F_{10}-SiPc, but it is not as suitable for CuPc and F_{16}-CuPc. In comparison, *p*-6P serves as a better template for CuPc and F_{16}-CuPc, but it exhibits lower effectiveness as a template for F_{10}-

SiPc. Additionally results evidently show the significance of adjusting the deposition conditions of the chosen template layer in order optimize device performance.

Table 2.2. *Surface energy of films deposited on an SiO_2 dielectric layer.*

	contact angle (deg °)					
material	deionized water	diiodomethane	γ_s^d (mJ·m^2)	γ_s^p (mJ·m^2)	γ_s^{tot} (mJ·m^2)	n[a]
p-6PF	101.6 ± 0.9	74.8 ± 2.7	19.0 ± 1.7	1.5 ± 0.5	20.6 ± 1.2	4
p-6P[*]	79.3 ± 5.2	44.9 ± 2.1	33.7 ± 2.5	5.1 ± 3.3	38.7 ± 0.8	–
OTS	103.7 ± 1.3	67.0 ± 2.0	24.1 ± 1.4	0.5 ± 0.3	24.6 ± 1.2	4
F_{10}-SiPc	105.1 ± 1.6	39.0 ± 4.0	40.7 ± 2.2	0.03 ± 0.1	40.8 ± 2.2	4
CuPc	68.6 ± 1.7	39.2 ± 4.3	34.8 ± 2.3	9.6 ± 1.4	44.5 ± 1.5	4
F_{16}-CuPc	96.9 ± 1.7	63.5 ± 2.0	25.3 ± 1.4	1.5 ± 0.6	26.7 ± 1.0	4

n[a] represents the number of contact angle measurements used for calculating surface energies. *p*-6P contact angle data and surface energy values gotten from literature.[47]

We, and others have shown a correlation between the surface energy of a modified dielectric layer and the device electrical performance.[47,49,51] This is because the interface between the semiconductor and the dielectric layer plays a crucial role in the generation and transport of charge carries.[62] A low surface energy typically increases the charge mobility in OTFTs.[48–50] However, it is also reported that matching the γ_s^{tot} of the template layer and the semiconductor while maximizing the dispersive surface energy (γ_s^d) and minimizing the polar surface energy (γ_s^p) can also increase OTFT mobility.[47,53] To determine the total surface energy (γ_s^{tot}) of the films presented in **Table 2.2**, we calculated the polar (γ_s^p) and dispersive (γs^d) surface energy component using contact angle measurement of deionized water and diiodomethane (**Figure 2.19**) for the application of the Fowkes model.[63] **Figure 2.5** shows the γ_s^{tot} as a component of the γ_s^p and γ_s^d of the dielectric modifiers and MPcs studied.

The results show that *p*-6PF had the lowest γ_s^{tot} (20.6 ± 1.2 mJ·m^2) which was similar to the γ_s^{tot} OTS (24.6 ± 1.2 mJ·m^2). These data explain why the charge mobility of F_{10}-SiPc on *p*-6PF (~0.13 cm^2 V^{-1} s^{-1}) are similar to that reported for OTS. In comparison, *p*-6P had a relatively higher γ_s^{tot} (38.7 ± 0.8 mJ·m^2) which yields a lower charge mobility for F_{10}-SiPc OTFTs compared to mobilities reported for devices made using OTS and *p*-6PF.[47] However, for OTFTs fabricated using CuPc and F_{16}-CuPc on *p*-6P the devices yielded higher mobilities than when using OTS or *p*-6PF as template layer. For CuPc it can be argued that the better performance on *p*-6P is likely a result of matching of γ_s^{tot} while maximizing γ_s^{d} and minimizing γ_s^{p}. This is because *p*-6P has also been shown to the reduce diffusion energy and improve the film morphology of CuPc OTFTs. The same effect is not seen when *p*-6P is used as a template layer on F_{10}-SiPc devices. However, F_{16}-CuPc does not follow either a low surface energy or a match in surface energy correlation because the use *p*-6P led to higher mobilities in F_{16}-CuPc OTFTs compared to using OTS or *p*-6PF. This suggests that surface energy is not the only factor influencing mobility.[47] For instance, the chemical structure of the template layer and its relationship with the semiconductor, as well as the surface coverage of the template layer, can also significantly impact device performance.[47,62] We surmise that additional factors are at play and that some sort of fluorine-fluorine interaction between *p*-6PF and F_{16}-CuPc are leading to poor film structure which is not observed with F_{10}-SiPc. For example, we recently demonstrated that device performance can be increased through fluorine-fluorine interactions between the fluorinated semiconductor and a fluorinated surface.[64]

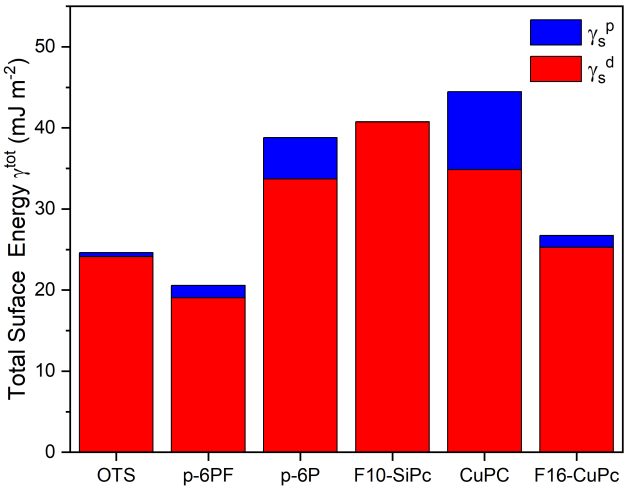

Figure 2.5. *Surface energy components (polar (γ_s^p) and dispersive (γ_s^d)) of the film surfaces measured on SiO_2. p-6P values gotten from literature values (**Table 2.2**).*

To gain insight into the molecular structure versus performance of the MPc on *p*-6P versus *p*-6PF we employed grazing incidence wide angle X-ray scattering (GIWAXS) on the thin film bilayers. Typically, improved device mobility is directly related to the π-π orbital overlap, which is improved when parallel to the substrate which can be achieved in an edge-on orientation of the semiconductor molecules.[28,65] **Figure 2.6** represents the 2D GIWAXS scattering maps of F_{10}-SiPc and F_{16}-CuPc deposited on *p*-6P and *p*-6PF as template layers. To ensure proper comparison GIWAXS experiments were performed on films which were obtained with the same deposition conditions as those used in the OTFT fabrication. However, for the GIWAXS experiments, depositions were performed on plasma-treated Si substrates to minimize the background scattering caused by thick and amorphous SiO_2. To quantify the orientation distribution of the MPcs, we plotted the scattering intensity as a function of azimuthal angle, χ. Where, χ is the angle with respect to the q_z axis. When χ = 0° this lies directly along the out-of-plane (q_z) axis, while χ = 90° lies directly along the in-plane (q_r) axis.[66] The azimuthal integration of the GIWAXS results for F_{10}-SiPc films deposited on *p*-6P and *p*-6PF demonstrated excellent agreement with the powder diffraction pattern for F_{10}-SiPc based on single crystal X-ray diffraction data (**Figure 2.21**). The same is true for F_{16}-CuPc (**Figure 2.22**), and this agreement provides strong confidence in the scattering data used for analyzing the film structure.

A qualitative analysis of the GIWAXS patterns (**Figure 2.6**) shows that the angular intensity distribution is similar for both phthalocyanines when deposited on either *p*-6PF or *p*-6P, indicating similar molecular orientations on either substrate. To determine the angle between the MPs and the substrate, we found a plane that was aligned parallel with the plane of the substrate primarily one with a reflection oriented along q_z, $\chi = 0°$. The calculated angle between MPc and the substrate an aligned plane parallel to the plane of substrate was used to show the primary molecular orientation of the MPc on the substrate (**Figure 6C and F**). The relative degree of crystallinity (rDoC) of the MPcs on different template layer was calculated by normalizing the integrated intensity over a given range of *q*, as outlined in the Experimental Section. The choice of the substrates did have a significant impact on the overall scattering intensity, with significant differences in the rDoC. A more quantitative analysis can be obtained by integrating the most-intense feature at 0.6 $Å^{-1}$ (**Figure 2.23**); this is a combination of the (001), (011) and (010) reflections, which were too closely spaced to be separated. This shows a rDoC of only 0.28 when *p*-6P was used as the template layer for F_{10}-SiPc, as compared to 1 when *p*-6PF was used. Results obtained using the lower-intensity (102) feature (which could be individually resolved) were similar (**Figure 2.24**). This finding strongly supports the improved device mobility of F_{10}-SiPc using a *p*-6PF template (**Table 2.1**) over our recent reports using *p*-6P.[47] In contrast, F_{16}-CuPc exhibited an opposing trend, where the use of *p*-6P resulted in higher crystallinity (rDoC = 1) compared to *p*-6PF (rDoC = 0.31) (**Figure 2.25**). These results are also consistent with reported OTFT reported results where mobility of F_{16}-CuPc using *p*-6P was greater than OTFTs fabricated using *p*-6PF (**Table 2.1**).[44] These results suggest that *p*-6P, a classic templating layer for typical divalent MPcs (such as CuPc and ZnPc), is less effective than *p*-6PF for the crystallization of F_{10}-SiPc. These results further suggest that templating layers should be developed in tandem with high performance semiconductors to high-performance OTFTs.

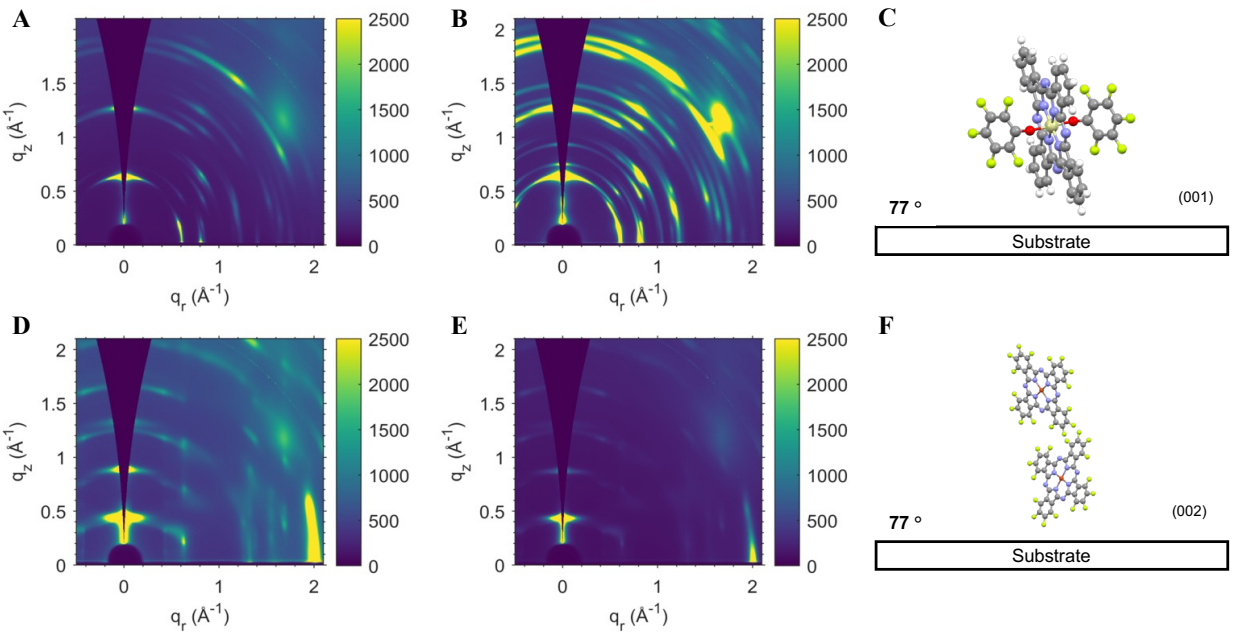

Figure 2.6. *2D GIWAXS patterns of F_{10}-SiPc films on Si substrate (A) with a p-6P (B) and p-6PF template layer, (C) with determined angle between family of planes of F_{10}-SiPc and the substrate (which is parallel to (001) plane) for both templates. (D) F_{16}-CuPc films on Si surface with p-6P (E) and p-6PF template layer (F) with determined angle between family of planes of F_{16}-CuPc and the substrate (which is parallel to (002) plane) for both templates.*

2.3 Conclusion

In this study, we reported the use of a template layer (*p*-6PF) for the WEG of F_{10}-SiPc-, CuPc-, and F_{16}-CuPc-based OTFTs. The results establish the impact of varying deposition thicknesses (2, 4, and 8 nm) and substrate temperatures during deposition (25, 100, 150, and180°C) on the growth morphology and surface coverages of *p*-6PF. We validated the resulting templating layers through incorporation into F_{10}-SiPc OTFTs, which yielded the highest average mobility (0.14cm^{2}V^{-1}s^{-1}) at a *p*-6PF thickness of 8 nm and substrate temperature of 100 °C during deposition. Device mobility and F_{10}-SiPc film crystallinity increased with increasing thicknesses of *p*-6PF at substrate temperatures of 25 and 100 °C during deposition. We found that *p*-6PF had low total surface energy (γ_s^{tot}) similar to that of the OTS, which may be the reason for improved F_{10}-SiPc films compared to *p*-6P· GIWAXS results show that the molecular orientation of both F_{10}-SiPc and F_{16}-CuPc remained unchanged when a *p*-6PF or *p*-6P template was used. However, the crystallinity of F_{10}-SiPc was significantly increased when *p*-6PF was used as the template layer as opposed to *p*-6P, while F_{16}-CuPc exhibited an opposite trend. We demonstrate

the importance of optimizing the deposition conditions of a template layer when applied to the WEG of a semiconductor in OTFTs. Additionally, our results highlight how high-performance OTFTs depend on the simultaneous choice and design of the template layer and the semiconductor.

2.4 Experimental Section

Materials

Copper phthalocyanine (**CuPc**, 90%, TCI P100525G), copper(ii) 1,2,3,4,8,9,10,11,15,16,17,18,22,23,24,25-hexadecafluoro-29*H*,31*H*-phthalocyanine (**F_{16}-CuPc**, >98%, TCI H1194) and para-sexiphenyl (***p*-6P**) were obtained from TCI Chemicals. CuPc was further purified using train sublimation prior to device fabrication. Bis(pentafluorophenoxy) Silicon Phthalocyanine (**F_{10}-SiPc**) was synthesised using previous demonstrated method reported by our group. Per-fluorinated para-sexiphenyl (***p*-6PF**) was synthesized according to a previously reported literature procedure.[67]

Device Fabrication and Characterization

N-doped Ossila Si substrates with a 230 nm thermally grown SiO_2 dielectric layer was rinsed with acetone and isopropanol sequentially. The substrates were dried with a nitrogen stream and were cleaned by sonicating using a VWR ultrasonic cleaner (Model No: 97043-964) in acetone and methanol sequentially for 5 mins. After sonication, the substrates were dried with a nitrogen stream and cleaned in a Harrick plasma cleaner (PDC32G1 060198) under vacuum for 15 mins. The cleaned substrates were then transported into a nitrogen glove box for the deposition of *p*-6PF. The substrates were placed in a square shadow mask and different thicknesses of *p*-6PF were deposited by physical vapour deposition (PVD) using an Angstrom Engineering Evaporator with a stage height of 50 cm between the source and substrate at a rate of 0.05 $Å \cdot s^{-1}$ under vacuum ($P < 2 \times 10^{-6}$ Torr). The substrate holder was rotated during all depositions using an Oriental Motor (5IK60RGU-CU) at 25 RPM. For depositions above room temperature (100, 150 and 180 °C), the substrates were heated to the desired temperature and soaked for 1 h to reach thermal equilibrium. After *p*-6PF deposition, the substrates were left to cool to room temperature overnight. F_{10}-SiPc devices were then fabricated by thermally

depositing a 50 nm-thick layer of F_{10}-SiPc at ambient temperature acting as the organic semiconductor. The deposition of F_{10}-SiPc was carried out at a rate of 0.2 Å·s^{-1} under vacuum (P < 2×10^{-6} Torr). After *p*-6PF deposition CuPc and F_{16}-CuPc devices were also fabricated by thermally depositing a 15 nm-thick layer of the semiconductor at a rate of 0.3 Å·s^{-1} under vacuum (P < 2×10^{-6} Torr) on a heated substrate at 140 °C and soaked at for 1 h before deposition. After semiconductor depositions diamond tipped pen was used to scratch the corner of the substrates along the long edge to expose the Si base for deposition of the gate electrodes. The substrates were then placed in a source-drain shadow mask (L = 30 µm, W = 1000 µm) purchased from Ossila. Electrodes were fabricated by deposition of 10 nm of a manganese as contact interlayer at 0.5 Å·s^{-1} and 50 nm-thick layer of silver at a rate of 2 Å·s^{-1} at a base pressure of P < 2×10^{-6} Torr for F_{10}-SiPc devices. CuPc and F_{16}-CuPc based devices were fabricated with 50 nm-thick layer of gold as the electrodes which was deposited at a rate of 1 Å·s^{-1} at a base pressure of P < 2×10^{-6} Torr. All final films were patterned to have 20 transistors per substrate.

For electrical characterization OTFTs were transferred between glove boxes in a nitrogen filled airtight container. The oxygen and moisture concentration of both glove boxes are kept below 1 ppm. The testing glove box was equipped with a custom-built auto tester and Keithley 2614B source meter. The tips of the auto tester contact the source, drain, and gate electrodes of the bottom gate top contact (BGTC) OTFT. The auto tester was operated by a Keithley 2614B source meter with a custom LabVIEW program which allowed to set gate–source voltage (V_{GS}) and source–drain voltage (V_{SD}) while measuring the source–drain current (I_{SD}) in the devices. For each substrate (n ≤ 20 devices) output curves were collected by sweeping the V_{SD} while maintaining a constant V_{GS}. Transfer curves were collected by sweeping the V_{GS} and holding the V_{SD}. This was repeated four times to achieve stable performance. For all measurements the fourth run was used to evaluate device performance. The device performance characteristics were collected in the saturation regime using Eq 1.

$$I_{DS} = \frac{\mu C_i W}{2L}(V_{GS} - V_T)^2 \qquad 1$$

Where μ is the field mobility of the semiconductor, and L and W represent the length and width of the channel respectively. C_i is the capacitance of the dielectric layer

and V_T is the threshold voltage. μ and V_T are calculated by measuring the slope and x-intercept respectively of the linearized transfer curve ($\sqrt{I_{DS}}\ vs\ V_{GS}$) using Eq 2

$$\sqrt{I_{DS}} = \sqrt{\frac{\mu_e C_i W}{2L}}(V_{GS} - V_T) \qquad 2$$

Finally, the on/off ratio of the devices is calculated as the ratio of measured maximum (I_{on}) and minimum (I_{off}) current achieved in the operational voltage range of the transfer curves.

Contact Angle Measurement

Contact angle measurement was performed by making use of a VCA Optima goniometer from AST Product Inc. The syringe was programmed to dispense 1 µL of deionized water or diiodomethane. The image of the droplet was captured as soon as it contacted the surface of the substrate. The surface energy was calculated by solving the system of equations for deionized water and diiodomethane with Fowkes model equation presented below in Eq 3.[63]

$$1 + \cos\theta = \frac{2(\gamma_s^d)^{\frac{1}{2}}(\gamma_{lv}^d)^{1/2}}{\gamma_{lv}} + \frac{2(\gamma_s^p)^{\frac{1}{2}}(\gamma_{lv}^p)^{1/2}}{\gamma_{lv}} \qquad 3$$

where cos θ is the measured contact angle of the respective liquids on the surface of the substrate, γ_{lv}^d and γ_{lv}^p are the liquid dispersive and polar surface energy of the respective liquid, γ_{lv} is the total liquid surface energy of the reference liquid and is a combination of γ_{lv}^d and γ_{lv}^p, γ_s^d and γ_s^p are the dispersive and polar solid surface energy of the substrates and γ^{tot} is the total solid surface energy and is also a combination of γ_s^d and γ_s^p. The reference liquid surface energy parameters used were γ_{lv}^d = 21.8 mJ.m^{-2}, γ_{lv}^p = 51.0 mJ.m^{-2}, and γ_{lv} = 72.8 mJ.$^{m\text{-}2}$ for deionized water and γ_{lv}^d = 49.5 mJ.m^{-2}, γ_{lv}^p = 1.3 mJ.m^{-2}, and γ_{lv} = 50.8 mJ.m^{-2} for diiodomethane.[68,69]

Atomic Force Microscopy (AFM)

Atomic force microscopy was carried out using a Bruker Dimension Icon microscope in tapping mode using NCHV-A tips (320 kHz, 40 N/m, 8 nm radius).

Film X-ray Diffraction

Film X-ray diffraction data was collected using a Rigaku Ultima IV powder diffractometer with an X-ray source of Cu at a scan rate of 0.5 θ min^{-1} and scan range of $3° < 2\theta < 20°$

Grazing-Incidence Wide-Angle X-ray Scattering (GIWAXS)

GIWAXS experiments were performed at the Brockhouse X-ray Diffraction and Scattering Beamlines–Low Energy Wiggler (BXDS-WLE) beamline at the Canadian Light Source (CLS) with a photon energy of 15.1 keV (λ = 0.8202 Å) and in a grazing incidence (reflection) geometry. All samples were collected using a Rayonix MX300 CCD detector (73.242 μm × 73.242 μm pixel size), with an angle of incidence of θ=0.01-0.05°. Silver behenate (AgBeh) standards were used to calibrate all data using the GIXSGUI software package in MATLAB.

Relative Degree of Crystallinity Calculation (rDoC).

The relative degree of crystallinity was calculated by integrating the scattering intensity across χ as in Equation 4:

$$rDoC \propto \int_0^{\pi/2} \sin(\chi)\, I(\chi) d\chi \quad (4)$$

To determine rDoC, *I*(χ) × Sin(χ) was plotted against χ for a single Bragg peak by integrating over a given range of q. This was done for both samples. The results were normalized, assigning rDoC = 1 to the most crystalline sample. All samples were measured with the same detector integration time, and with the same scattering volume.

Acknowledgements

We thank the Natural Sciences and Engineering Research Council of Canada (NSERC, RGPIN-2020-04079 to B.H.L., RGPIN-2022-03138 to T.L.K., and CGS-D to B.K.). We also thank the Canada Research Chair program for supporting D.S.S., T.L.K., and B.H.L. The Canadian Light Source (CLS) was supported by the Canadian Foundation for Innovation (CFI), NSERC, the University of Saskatchewan, the Government of Saskatchewan, Western Economic Diversification Canada, and the Canadian Institutes of Health Research. The authors acknowledge the Centre for Research in Photonics at

the University of Ottawa for access to the AFM. Technical support from the BXDS beamline scientist Dr. Adam Leontowich is gratefully acknowledged.

Supporting Information

Nuclear Magnetic Resonance Spectroscopy

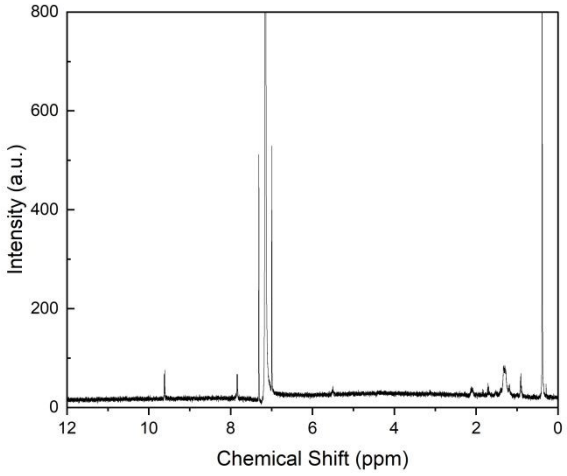

Figure 2.7. *^{1}H NMR spectra of F_{10}-SiPc*

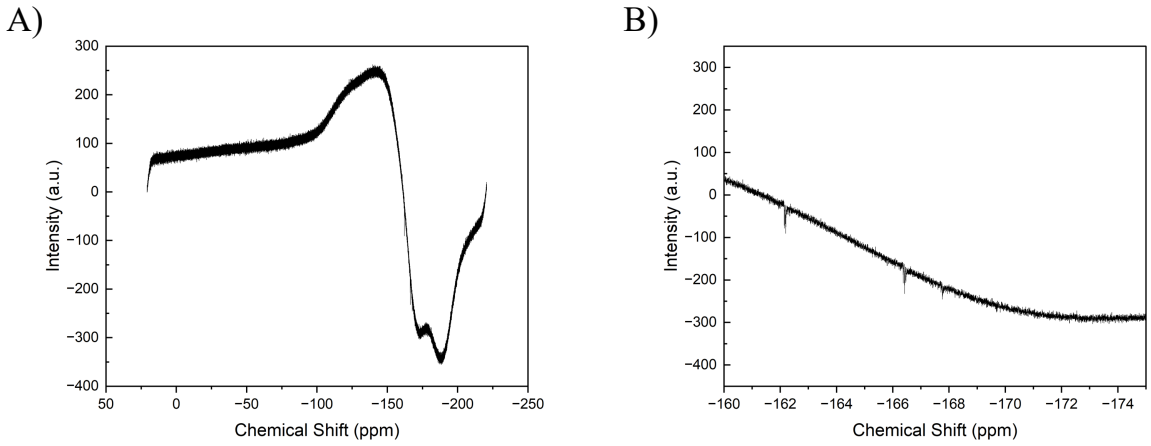

Figure 2.8. *^{19}F NMR spectra of F_{10}-SiPc*

Atomic forced microscopy (AFM)

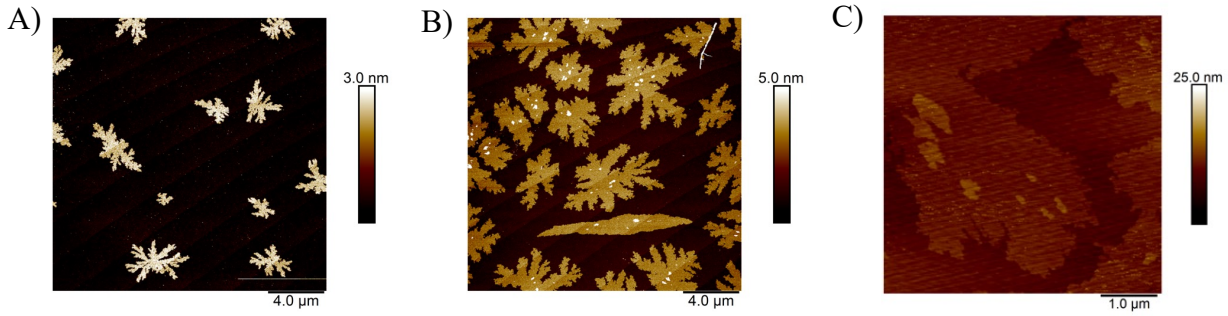

Figure 2.9. *AFM images (5 µm × 5 µm) of (A) 2 nm of p-6PF, (B) 4 nm, and (C) 8 nm deposited at a substrate temperature of 100 °C.*

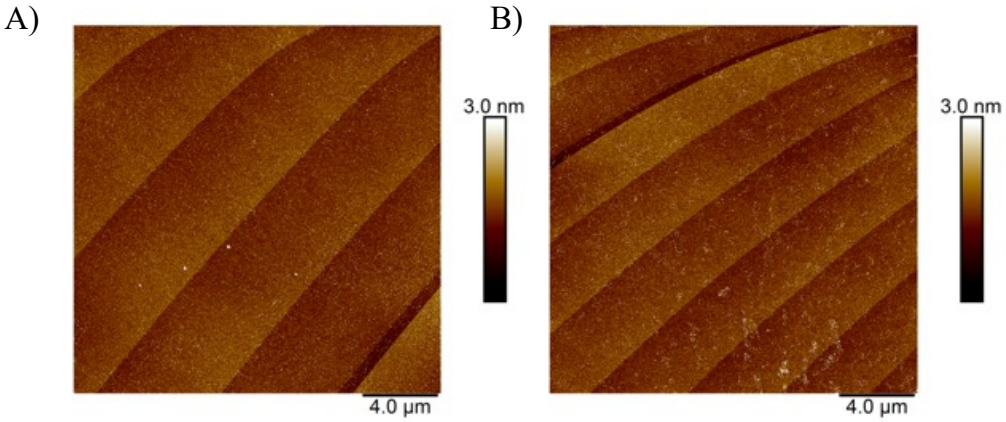

Figure 2.10. *AFM images (5 µm × 5 µm) of (A) 2 nm of p-6PF, (B) 4 nm, and (C) 8 nm deposited at a substrate temperature of 100 °C.*

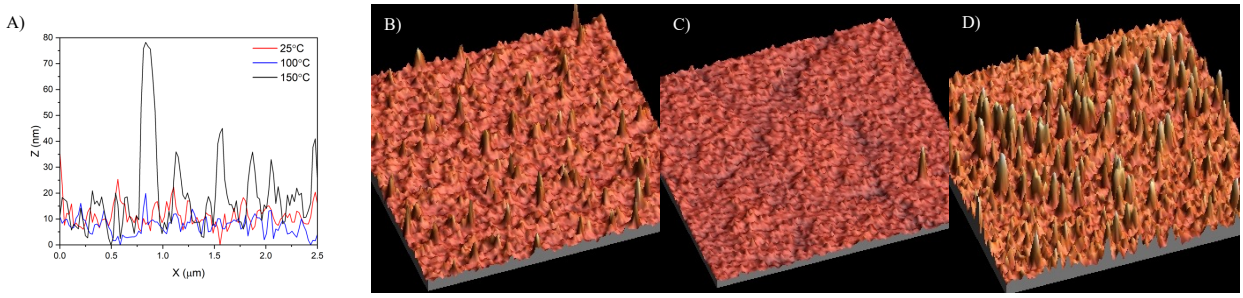

Figure 2.11. *AFM images (5 µm × 5 µm) of 50 nm F_{10}-SiPc deposited on 2 nm (A) and 4 nm (B) p-6PF thin films prepared at 180 °C.*

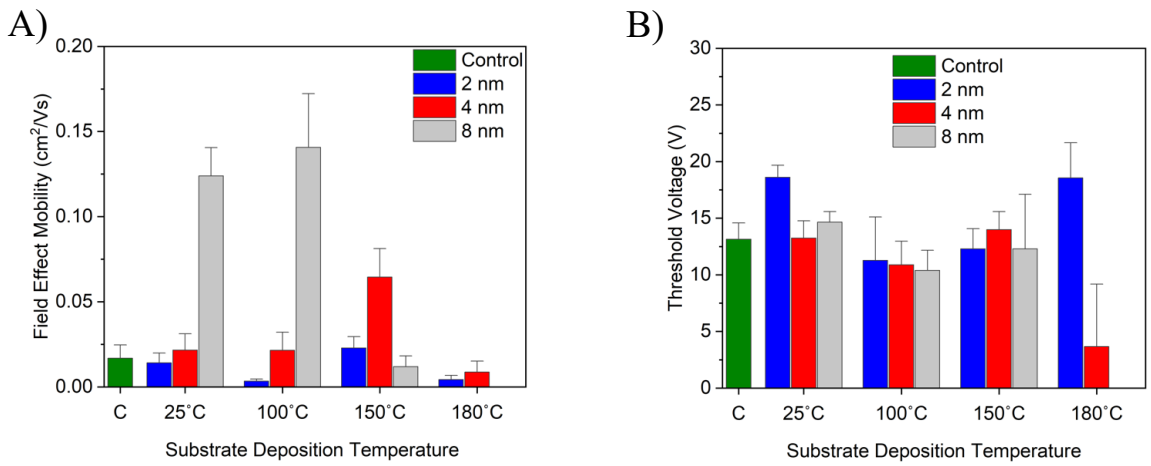

Figure 2.12. *Average saturation region (A) mobility (cm^2/Vs) and (B) threshold voltage (V) F_{10}-SiPc OTFTs with different thicknesses of the p-6PF deposited at difference substrate temperatures.*

Output and Transfer Curves

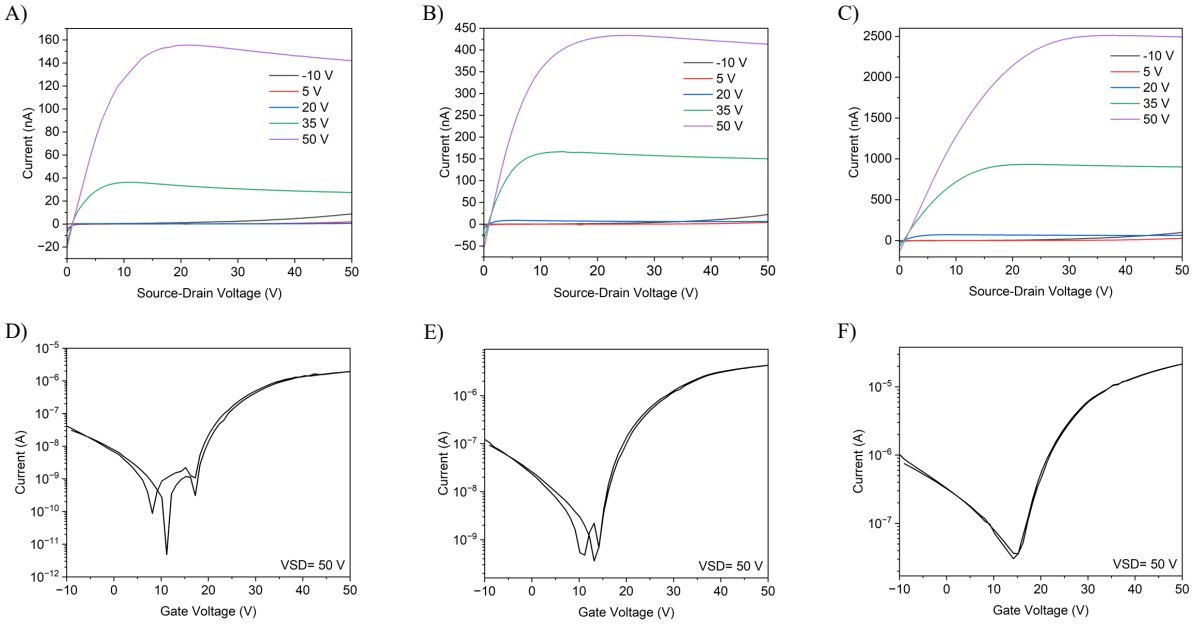

Figure 2.13. *Output curves of F_{10}-SiPc OTFTs on p-6PF substrates prepared at 25 °C with thicknesses of (A) 2, (B) 4, and (C) 8 nm, respectively. Corresponding transfer curves for each device are shown in (D), (E), and (F).*

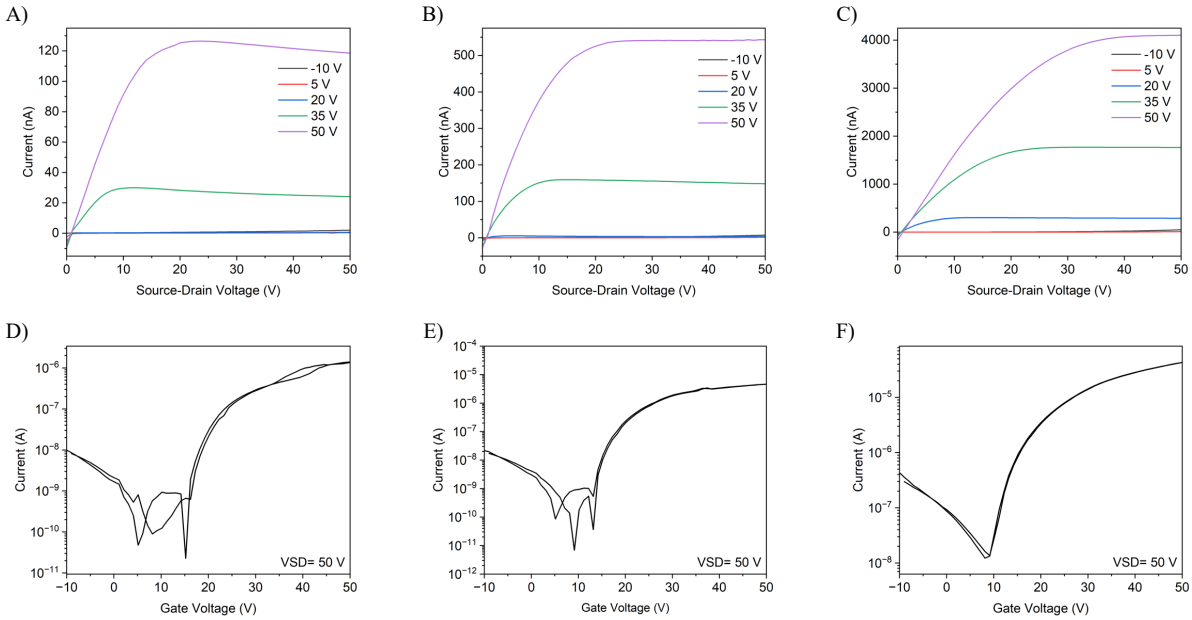

Figure 2.14. *Output curves of F_{10}-SiPc OTFTs on p-6PF substrates prepared at 100 °C with thicknesses of (A) 2, (B) 4, and (C) 8 nm, respectively. Corresponding transfer curves for each device are shown in (D), (E), and (F).*

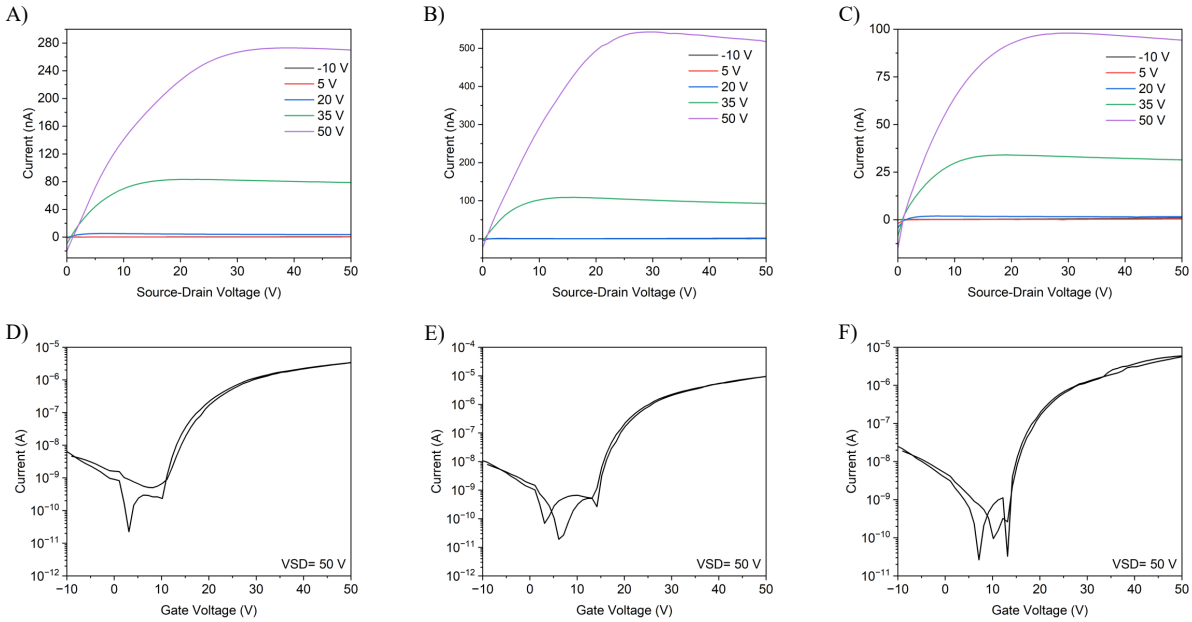

Figure 2.15. *Output curves of F_{10}-SiPc OTFTs on p-6PF substrates prepared at 150 °C with thicknesses of (A) 2, (B) 4, and (C) 8 nm, respectively. Corresponding transfer curves for each device are shown in (D), (E), and (F).*

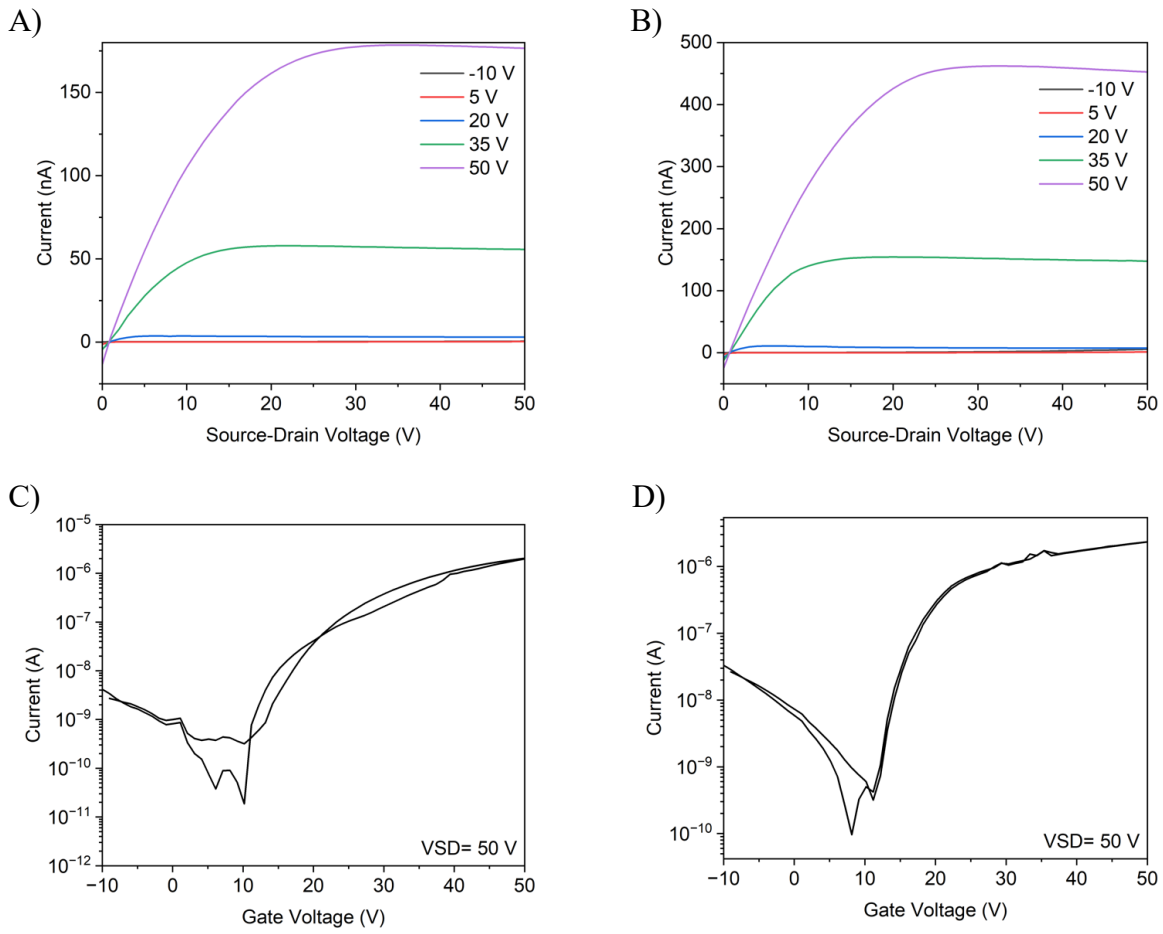

Figure 2.16. *Output of F_{10}-SiPc OTFTs on p-6PF substrates prepared at 180 °C with thicknesses of (A) 2, and (B) 4 nm, respectively. Corresponding transfer curves for each device are shown in (C), and (D).*

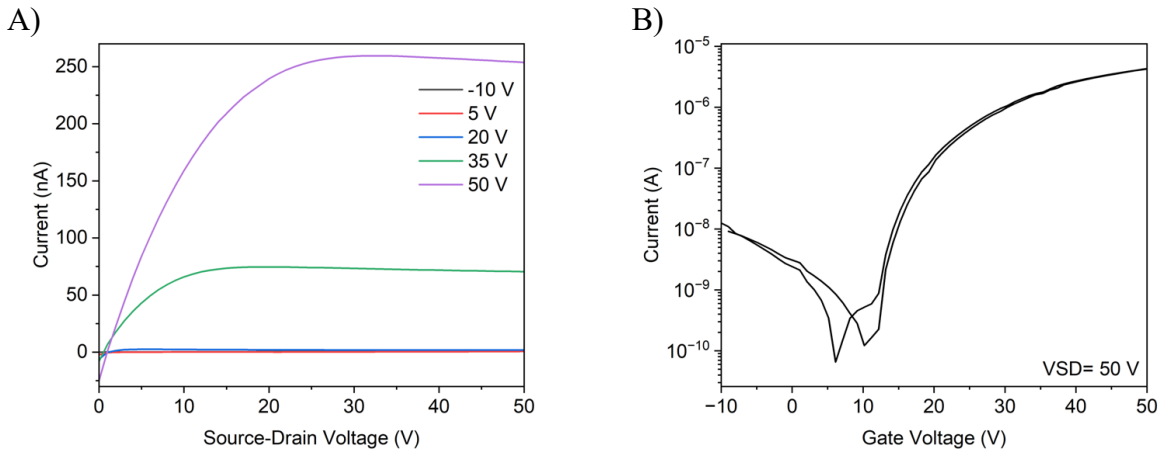

Figure 2.17. *Output curves of F_{10}-SiPc OTFTs on bare SiO_2. (B) Corresponding transfer curve.*

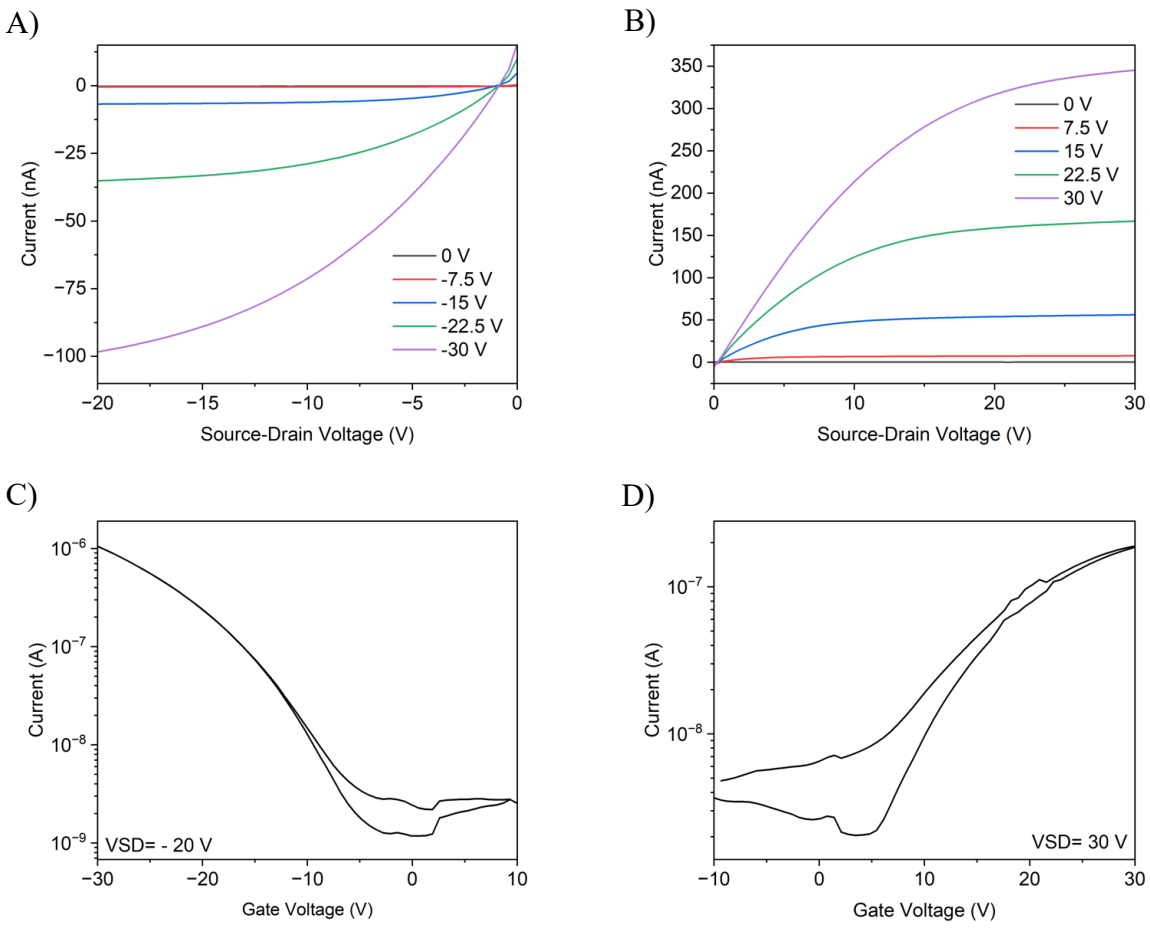

Figure 2.18. *Output of OTFTs on p-6PF substrates prepared at 100 °C with a thickness of 8 nm, using (A) CuPc and (B) F_{16}-CuPc as active layers. Corresponding transfer curves for each device are shown in (C) and (D), respectively.*

Contact Angle

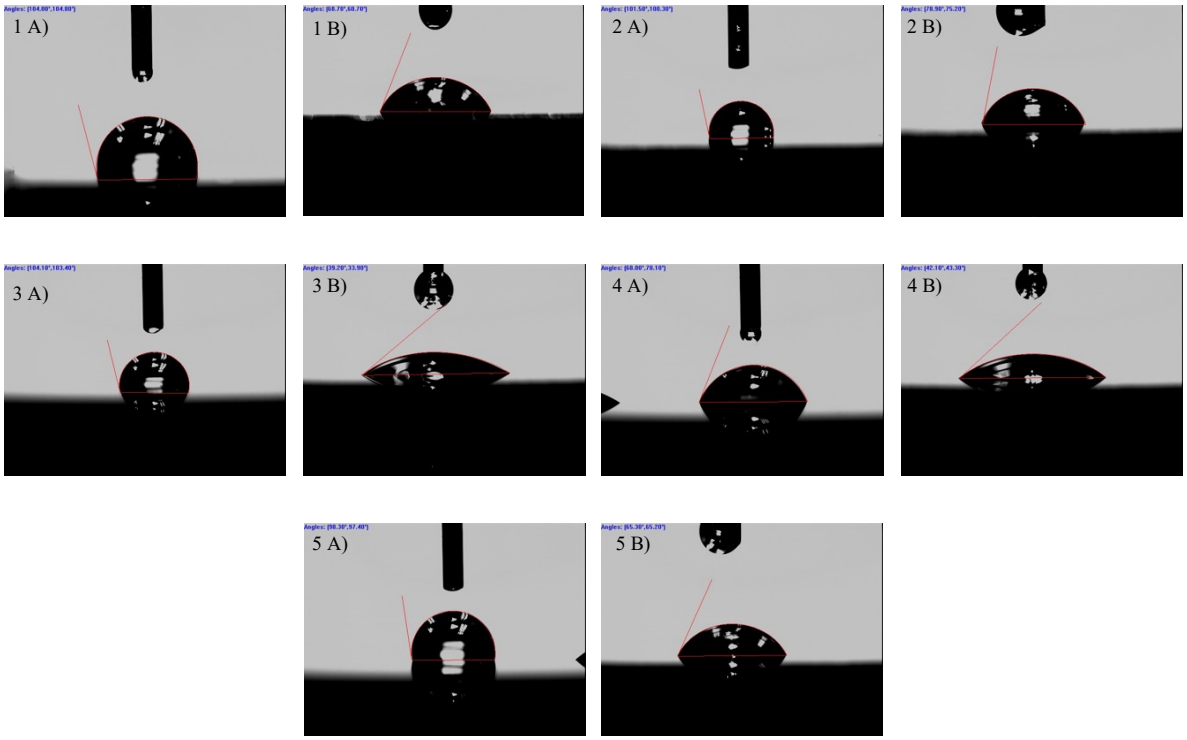

Figure 2.19. *Contact angle measurements of deionized water (A) and diiodomethane (B) on materials (1) OTS, (2) p-6PF, (3) F_{10}-SiPc, (4) CuPc, and (5) F_{16}-CuPc, evaporated on a 230 nm SiO_2 substrate.*

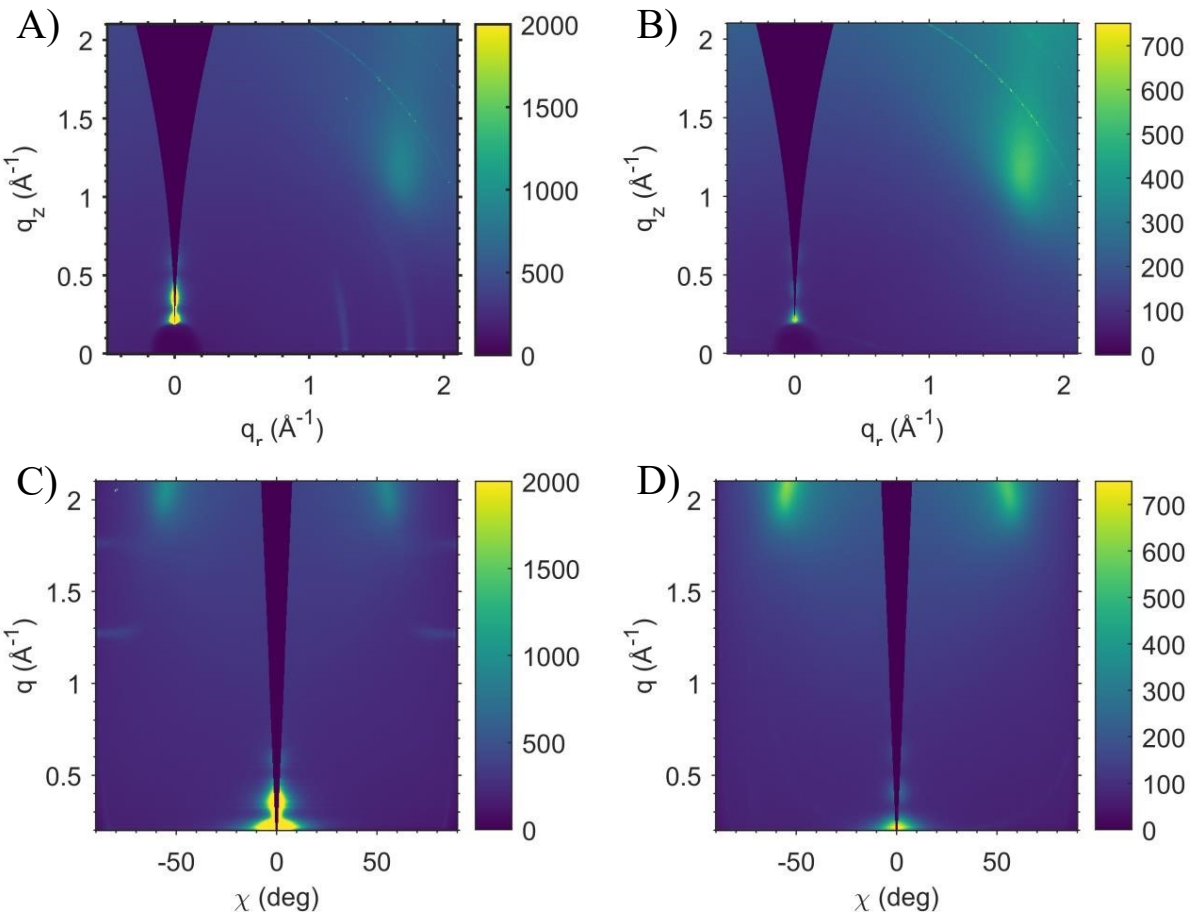

Figure 2.20. *2D GIWAXS patterns of (A) p-6P and (B) p-6PF films on Si substrate. 2D GIWAXS patterns of (C) p-6P and (D) p-6PF film represented with the azimuthal angle on Si substrate.*

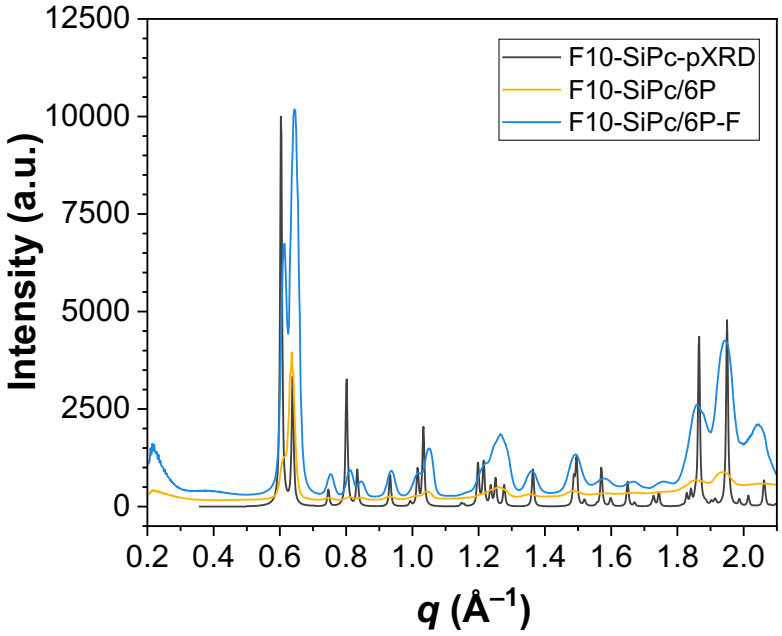

***Figure 2.21**. Azimuthally integrated GIWAXS pattern of F_{10}-SiPc on p-6PF and p-6P with pXRD of F_{10}-SiPc.*

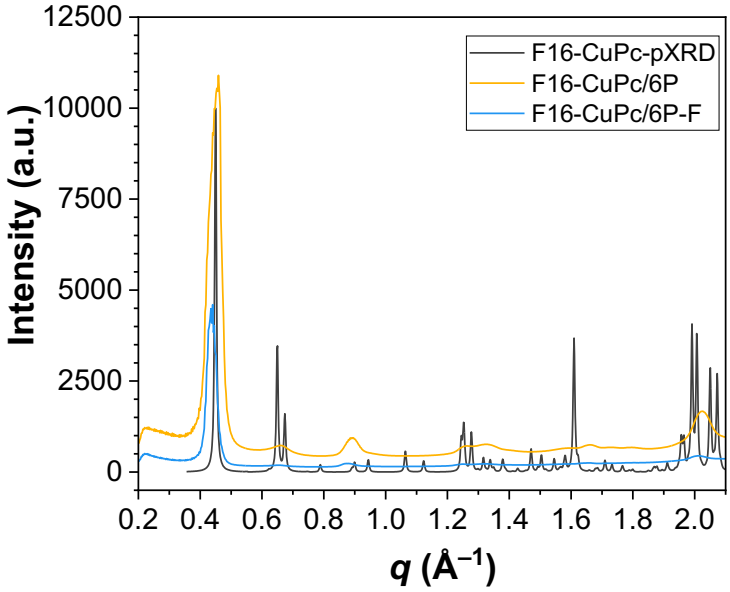

***Figure 2.22**. Azimuthally integrated GIWAXS pattern of F_{16}-CuPc on p-6PF and p-6P with PXRD of F_{16}-CuPc.*

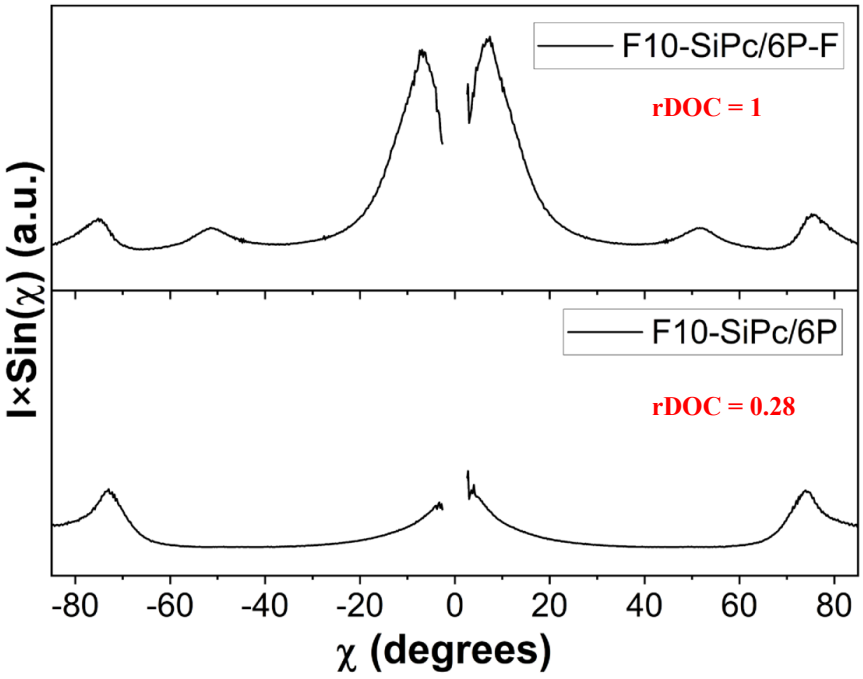

Figure 2.23. *Linecut of F_{10}-SiPc evaporated on p-6PF and p-6P, corresponding to the (001) plane.*

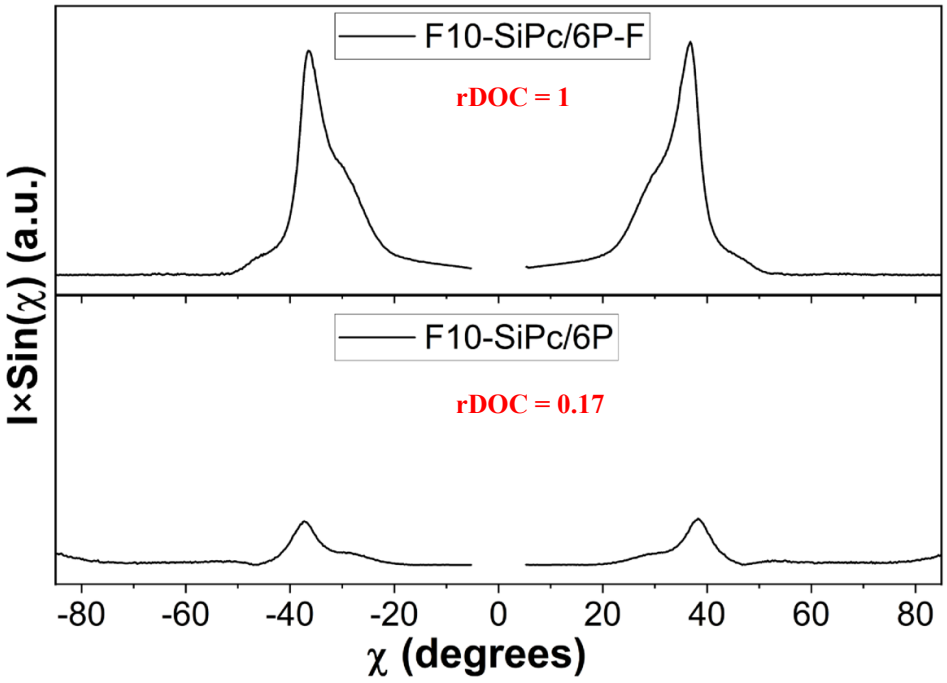

Figure 2.24. *Linecut of F_{10}-SiPc evaporated on p-6PF and p-6P, corresponding to the (102) plane.*

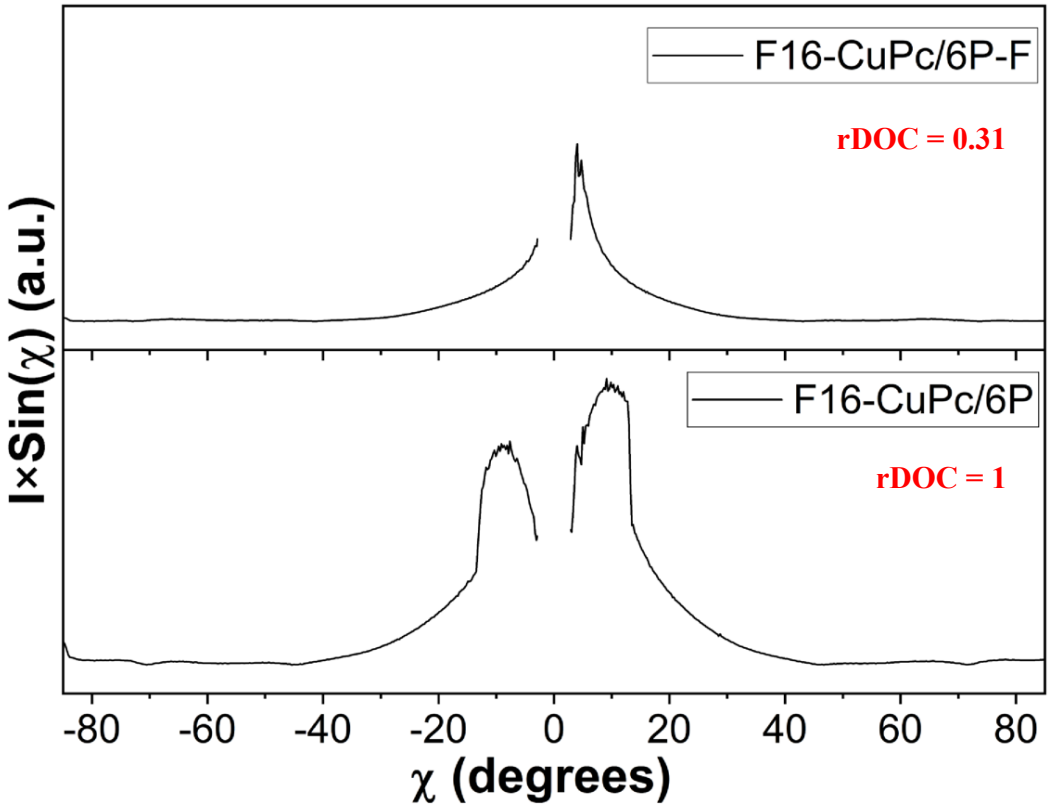

Figure 2.25. *Linecut of F_{16}-CuPc evaporated on p-6PF and p-6P, corresponding to the (002) plane.*

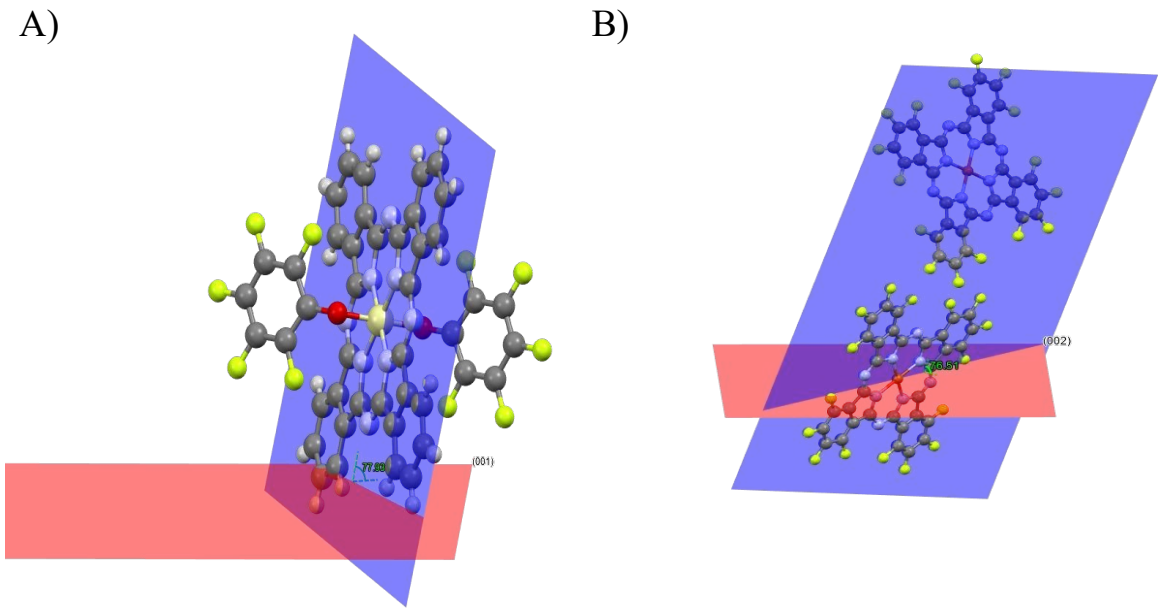

Figure 2.26. *Determined angle between family of planes of (A) F_{10}-SiPc and the substrate (which is parallel to (001) plane) and (B) F_{16}-CuPc and the substrate (which is parallel to (002) plane) on p-6P and p-6PF as template layer.*

References

(1) Braga, D.; Horowitz, G. High-Performance Organic Field-Effect Transistors. *Advanced materials (Weinheim)* **2009**, *21* (14–15), 1473–1486.

(2) Kim, J.; Kim, J.; Ahn, B.; Hassinen, T.; Jung, Y.; Ko, S. Optimization and Improvement of TIPS–Pentacene Transistors (OTFT) with UV–Ozone and Chemical Treatments Using an All-Step Solution Process. *Current applied physics* **2015**, *15* (10), 1238–1244. https://doi.org/10.1016/j.cap.2015.07.012.

(3) Reese, C.; Roberts, M.; Ling, M.; Bao, Z. Organic Thin Film Transistors. *Materials Today* **2004**, *7* (9), 20–27. https://doi.org/10.1016/S1369-7021(04)00398-0.

(4) Choi, Y.; Song, C. K. Low Leakage Current through Zirconium Oxide Gate Fabricated by Low Temperature Solution Process in OTFTs on Plastic Substrate. *Organic electronics* **2018**, *52*, 195–199. https://doi.org/10.1016/j.orgel.2017.10.030.

(5) Choi, J.; Kang, J.; Lee, C.; Jeong, K.; Im, S. G. Heavily Crosslinked, High-k Ultrathin Polymer Dielectrics for Flexible, Low-Power Organic Thin-Film Transistors (OTFTs). *Advanced electronic materials* **2020**, *6* (8), 2000314-n/a. https://doi.org/10.1002/aelm.202000314.

(6) Feng, L.; Xu, X.; Guo, X. Comparative Analysis of Organic Thin Film Transistor Structures for Flexible E-Paper and AMOLED Displays; 2011; Vol. 37, pp 105–112. https://doi.org/10.1149/1.3600730.

(7) Xie, T.; Xie, G.; Du, H.; Su, Y.; Ye, Z.; Chen, Y.; Jiang, Y. Two Novel Methods for Evaluating the Performance of OTFT Gas Sensors. *Sensors and actuators. B, Chemical* **2016**, *230*, 176–183. https://doi.org/10.1016/j.snb.2015.12.056.

(8) Chen, H.; Luo, D.; Li, Q.; Ma, X.; Liu, H.; Liu, L. OTFT Biosensor on Flexible Substrates for Human Health Monitoring: A Review. *IEEE sensors journal* **2023**, *23* (2), 997–1011. https://doi.org/10.1109/JSEN.2022.3221110.

(9) Grau, G.; Kitsomboonloha, R.; Swisher, S. L.; Kang, H.; Subramanian, V. Printed Transistors on Paper: Towards Smart Consumer Product Packaging. *Advanced functional materials* **2014**, *24* (32), 5067–5074. https://doi.org/10.1002/adfm.201400129.

(10) Tousignant, M. N.; Rice, N. A.; Niskanen, J.; Richard, C. M.; Ritaine, D.; Adronov, A.; Lessard, B. H. High Performance Organic Electronic Devices Based on a Green Hybrid Dielectric. *Advanced electronic materials* **2021**, *7* (10), 2100700-n/a.

(11) Lamontagne, H. R.; Comeau, Z. J.; Cranston, R. R.; Boileau, N. T.; Harris, C. S.; Shuhendler, A. J.; Lessard, B. H. Chloro Aluminum Phthalocyanine-Based Organic Thin-Film Transistors as Cannabinoid Sensors: Engineering the Thin Film Response. *Sensors & diagnostics* **2022**, *1* (6), 1165–1175. https://doi.org/10.1039/D2SD00071G.

(12) Peltekoff, A. J.; Brixi, S.; Niskanen, J.; Lessard, B. H. Ionic Liquid Containing Block Copolymer Dielectrics: Designing for High-Frequency Capacitance, Low-Voltage Operation, and Fast Switching Speeds. *Journal of the American Chemical Society* **2021**, *1* (7), 1044–1056. https://doi.org/10.1021/jacsau.1c00133.

(13) Peltekoff, A. J.; Tousignant, M. N.; Hiller, V. E.; Melville, O. A.; Lessard, B. H. Controlled Synthesis of Poly(Pentafluorostyrene-Ran-Methyl Methacrylate) Copolymers by Nitroxide Mediated Polymerization and Their Use as Dielectric Layers in Organic Thin-Film Transistors. *Polymers* **2020**, *12* (6). https://doi.org/10.3390/POLYM12061231.

(14) Shukla, D.; Nelson, S. F.; Freeman, D. C.; Rajeswaran, M.; Ahearn, W. G.; Meyer, D. M.; Carey, J. T. Thin-Film Morphology Control in Naphthalene-Diimide-Based Semiconductors: High Mobility n-Type Semiconductor for Organic Thin-Film Transistors. *Chemistry of materials* **2008**, *20* (24), 7486–7491.
(15) Vebber, M. C.; King, B.; French, C.; Tousignant, M.; Ronnasi, B.; Dindault, C.; Wantz, G.; Hirsch, L.; Brusso, J.; Lessard, B. H. From P-type to N-type: Peripheral Fluorination of Axially Substituted Silicon Phthalocyanines Enables Fine Tuning of Charge Transport. *Canadian journal of chemical engineering* **2023**, *101* (6), 3019–3031. https://doi.org/10.1002/cjce.24843.
(16) Pak, K.; Seong, H.; Choi, J.; Hwang, W. S.; Im, S. G. Synthesis of Ultrathin, Homogeneous Copolymer Dielectrics to Control the Threshold Voltage of Organic Thin-Film Transistors. *Advanced functional materials* **2016**, *26* (36), 6574–6582. https://doi.org/10.1002/adfm.201602585.
(17) Borthakur, T.; Sarma, R. Performance Enhancement of Top Contact Pentacene-Based Organic Thin-Film Transistor (OTFT) Using Perylene Interlayer between Organic/Electrode Interface. *Appl. Phys. A* **2017**, *123* (3), 1–5. https://doi.org/10.1007/s00339-017-0836-2.
(18) Tai, H.; Zhang, B.; Duan, C.; Xie, G.; Jiang, Y. The Effect of MWCNTs on the Performance of α-Sexithiophene OTFT Device and Its Gas-Sensing Property. *Sci. China Technol. Sci* **2014**, *57* (6), 1101–1108. https://doi.org/10.1007/s11431-014-5539-8.
(19) Lever, A. B. P. The Phthalocyanines. In *Advances in Inorganic Chemistry and Radiochemistry*; Emeléus, H. J., Sharpe, A. G., Eds.; Academic Press, 1965; Vol. 7, pp 27–114. https://doi.org/10.1016/S0065-2792(08)60314-3.
(20) Vebber, M. C.; Grant, T. M.; Brusso, J. L.; Lessard, B. H. Bis(Trialkylsilyl Oxide) Silicon Phthalocyanines: Understanding the Role of Solubility in Device Performance as Ternary Additives in Organic Photovoltaics. *Langmuir* **2020**, *36* (10), 2612–2621. https://doi.org/10.1021/acs.langmuir.9b03772.
(21) Tian, X.; Xu, Z.; Zhang, F.; Zhao, S.; Yuan, G.; Li, J.; Sun, Q.; Wang, Y. Influence of Thermal Treatment on the Performance of Copper Phthalocyanine Thin-Film Transistors. *Current applied physics* **2010**, *10* (1), 129–132. https://doi.org/10.1016/j.cap.2009.05.008.
(22) Namgoong, J. W.; Kim, S. H.; Chung, S.-W.; Kim, Y. H.; Kwak, M. S.; Kim, J. P. Aryloxy- and Chloro-Substituted Zinc(II) Phthalocyanine Dyes: Synthesis, Characterization, and Application for Reducing the Thickness of Color Filters. *Dyes and Pigments* **2018**, *154*, 128–136. https://doi.org/10.1016/j.dyepig.2018.01.024.
(23) Melville, O. A.; Lessard, B. H.; Bender, T. P. Phthalocyanine-Based Organic Thin-Film Transistors: A Review of Recent Advances. *ACS Applied Materials and Interfaces* **2015**, *7* (24), 13105–13118. https://doi.org/10.1021/acsami.5b01718.
(24) Lessard, B. H. The Rise of Silicon Phthalocyanine: From Organic Photovoltaics to Organic Thin Film Transistors. *ACS Applied Materials and Interfaces* **2021**, *13* (27), 31321–31330. https://doi.org/10.1021/acsami.1c06060.
(25) Melville, O. A.; Grant, T. M.; Lessard, B. H. Silicon Phthalocyanines as N-Type Semiconductors in Organic Thin Film Transistors. *Journal of Materials Chemistry C* **2018**, *6* (20), 5482–5488. https://doi.org/10.1039/c8tc01116h.

(26) King, B.; Vebber, M. C.; Ewenike, R.; Dupuy, M.; French, C.; Brusso, J. L.; Lessard, B. H. Peripherally Fluorinated Silicon Phthalocyanines: How Many Fluorine Groups Are Necessary for Air-Stable Electron Transport in Organic Thin-Film Transistors? *Chem. Mater.* **2023**. https://doi.org/10.1021/acs.chemmater.3c01342.
(27) Cranston, R. R.; Lessard, B. H. Metal Phthalocyanines: Thin-Film Formation, Microstructure, and Physical Properties. *RSC Advances* **2021**, *11* (35), 21716–21737. https://doi.org/10.1039/d1ra03853b.
(28) Yang, J.; Yan, D.; Jones, T. S. Molecular Template Growth and Its Applications in Organic Electronics and Optoelectronics. *Chem. Rev.* **2015**, *115* (11), 5570–5603. https://doi.org/10.1021/acs.chemrev.5b00142.
(29) Qian, C.; Sun, J.; Kong, L.-A.; Gou, G.; Zhu, M.; Yuan, Y.; Huang, H.; Gao, Y.; Yang, J. High-Performance Organic Heterojunction Phototransistors Based on Highly Ordered Copper Phthalocyanine/Para-Sexiphenyl Thin Films. *Advanced Functional Materials* **2017**, *27* (6), 1604933. https://doi.org/10.1002/adfm.201604933.
(30) Wang, H.; Zhu, F.; Yang, J.; Geng, Y.; Yan, D. Weak Epitaxy Growth Affording High-Mobility Thin Films of Disk-Like Organic Semiconductors. *Advanced materials (Weinheim)* **2007**, *19* (16), 2168–2171. https://doi.org/10.1002/adma.200602566.
(31) Liu, L.; Li, C.; Li, Z.; Sun, P.; Zhu, F.; Wang, Y.; Yan, D. Highly Oriented Crystalline Thin Film with High Electroluminescence Performance Fabricated by Weak Epitaxy Growth. *Organic Electronics* **2020**, *84*, 105806. https://doi.org/10.1016/j.orgel.2020.105806.
(32) Lizhen Huang; Chengfang Liu; Bo Yu; Jidong Zhang; Yanhong Geng; Donghang Yan. Evolution of 2,5-Bisbithiophene Thin Films and Its Effect on the Weak Epitaxy Growth of ZnPc. *The journal of physical chemistry. B* **2010**, *114* (14), 4821.
(33) Andreev, A.; Sitter, H.; Brabec, C. J.; Hinterdorfer, P.; Springholz, G.; Sariciftci, N. S. Self-Assembled Growth of Highly Oriented Para- Sexiphenyl Thin Films. *Synthetic metals* **2001**, *121* (1), 1379–1380. https://doi.org/10.1016/S0379-6779(00)00966-8.
(34) Yang, J.; Wang, T.; Wang, H.; Zhu, F.; Li, G.; Yan, D. Ultrathin-Film Growth of Para-Sexiphenyl (II): Formation of Large-Size Domain and Continuous Thin Film. *The journal of physical chemistry. B* **2008**, *112* (26), 7821–7825. https://doi.org/10.1021/jp711457p.
(35) Andreev, A.; Sitter, H.; Sariciftci, N. S.; Brabec, C. J.; Springholz, G.; Hinterdorfer, P.; Plank, H.; Resel, R.; Thierry, A.; Lotz, B. Highly Ordered Anisotropic Nano-Needles in Para-Sexiphenyl Films. *Thin solid films* **2002**, *403*, 444–448. https://doi.org/10.1016/S0040-6090(01)01587-5.
(36) Resel, R. Surface Induced Crystallographic Order in Sexiphenyl Thin Films. *Journal of physics. Condensed matter* **2008**, *20* (18), 184009-184009 (10). https://doi.org/10.1088/0953-8984/20/18/184009.
(37) Yang, J.; Wang, T.; Wang, H.; Zhu, F.; Li, G.; Yan, D. Ultrathin-Film Growth of Para-Sexiphenyl (I): Submonolayer Thin-Film Growth as a Function of the Substrate Temperature. *J. Phys. Chem. B* **2008**, *112* (26), 7816–7820. https://doi.org/10.1021/jp711455u.
(38) Sparenberg, M.; Zykov, A.; Beyer, P.; Pithan, L.; Weber, C.; Garmshausen, Y.; Carlà, F.; Hecht, S.; Blumstengel, S.; Henneberger, F.; Kowarik, S. Controlling the Growth Mode of Para-Sexiphenyl (6P) on ZnO by Partial Fluorination. *Physical*

chemistry chemical physics : PCCP **2014**, *16* (47), 26084–26093. https://doi.org/10.1039/c4cp04048a.

(39) Fu, C.; Orgiu, E.; Perepichka, D. F. Face-on vs. Edge-on: Tuning the Structure of Tetrathiafulvalene Monolayers with Solvent. *J. Mater. Chem. C* **2018**, *6* (14), 3787–3791. https://doi.org/10.1039/C7TC05757A.

(40) Lipton-Duffin, J. A.; Miwa, J. A.; Kondratenko, M.; Cicoira, F.; Sumpter, B. G.; Meunier, V.; Perepichka, D. F.; Rosei, F. Step-by-Step Growth of Epitaxially Aligned Polythiophene by Surface-Confined Reaction. *Proceedings of the National Academy of Sciences* **2010**, *107* (25), 11200–11204. https://doi.org/10.1073/pnas.1000726107.

(41) Song, D.; Zhu, F.; Yu, B.; Huang, L.; Geng, Y.; Yan, D. Tin (IV) Phthalocyanine Oxide: An Air-Stable Semiconductor with High Electron Mobility. *Applied Physics Letters* **2008**, *92* (14), 143303. https://doi.org/10.1063/1.2903486.

(42) Wang, H.; Song, D.; Yang, J.; Yu, B.; Geng, Y.; Yan, D. High Mobility Vanadyl-Phthalocyanine Polycrystalline Films for Organic Field-Effect Transistors. *Applied Physics Letters* **2007**, *90* (25), 253510. https://doi.org/10.1063/1.2751103.

(43) Gu, W.; Hu, Y.; Zhu, Z.; Liu, N.; Zhang, J.; Wang, J. Preparing Highly Ordered Copper Phthalocyanine Thin-Film by Controlling the Thickness of the Modified Layer and Its Application in Organic Transistors. *Solid-State Electronics* **2013**, *89*, 101–104. https://doi.org/10.1016/j.sse.2013.07.008.

(44) Shao, X.; Wang, S.; Li, X.; Su, Z.; Chen, Y.; Xiao, Y. Single Component P-, Ambipolar and n-Type OTFTs Based on Fluorinated Copper Phthalocyanines. *Dyes and Pigments* **2016**, *132*, 378–386. https://doi.org/10.1016/j.dyepig.2016.05.020.

(45) Nénon, S.; Kanehira, D.; Yoshimoto, N.; Fages, F.; Videlot-Ackermann, C. Shelf-Life Time Test of p- and n-Channel Organic Thin Film Transistors Using Copper Phthalocyanines. *Thin Solid Films* **2010**, *518* (19), 5593–5598. https://doi.org/10.1016/j.tsf.2010.04.035.

(46) Hong, F.; Guo, X.; Zhang, H.; Wei, B.; Zhang, J.; Wang, J. Preparation of Highly Oriented Copper Phthalocyanine Film by Molecular Templating Effects for Organic Field-Effect Transistor. *Organic electronics* **2009**, *10* (6), 1097–1101.

(47) King, B.; Radford, C. L.; Vebber, M. C.; Ronnasi, B.; Lessard, B. H. Not Just Surface Energy: The Role of Bis(Pentafluorophenoxy) Silicon Phthalocyanine Axial Functionalization and Molecular Orientation on Organic Thin-Film Transistor Performance. *ACS Appl. Mater. Interfaces* **2023**, *15* (11), 14937–14947. https://doi.org/10.1021/acsami.2c22789.

(48) Yang, S. Y.; Shin, K.; Park, C. E. The Effect of Gate-Dielectric Surface Energy on Pentacene Morphology and Organic Field-Effect Transistor Characteristics. *Advanced Functional Materials* **2005**, *15* (11), 1806–1814. https://doi.org/10.1002/adfm.200400486.

(49) Umeda, T.; Kumaki, D.; Tokito, S. Surface-Energy-Dependent Field-Effect Mobilities up to 1 Cm2/V s for Polymer Thin-Film Transistor. *Journal of Applied Physics* **2009**, *105* (2), 024516. https://doi.org/10.1063/1.3072669.

(50) Kwak, S.-Y.; Choi, C. G.; Bae, B.-S. Effect of Surface Energy on Pentacene Growth and Characteristics of Organic Thin-Film Transistors. *Electrochemical and Solid-State Letters* **2009**, *12* (8), G37. https://doi.org/10.1149/1.3139526.

(51) Lim, S. C.; Kim, S. H.; Lee, J. H.; Kim, M. K.; Kim, D. J.; Zyung, T. Surface-Treatment Effects on Organic Thin-Film Transistors. *Synthetic Metals* **2005**, *148* (1), 75–79. https://doi.org/10.1016/j.synthmet.2004.08.034.
(52) Londhe, P.; Chaure, N. B.; Athawale, A. Interface Engineering of Gate Dielectrics with Multifunctional Self-Assembled Monolayers in Copper Phthalocyanine Based Organic Field-Effect Transistors. *Materials Science and Engineering: B* **2021**, *273*, 115397. https://doi.org/10.1016/j.mseb.2021.115397.
(53) Zhou, S.; Tang, Q.; Tian, H.; Zhao, X.; Tong, Y.; Barlow, S.; Marder, S. R.; Liu, Y. Direct Effect of Dielectric Surface Energy on Carrier Transport in Organic Field-Effect Transistors. *ACS applied materials & interfaces* **2018**, *10* (18), 15943–15951.
(54) Melville, O. A.; Grant, T. M.; Lochhead, K.; King, B.; Ambrose, R.; Rice, N. A.; Boileau, N. T.; Peltekoff, A. J.; Tousignant, M.; Hill, I. G.; Lessard, B. H. Contact Engineering Using Manganese, Chromium, and Bathocuproine in Group 14 Phthalocyanine Organic Thin-Film Transistors. *ACS Applied Electronic Materials* **2020**, *2* (5), 1313–1322. https://doi.org/10.1021/acsaelm.0c00104.
(55) King, B.; Melville, O. A.; Rice, N. A.; Kashani, S.; Tonnelé, C.; Raboui, H.; Swaraj, S.; Grant, T. M.; McAfee, T.; Bender, T. P.; Ade, H.; Castet, F.; Muccioli, L.; Lessard, B. H. Silicon Phthalocyanines for N-Type Organic Thin-Film Transistors: Development of Structure-Property Relationships. *ACS Applied Electronic Materials* **2021**, *3* (1), 325–336. https://doi.org/10.1021/acsaelm.0c00871.
(56) Steudel, S.; De Vusser, S.; De Jonge, S.; Janssen, D.; Verlaak, S.; Genoe, J.; Heremans, P. Influence of the Dielectric Roughness on the Performance of Pentacene Transistors. *Applied physics letters* **2004**, *85* (19), 4400-.
(57) Potocar, T.; Lorbek, S.; Nabok, D.; Shen, Q.; Tumbek, L.; Hlawacek, G.; Puschnig, P.; Ambrosch-xl, C.; Teichert, C.; Winkler, A. Initial Stages of a Para-Hexaphenyl Film Growth on Amorphous Mica. *Physical review. B, Condensed matter and materials physics* **2011**, *83* (7).
(58) Mattox, D. M. Chapter 6 - Vacuum Evaporation and Vacuum Deposition. In *Handbook of Physical Vapor Deposition (PVD) Processing (Second Edition)*; Mattox, D. M., Ed.; William Andrew Publishing: Boston, 2010; pp 195–235. https://doi.org/10.1016/B978-0-8155-2037-5.00006-X.
(59) Qian, C.; Sun, J.; Zhang, L.; Xie, H.; Huang, H.; Yang, J.; Gao, Y. Air-Stable and High-Performance Organic Field-Effect Transistors Based on Ordered, Large-Domain Phthalocyanine Copper Thin Film. *Synthetic metals* **2015**, *210*, 336–341. https://doi.org/10.1016/j.synthmet.2015.10.023.
(60) Ma Feng; Wang Shi-Rong; Li Xiang-Gao. Improved Performance of Fluorinated Copper Phthalocyanine Thin Film Transistors Using Para-Hexaphenyl as the Inducing Layer. *Chinese Physics Letters* **2011**, *28* (11), 118501. https://doi.org/10.1088/0256-307X/28/11/118501.
(61) Boileau, N. T.; Melville, O. A.; Mirka, B.; Cranston, R.; Lessard, B. H. P and N Type Copper Phthalocyanines as Effective Semiconductors in Organic Thin-Film Transistor Based DNA Biosensors at Elevated Temperatures. *RSC Advances* **2019**, *9* (4), 2133–2142. https://doi.org/10.1039/c8ra08829b.
(62) Chen, H.; Zhang, W.; Li, M.; He, G.; Guo, X. Interface Engineering in Organic Field-Effect Transistors: Principles, Applications, and Perspectives. *Chem. Rev.* **2020**, *120* (5), 2879–2949. https://doi.org/10.1021/acs.chemrev.9b00532.

(63) Kozbial, A.; Li, Z.; Conaway, C.; McGinley, R.; Dhingra, S.; Vahdat, V.; Zhou, F.; D'Urso, B.; Liu, H.; Li, L. Study on the Surface Energy of Graphene by Contact Angle Measurements. *Langmuir* **2014**, *30* (28), 8598–8606. https://doi.org/10.1021/la5018328.

(64) Cranston, R. R.; Vebber, M. C.; Faleiro Berbigier, J.; Brusso, J.; Kelly, T. L.; Lessard, B. H. High Performance Solution Processed N-Type OTFTs through Surface Engineered F–F Interactions Using Asymmetric Silicon Phthalocyanines. *Advanced Electronic Materials* **2022**, *8* (12). https://doi.org/10.1002/aelm.202200696.

(65) Rand, B. P.; Cheyns, D.; Vasseur, K.; Giebink, N. C.; Mothy, S.; Yi, Y.; Coropceanu, V.; Beljonne, D.; Cornil, J.; Brédas, J.-L.; Genoe, J. The Impact of Molecular Orientation on the Photovoltaic Properties of a Phthalocyanine/Fullerene Heterojunction. *Advanced functional materials* **2012**, *22* (14), 2987–2995.

(66) Steele, J. A.; Solano, E.; Hardy, D.; Dayton, D.; Ladd, D.; White, K.; Chen, P.; Hou, J.; Huang, H.; Saha, R. A.; Wang, L.; Gao, F.; Hofkens, J.; Roeffaers, M. B. J.; Chernyshov, D.; Toney, M. F. How to GIWAXS: Grazing Incidence Wide Angle X-Ray Scattering Applied to Metal Halide Perovskite Thin Films. *Advanced Energy Materials* **2023**, *13* (27), 2300760. https://doi.org/10.1002/aenm.202300760.

(67) Zheng Sonia Lin, B. H. L.; Brusso, J. One-Step Synthesis of Perfluorinated Polyphenylenes Using Modified Ullmann Coupling Conditions. *Synthetic Communications* **2023**, *53* (20), 1730–1738. https://doi.org/10.1080/00397911.2023.2246084.

(68) Owens, D. K.; Wendt, R. C. Estimation of the Surface Free Energy of Polymers. *Journal of Applied Polymer Science* **1969**, *13* (8), 1741–1747. https://doi.org/10.1002/app.1969.070130815.

(69) Zhao, C.; Li, A.; Chen, X.; Ali, M. U.; Meng, H. Hysteresis Effect in Organic Thin Film Transistors Based on Naphthalene Tetracarboxylic Diimide Derivatives. *Applied Physics Letters* **2021**, *118* (19), 193302. https://doi.org/10.1063/5.0045183.

Chapter 3. Engineering the Templating Layer for Silicon Phthalocyanine Based Organic Thin Film Transistors

This chapter was accepted for publication in the journal "Advanced Functional Materials": Ewenike, R. B.; Lin, Z. S.; Cranston, R.; Lamontagne, H. R.; Shuhendler, A. J.; Kim, C.-H.; Brusso, J.; Lessard, B. H.* Engineering the Template Layer for Silicon Phthalocyanine Based Organic Thin Film Transistors.

Context

Building off the success of my first chapter, we designed other templating layers to build structure property relationships and see if we can improve the F_{10}-SiPc OTFTs performance. These template layer derivatives were used to examine the impact of varying quantity of fluorine atoms on the template layer, as well as the alteration in the structure transitioning from the usual rod-like structure to a box-like structure and a S-shaped template layer. I fabricated and characterized WEG based F_{10}-SiPc OTFTs using the same conditions for all template layers for comparison.

Contributions

I synthesised and purified F_{10}-SiPc, fabricated and characterized all OTFT devices and performed the PXRD, Raman microscopy and TGA analysis. Dr. Sonia Lin synthesised the template layers (*p*-6PF_4, *p*-6PF, BBTBP, QBBP, and DFBP) with final purification through train sublimation which was performed by me. Rosemary Cranston, Halynne Lamontagne, Bahar Ronnasi, Dr. Benoît Lessard and me carried out GIWAXS experiment at the Canadian Light Source (CLS, Saskatoon). All GIWAXS data characterization and processing was performed by me with training provided by Rosemary Cranston and Halynne Lamontagne. I wrote the manuscript and with edits and revisions from Dr. Benoit Lessard. The manuscript is being reviewed by all co-authors before submission.

Abstract

Multi-phenyl and multi-thiophene rod-like molecules are typically used for the weak epitaxial growth (WEG) of highly ordered organic semiconductor films enabling controllable microstructure properties and improved device performance. However, very few templating molecules are found in literature making it challenging to establish structure property relationships. As emerging semiconductors are integrated into organic thin film transistors (OTFTs), it is necessary to establish the impact of templating layers on semiconductor microstructure and resulting device performance. Herein, four aromatic molecules with similar structure to para-sexiphenyl (*p*-6P) were synthesized and incorporated as the template layer in bottom-gate top-contact bis (pentafluoro phenoxy) silicon phthalocyanine (F_{10}-SiPc) OTFTs. The use of fluorinated *p*-6P (*p*-6PF) yielded devices with the highest electron field-effect mobility (μ_e) of 0.14 cm^2/Vs while using a partially fluorinated *p*-6P derivative (*p*-6PF_4) resulted in improved threshold voltage (V_T). X-ray diffraction (XRD) demonstrated varying F_{10}-SiPc crystallinity as a function of templating layer with the most crystalline films resulting from the use of *p*-6PF. By GIWAXS and polarized Raman microscopy all templating layers yielded films with F_{10}-SiPc molecules predominantly aligned face-on to the substrate. However, rod-like *p*-6P derivatives led to F_{10}-SiPc molecules with increased face-on orientation to the substrate. This study highlights the importance of template layer selection and deposition optimization in the fabrication of WEG based OTFTs.

3.1 Introduction

Organic thin film transistors (OTFTs) have gained significant interest in recent years due to the potential for integration in applications, ranging from smart packaging to sensors.[1,2] This growth is facilitated by the synthesis of novel organic compounds that can be seamlessly incorporated into the fabrication of electronic devices on a laboratory scale without the need to redesign equipment and procedures to accommodate these new materials.[3,4] OTFTs enable the use of a wide range of newly synthesized or existing organic compounds to serve as the dielectric layer, semiconducting layer, interlayers, or as a functional layer within the device.[5–8]

Metal phthalocyanines (MPcs) are conjugated macrocycle molecules which chelate a central metallic or metalloid atom. MPcs are commercially available, with relative ease of synthesis and are typically used as industrial dyes and pigments.[9] The exceptional thermal, mechanical, and chemical stability of MPcs has extended their application to the fabrication of highly ordered thin films for use in organic photovoltaics (OPVs), organic photoreceptors, and OTFTs.[10–12] MPcs have been extensively utilized as the semiconducting layer in OTFTs, generally resulting in *p*-type transistors (hole transport) like copper (CuPc) and zinc phthalocyanines (ZnPc). While less common, through substitution to the peripheral and central atom position, some MPcs can be derived to function as both *n*-type transistors (electron transport) and ambipolar transistors.[13] In particular, silicon phthalocyanines (R_2-SiPcs) have shown great potential as *n*-type organic semiconductors for OTFTs.[14] The tetravalent central silicon atom enables dual axial substitutions to the MPc, a feature that cannot be attained with a divalent or trivalent central atom. This substitution has resulted in a wide variety of R_2-SiPcs that can undergo thermal processing, solution processing, or both.[15] These R_2-SiPcs have demonstrated the capability to produce both *n*-type and ambipolar devices.[16] Notably, the physical vapour deposition (PVD) of bis (pentafluoro phenoxy) SiPc (F_{10}-SiPc) on an octyl-(trichloro) silane (OTS) treated silicon dioxide dielectric surface has achieved high electron field-effect mobility (μ_e) ranging from 0.1-0.5 cm²/Vs.[3,17]

Engineering the semiconductor/dielectric interface using self-assembled monolayers (SAMs) is a common strategy used to enhance the performance of OTFTs.[18–22] Modifying the dielectric surface can be used to control the crystallinity, molecular orientation, packing motif, and growth of the semiconductor resulting in a highly ordered thin film with improved charge carrier mobility (μ).[23–25] Although research has primarily focused on increasing μ, dielectric surface modification can also be used to reduce the threshold voltage (V_T) of OTFTs.[26,27] Beyond impacting the electrical characteristics of the device, modifying the dielectric surface can reduce surface defects lowering the roughness of the dielectric layer prior to semiconductor deposition.

Similar to the use of SAMs, templating layers comprised of an ultra-thin layer of a rod-like molecule can be used to modify the dielectric surface and promote weak epitaxial growth (WEG) of disk-like semiconductor molecules. WEG typically involves the thermal

deposition of a monolayer or bilayer of these rod-like molecules on the dielectric layer prior to the deposition of the organic semiconductor.[28,29] These rod-like molecules are able to provide a favourable surface for semiconductor deposition as they provide stronger π-π interactions between organic molecules compared to their interaction with the inorganic substrate.[30] WEG can influence the molecular orientation of the semiconductor during deposition, leading to a more “edge-on” orientation versus “face-on” orientation, which typically leads to improved charge transport in OTFTs. WEG has already shown to be effective in producing high-performance OTFTs, particularly with MPcs such ZnPc, CuPc, perfluorinated copper phthalocyanine (F_{16}-CuPc), tin phthalocyanine (SnOPc), and vanadyl phthalocyanine (VOPc).[30,31] Changes in the deposition conditions of the template layer, in particular the substrate temperature and deposition time, have been shown to induce distinct growth morphologies and surface coverages, leading to changes in OTFT performance.[32] Similar to WEG, the use of molecular step template (MST) has been shown to effectively smooth the dielectric surface, reduce the nucleation barrier, and decrease nucleation event density. This results in an improvement to the grain size leading to highly ordered organic thin films.[33] Furthermore, MST and WEG could potentially serve as ideal platforms for enhancing organic semiconductor single crystal films, which have already exhibited high-performance OTFTs with mobilities reaching >10 cm²/Vs without the need for a template layer.[34] Using para-sexiphenyl (*p*-6P) and per-fluorinated *p*-6P (*p*-6PF) as template layers for fabricating F_{10}-SiPc OTFTs, our group has demonstrated the importance of not only optimizing the template layer deposition, but also the selection of template layer molecule. It was found that a substrate deposition temperature of 100°C and a template layer thickness of 8 nm yielded F_{10}-SiPc OTFTs with μ_e on the same order of magnitude as F_{10}-SiPc OTFTs fabricated using OTS surface modification. Additionally, grazing incidence wide-angle X-ray scattering (GIWAXS) showed that the molecular orientation of F_{10}-SiPc remains unchanged when *p*-6P and *p*-6PF are used as the template layer. However, the relative degree of crystallinity of F_{10}-SiPc is significantly enhanced when using *p*-6PF as opposed to the use of *p*-6P.[35]

In this study, we report the synthesis of four novel template compounds 2',2'''',2''''',3,3',3'''',3''''',4,4''''',5,5',5'''',5''''',6',6''''-hexadecafluoro

1,1':4',1":4",1"':4"',1"":4"",1"""-sexiphenyl (*p*-6PF$_4$), 4,4'-bis(benzo[d]thiazol-2-yl)-1,1'-biphenyl - bisbenzothiazolylbiphenyl (BBTBP), (1,1′:3′,1″:3″,1‴-quaterphenyl, 5′,5″-diphenyl-) (QPBP), and 4,4'-di(9H-fluoren-3-yl)-1,1'-biphenyl – difluorenylbiphenyl (DFBP). These molecules, along with bare SiO_2, *p*-6PF, and *p*-6P, were employed as the templating layer in bottom-gate top-contact F_{10}-SiPc OTFTs, as shown in **Figure 3.1**. These template layers resulted in differing OTFT electrical performance that was characterized by measuring the μ_e, V_T, and current on/off ratio ($I_{on/off}$). XRD was used to analyze the crystallinity of F_{10}-SiPc thin films deposited on the template layers, while polarized Raman microscopy and GIWAXS techniques were used to draw a correlation between device performance and structural properties. Herein, we demonstrate the need to optimize the selection of template layer and semiconductor pair along with the deposition conditions of the template layer for WEG based OTFTs.

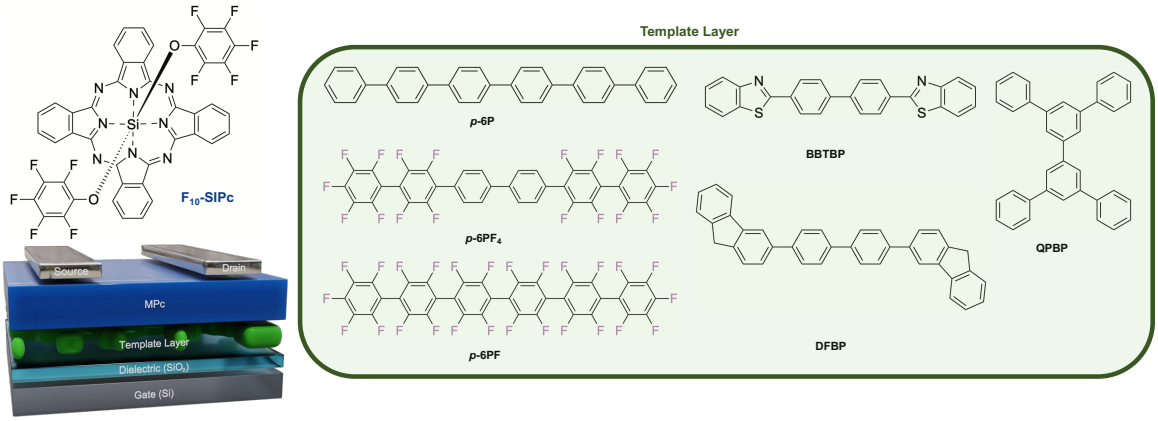

Figure 3.1. *Schematic diagram of a bottom-gated top-contact OTFT and structure of F_{10}-SiPc. Molecular structure of p-6P, p-6PF$_4$, p-6PF, BBTBP, QPBP, and DFBP template layers.*

3.2 Results and Discussion

A series of aromatic molecules with similar structures to *p*-6P were synthesized and used as templating layers to study the WEG growth of F_{10}-SiPc for integration into OTFTs. The structure and purity of each derivative after train sublimation were confirmed by nuclear magnetic resonance (NMR) and mass spectrometry (**Figure 3.5-3.11**). Further material analysis was performed by thermogravimetric analysis (TGA) of F_{10}-SiPc and the template layers presented (**Figure 3.12**). OTFTs were fabricated using six different templating layers (**Figure 3.1**) which were deposited by PVD. Electrical performance of

F_{10}-SiPc OTFTs fabricated on *p*-6PF and bare SiO_2 has been reported in literature and was included as controls for comparison.[35] The four novel materials (*p*-6PF_4, BBTBP, QPBP, and DFBP) were therefore integrated into F_{10}-SiPc based OTFTs as the templating layer. To compare the electrical properties of OTFTs using these new template materials to the previously reported *p*-6PF, the optimized deposition procedure outlined in our previous work was used.[35] Template layers were deposited by PVD onto heated substrates at 100˚C until a final thickness of 8 nm was reached as determined by a quartz crystal microbalance (QCM). Subsequently, a 50 nm thick layer of F_{10}-SiPc was deposited by PVD on all templating layers at the same time ensuring the deposition conditions used for the F_{10}-SiPc layers were identical for all devices.

The first three template layers (*p*-6P, *p*-6PF_4, *p*-6PF) were chosen to provide increasing fluorination to the linear *p*-6P derivatives in order to investigate the influence of fluorine interactions between F_{10}-SiPc and the template layer. QPBP was chosen to provide a box-like structure, serving as an isomer of *p*-6P, to investigate the influence of its structure on the electrical performance and molecular orientation of F_{10}-SiPc. These structures have been shown to improve perpendicular molecular orientation of planar semiconductors to the substrate when incorporated in OLEDs.[36] However, F_{10}-SiPc differs from traditional planar semiconductors due to its axial substitution, leading to more complex molecular packing.[14,23] Similar to the QPBP, DFBP was selected to introduce a slight deviation from the linear *p*-6PF, as the "S" conformation of this material provides a non-linear template structure which was hypothesized to induce different stacking of non-planar semiconductor molecules. Furthermore, BBTBP was employed to preserve the rod-like configuration while changing the aromatic ring structure and including atoms such as nitrogen and sulphur while maintaining a similar length to *p*-6P. These template layers were selected to investigate the impact of the structure of template on F_{10}-SiPc, whose molecular stacking differs from the typically disk-like MPcs. **Table 3.1** summarizes the electrical characterization of F_{10}-SiPc OTFTs fabricated using the different templating layers, with characteristic transfer and output curves found in **Figure 3.13-3.17**. OTFTs fabricated using *p*-6PF had the highest measured μ_e of 0.14 cm²/Vs followed by devices fabricated with DFBP which gave a μ_e of 0.032 cm²/Vs. Conversely, OTFTs fabricated

with the template materials *p*-6P and QPBP exhibited the lowest measured μ_e of 0.0012 and 0.0013 cm²/Vs, respectively.

Table 3.1. *Electrical characteristics summary of F_{10}-SiPc OTFTs measured in the saturation region with 8 nm thick template layers deposited on substrates heated to 100˚C.*

Template Layer	μ_e [a] ($cm^2/V\,s$) × 10^{-2}	$\mu_{e,max}$ [b] ($cm^2/V\,s$) × 10^{-2}	V_T [a] (V)	$I_{on/off}$ [c]	N#[a]	ref
SiO_2	1.70 ± 0.8	2.26	13.2 ± 1.9	10^4	39	[35]
p-6P	0.12 ± 0.01	0.04	12.5 ± 3.4	10^4	24	–
p-6PF_4	0.70 ± 0.1	1.10	5.52 ± 2.4	10^4	37	–
p-6PF	14.1 ± 3.1	17.7	10.4 ± 2.4	10^3	38	[35]
BBTBP	1.70 ± 0.5	2.50	7.40 ± 0.7	10^3	38	–
QPBP	0.13 ± 0.1	0.03	17.6 ± 6.0	10^3	22	–
DFBP	3.20 ± 2.0	5.60	9.20 ± 2.9	10^3	36	–

a) μ_e and V_T were calculated using an average value. b) maximum μ_e of measured from N# of functional devices out of 40 used for averages and medians c) ratio of the on and off current, $I_{on/off}$ were calculated using a median value.

These results highlight that increasing the number of fluorine atoms in linear rod-like template layers (*p*-6P, *p*-6PF_4, and *p*-6PF) leads to an increase in the μ_e of F_{10}-SiPc OTFTs. The semiconductor/dielectric interface plays a crucial role in charge transfer within an OTFT, particularly within the first few monolayers of the semiconductor where charge transport occurs. Therefore, hydrophobic surfaces are typically used to inhibit the diffusion of environmental dopants such as water and oxygen, improve charge injection, reduce the polarity in the dielectric layer, and to minimize charge traps at the interface.[37] Studies have also shown that fluorine-fluorine interactions significantly improve the formation of highly ordered crystalline films.[38,39] Cranston et al. showed that the use of trichloro(3,3,3-trifluoropropyl) silane (PTFS), a fluorine-rich SAM, for the fabrication of solution-processed (tri-*n*-hexylsilyl oxide) fluorosilicon phthalocyanine (F-3HS-SiPc) based OTFTs yielded high μ_e of 0.13 cm^2/Vs.[24] The use of PTFS significantly improved μ_e and film crystallinity in comparison to other OTFTs fabricated on bare SiO_2 and SAMs with different chain lengths, fluorinated chains, and functional groups such as

trimethoxy(phenyl) silane (MPTS) and trichloro(phenyl) silane (PTS).[24] Our results clearly demonstrate that the use of *p*-6PF provided the most fluorine-fluorine interactions with the F_{10}-SiPc leading to enhanced device performance and crystallinity when compared to the other template mentioned in this study. Another study by Ward highlights the use of fluorine-fluorine interactions between the semiconductor and SAM treated electrode as a means to induce more edge-on orientation of the semiconductor leading to an increase in device μ.[40] Therefore, exploiting fluorine-fluorine interactions between the semiconductor and template layer can significantly improve device performance and film crystallinity.

The transition in template structure from a rod-like *p*-6P to a box-structure *p*-6P (QPBP) did not significantly influence the μ_e. However, employing *p*-6P resulted in devices with lower V_T and higher $I_{on/off}$. DFBP yielded the second highest μ_e, despite lacking the fluorine atoms that enhance intermolecular F-F interactions observed in *p*-6PF suggesting that the "S"-shape structure may be promising as a template layer. Notably, *p*-6PF4 resulted in OTFTs with the lowest V_T of 5.52 V across all surfaces and the lowest subthreshold swing (SS) of 2.80 mV/decade, with the lowest number of interfacial traps (D_{it}^{max}) of 2.76 × 10^{43} cm^{-2} eV^{-1} (**Table 3.2**) compared to the devices fabricated using *p*-6P and *p*-6PF. Devices fabricated using BBTBP had the lowest characterized *SS* of 1.37 mV/decade and D_{it}^{max} of 1.36 × 10^{43} cm^{-2} eV^{-1} across all surfaces despite not having the lowest V_T. In OTFTs V_T shifts are influenced by several factors, including environmental factors such as ambient oxygen and moisture, as well as limitations in charge injection at the contact electrodes.[20] However for this work, shifts in V_T due to environmental effects or source-drain contacts are unlikely as all devices were characterized under identical inert conditions and fabricated using electrodes of the same dimensions and material. Aghamohammadi et al. demonstrated that using fluoroalkyl and alkyl SAMs for the fabrication of dinaphtho[2,3-b:2′,3′-f]thieno[3,2-b]thiophene (DNTT) OTFTs resulted in varying effects on V_T shift. Specifically, the use of fluoroalkyl SAMs, featuring electron-withdrawing groups, led to a linear relationship between gate dielectric capacitance, and V_T, whereas with alkyl SAMs, the V_T was independent of gate-dielectric capacitance, primarily determined by the dipolar character of the SAM.[26] This suggests that factors beyond the electron-withdrawing properties of the template may be at play.

Dipole-dipole interactions between the template molecules could also induce an electrostatic potential across the dielectric surface, resulting in an additional gate voltage potential that could favourably affect the V_T of *p*-6PF$_4$ compared to *p*-6PF and *p*-6P.[41]

Overall, the increase in μ seen for *p*-6PF can be attributed to the higher surface contacts resulting from fluorine-fluorine interactions, whereas the improved V_t observed with *p*-6PF$_4$ is likely the result of an induced electrostatic potential across the dielectric interface due to its dipolar character. This highlights the balancing of interactions and surface properties that must be considered when selecting an appropriate templating layer. To investigate surface morphology and its effect on the observed performance, XRD was performed on F$_{10}$-SiPc films deposited on bare SiO_2 and the six different templating layers. The XRD measurements show that all films share the same characteristic peak at 2θ = 8.5-8.9° with varying peak intensity (**Figure 3.2**). The thickness of the semiconductor was identical in all films enabling the XRD peak intensity to be used to estimate the relative crystallinity between films. Additional peak analysis was used to determine crystallite size and is presented in **Table 3.3** along with peak intensities and areas. The use of rod-like template layers enhances the crystallinity of the F$_{10}$-SiPc films compared to F$_{10}$-SiPc deposited on bare SiO_2 substrates, except for the box structure template layer QPBP. Typically, newly synthesized template layers for OTFTs possess rod-like structures resembling *p*-6P. Rod-like structures are preferred as their 2D lattice parameters and geometric channels typically result in an edge-on orientation when deposited, which is crucial for promoting formation of highly ordered edge-on organic semiconductor thin films.[30]

The box-structured template layer QPBP, which lacks a rod-like structure, yielded the least crystalline films. QPBP yielded more amorphous and less crystalline F$_{10}$-SiPc films while exhibiting similar μ_e to F$_{10}$-SiPc OTFTs fabricated on *p*-6P. F$_{10}$-SiPc films deposited on *p*-6PF showed the highest XRD peak intensity, indicative of the most crystalline thin films and correlating with OTFTs which had the highest measured μ_e. These findings are consistent with our previous report, indicating that F$_{10}$-SiPc films deposited on *p*-6PF yielded a higher relative degree of crystallinity compared to those deposited on *p*-6P. Typically an increase in film crystallinity yields an increase in μ. Similar trends have been reported by De et al. and Wang et al. who found that OTFT μ improved

as the crystallinity of tin (IV) dichloride phthalocyanine ($SnCl_2Pc$) and ZnPc increased respectively after dielectric surface modification.[31,42] However, it is important to note that improved crystallinity does not always correlate with improved device performance. An example reported by Feng et al reported that F_{16}-CuPc OTFTs fabricated with *p*-6P exhibited a lower crystallinity compared to those on bare SiO_2, despite F_{16}-CuPc/*p*-6P OTFTs yielding a higher μ_e than F_{16}-CuPc/SiO_2 OTFTs.[43]

Additionally, our group has shown for different R_2-SiPcs when the substrate temperature during deposition increased the crystallinity of the film and OTFT μ increase, however when using a temperature above 200˚C the crystallinity increases further but the μ_e decreases due to large grain boundary formation.[16,44] Other factors, such as surface roughness, can also influence charge carrier pathways as previously reported using *p*-6PF deposited on substrates at 150˚C to a thickness of 8 nm led to significantly rougher dielectric surface and ultimately a reduction in device μ_e.[35] As shown in **Table 3.1**, OTFTs made with *p*-6P yielded lower μ_e (0.0012 cm²/Vs) than OTFTs fabricated on bare SiO_2 (0.017 cm²/Vs), despite films made with *p*-6P showing significantly higher crystallinity compared to films made on bare SiO_2. The second most crystalline film of F_{10}-SiPc was obtained when using DFBP as the template layer which also resulted in the second highest μ_e. These findings further suggest that rod-like structured templates may not be optimal for non-planar semiconductors like R_2-SiPcs in the absence of additional intermolecular interactions to enhance semiconductor performance. Overall, both the template structure and intermolecular forces contribute significantly to the electrical performance of F_{10}-SiPc on these template layers.

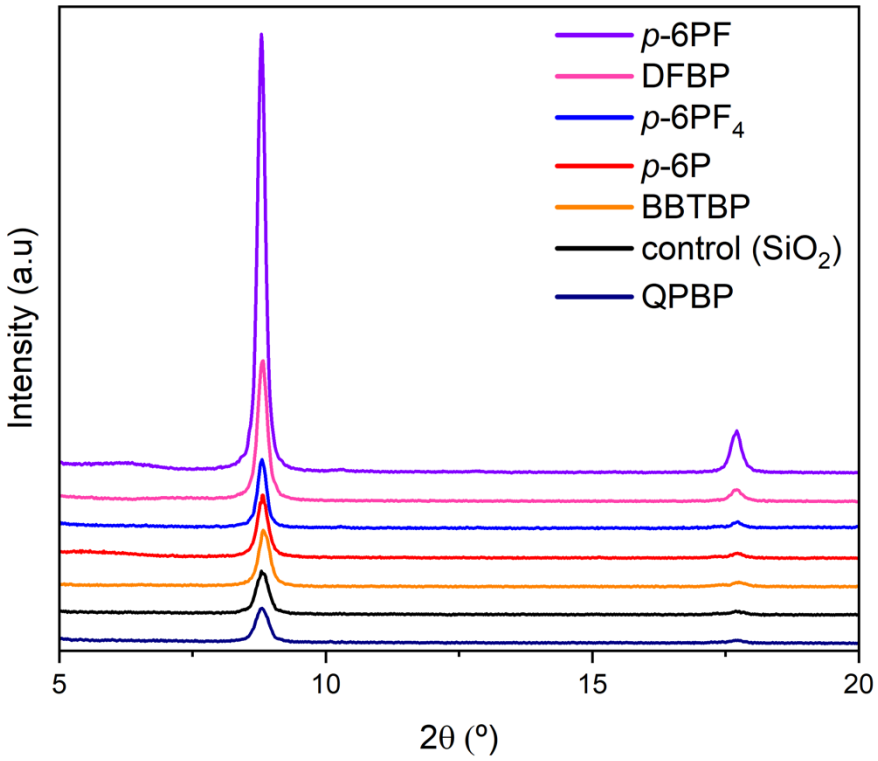

Figure 3.2. *XRD pattern of F_{10}-SiPc films deposited on bare SiO_2 and template layers used herein.*

GIWAXS was conducted on F_{10}-SiPc films deposited on SiO_2, *p*-6P, *p*-$6PF_4$, BBTBP, QPBP and DFBP to characterize the relative crystallinity and molecular orientation of F_{10}-SiPc molecules. Synchrotron radiation experiments provide higher energy and resolution for the characterization of thin films in comparison to other techniques such as XRD.[45] **Figure 3.3** shows the 2D scattering patterns of F_{10}-SiPc films deposited on bare SiO_2, *p*-6P, *p*-$6PF_4$, BBTBP, QPBP and DFBP templates. Azimuth linecuts of F_{10}-SiPc evaporated on these surfaces are in good agreement with the predicated diffraction pattern by single crystal (**Figure 3.18A**). Through GIWAXS, the molecular orientations of F_{10}-SiPc in films were determined by χ linecuts at q = 1.90 $Å^{-1}$ to characterize the π−π stacking direction parallel to the macrocycle rings of the MPc. (**Figure 3.18B**). The described linecuts show two distinct orientations at approximately 30° and 60° to the substrate (**Table 3.4**). Typically, a more edge-on orientation of the semiconductor on the substrate provides greater potential for π-π overlap and

consequently greater charge transport parallel to the substrate surface which is required for OTFT performance. Both orientations exhibit broad distributions, due to the deposition of F_{10}-SiPc on a combination surface such as the second monolayer, first monolayer of template, or bare SiO_2 due to poor template layer coverage. The orientation of F_{10}-SiPc molecules in films does not show any distinct differences with the use of template materials and shows no correlation to device performance. This suggests that regardless of the structure of the template layer it does not contribute meaningfully to changes in polymorph formation or molecular orientation relative to the substrate, but rather influences the degree of crystallinity as shown by XRD (**Figure 3.2**).

Ideal transfer characteristics are an important requirement for producing reliable and reproducible OTFTs.[46–48] The presence of significant contact and/or trap effects is usually captured as visual non-idealities such as bends or kinks in a linear-regime I_{DS}–V_{GS} curve or in a saturation-regime $I_{DS}^{1/2}$–V_{GS} curve. All our F_{10}-SiPc transistors showed nearly ideal field-effect switching evidenced by their highly linear $I_{DS}^{1/2}$–V_{GS} curves. This argument was also confirmed by the slopes approaching 2 on log-log plots between I_{DS} and (V_{GS}–V_T) (**Figure 3.19**). This ideality assessment reflects high-quality electron transport in all templated F_{10}-SiPc films, consistent with the relative crystallinity shown in **Figures 3.2 and 3.3**

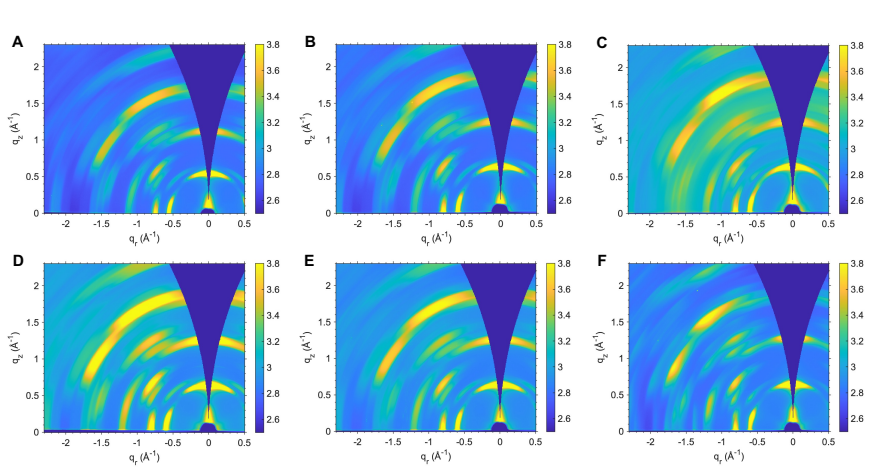

Template Layer	Primary Orientation (30°) proportion (%)	Secondary Orientation (60°) proportion 2 (%)
SiO_2	64.91	35.09
p-6P	65.52	34.48
p-6PF$_4$	66.81	33.19
BBTBP	65.87	34.13
QPBP	65.90	34.10
DFBP	65.84	34.16

Figure 3.3. *2D scattering patterns of F_{10}-SiPc deposited on (A) bare SiO_2, (B) p-6P, (C) p-6PF$_4$, (D) BBTBP, (E) QPBP, and (F) DFBP. Top-right showing the primary orientations*

of F_{10}-SiPc on corresponding surfaces determined by GIWAXS. Bottom-right shows the proportion of orientations respective to each other.

Raman microscopy is a non-destructive technique that measures the distinctive relative intensity and vibrational modes of a sample using lasers with different wavelengths. Raman microscopy has shown to be a powerful tool in investigating organic semiconductors due to the inherent delocalization of the π-electron system within conjugated molecules. This feature helps in identifying distinctive chemical bonds and molecular structures, which are dependent on the characteristics of the π-electron system.[49,50] Polarized Raman microscopy can be used to determine the local molecular orientation of organic molecules in polycrystalline films.[51,52] Polarized Raman microscopy was used to further investigate how the choice of template material influences the molecular angle of the F_{10}-SiPc with respect to the substrate. The most intense non-degenerate mode was B_{1g} pyrrole (~1535 cm^{-1}) for F_{10}-SiPc and this was used to determine the polarized integral ratios of the Z (X, X) Z' and Z (X, Y) Z' directions (**Figure 3.20**).

Polarized Raman microscopy was used to create surface maps to visualize the change in F_{10}-SiPc molecular orientation relative to the substrate using the same procedure outlined in our previous work (**Figure 3.4**).[53] **Table 3.5** summarizes the change in F_{10}-SiPc orientation when deposited on the different template layers, with all materials resulting in F_{10}-SiPc molecules aligned on average 35-38º to the substrate, similar to our GIWAXS results and previous reports using scanning transmission X-ray microscopy (STXM).[51] Unlike GIWAXS which only characterizes the orientation average in the crystalline domains, polarized Raman microscopy provides molecular orientation information for molecules in both the amorphous and crystalline domains of the films while providing information on the domain sizes. The use of rod-like template layers such as (*p*-6P, *p*-6PF_4, *p*-6PF, BBTBP, and DFBP) resulted in similar average orientations with *p*-6PF and *p*-6P resulting F_{10}-SiPc molecules aligned at the highest angle to the substrate. These findings are consistent with literature reports showing that the molecular orientation of F_{10}-SiPc remains unchanged, regardless of whether *p*-6PF or *p*-6P is used as a template layer.[35] The results also show that *p*-6P and *p*-6PF yielded boarder distributions in orientation with full width at half-maximum (FWHM) values of 2.83° and 2.68°

respectively (**Figure 3.21**). More interesting the use of the QPBP yielded a significantly lower F_{10}-SiPc angle to the substrate from the other template layers and the control SiO_2. These results show a more face-on orientation and suggest the box-structured template layer cannot induce an edge-on orientation hence the reduced device μ. For instance, the use of perylenetetracarboxylic dianhydride (PTCDA), which shares a similar box structure with QPBP, exhibits a favoured face-on orientation on inorganic substrates.[55,56] This face-on orientation is commonly used in the WEG of semiconductors, particularly in applications such as OPVs or vertical organic field-effect transistors (VOFETs), where a face-on orientation is advantageous to device performance.[57] Using BBTBP and DFBP resulted in F_{10}-SiPc molecules aligned almost identically to the control SiO_2. These three surfaces all showed similar device μ. The primary difference among these surfaces lies in the spread of FWHM (**Figure 3.21**), with DFBP resulting in the widest FWHM of 1.89°. This distribution is also reflected in device μ, where the use of DFBP led to a larger standard deviation compared to BBTBP and control SiO_2, which exhibited similar standard deviations and orientation distribution. However, it is crucial to recognize that these template layers are thermally evaporated under conditions that may not always facilitate complete monolayer formation. Consequently, the resulting film of F_{10}-SiPc will yield a varied molecular orientation due to the uneven surface coverage. These results suggest that the use of rod-like templates for OTFT fabrication yielded better edge-on orientation which improved charge transport in comparison to a box-structured template layer.

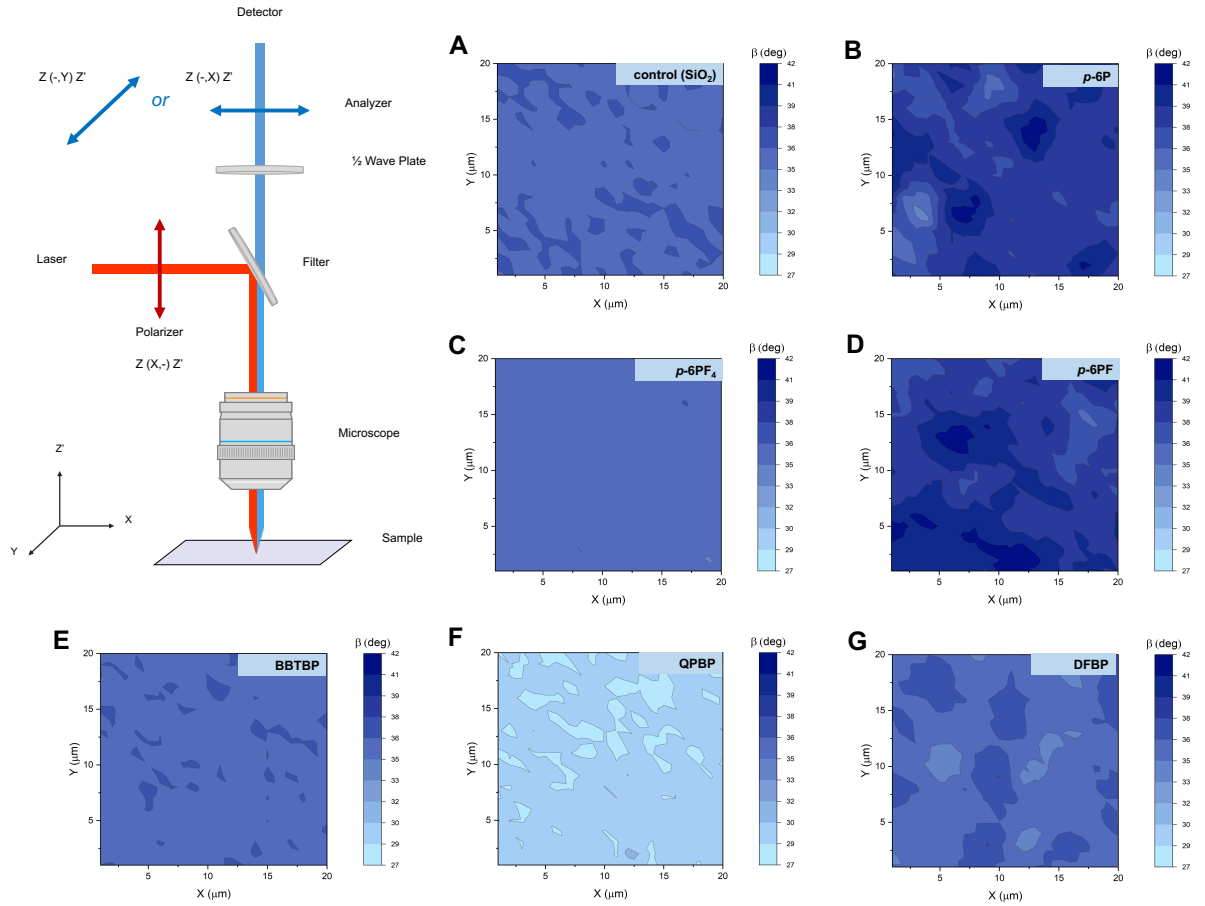

Figure 3.4. *Diagram of the polarized Raman microscope configuration and the orientation of polarization axes with respect to the sample with the corresponding Porto notation. Molecular angle maps (20 x 20 μm) between the substrate and F_{10}-SiPc deposited on (A) bare SiO_2, (B) p-6P, (C) p-6PF_4, (D) p-6PF, (E) BBTBP, (F) QPBP, and (G) DFBP.*

3.3 Conclusion

Herein, we present the synthesis of four novel small molecules (*p*-6PF_4, BBTBP, QPBP, and DFBP) which were compared to existing *p*-6P and *p*-6PF as templating layers for the formation of ordered R_2-SiPc semiconducting films in OTFTs. These molecules enabled the comparison of 1) the effect of the degree of fluorination on their ability to template the growth of the semiconductor as well as 2) their shape from linear, to "S" and to "box" or "H" shape on their ability to template the growth of the semiconductor. Increasing fluorination of the template layer resulted in higher μ devices, with the highest measured μ_e of 0.14 cm^2/Vs obtained using *p*-6PF as the template layer. The use of a partially fluorinated template layer (*p*-6PF_4) yielded OTFTs with the lowest V_T of 5.52 V.

By XRD, changes in the crystalline fraction of F_{10}-SiPc films were observed with different template layers and correlated to device performance. Through GIWAXS and polarized Raman microscopy it was determined that with all template layers, F_{10}-SiPc molecules were aligned predominantly face-on to the substrate with a wide distribution in films. PXRD and GIWAXS predominantly characterizes the crystalline domains of the films while Polarized Raman microscopy provides insight into the orientation of the molecules in both the crystalline and amorphous domains, providing complimentary insight into the different films. Molecular angle maps of F_{10}-SiPc films deposited on the different template layers revealed that the use of rod-like and the "S" structured template layers resulted in F_{10}-SiPc molecules aligned slightly more edge-on to the substrate compared to the use of a box-structured template layer. Therefore, these templating molecules are needed to yield parallel π-π bonds to the substrate, improve semiconductor growth and molecular packing to obtain high performing devices. Overall, this work shows the impact of interlayer interactions, such as halogen bonding, between the dielectric surface and the semiconductor, highlighting the importance of semiconductor/dielectric pair selection and dielectric surface treatment optimization in device performance.

3.4 Experimental Section

Materials

Para sexiphenyl (*p*-6PF, 97%) was obtained from Finetech. Bis (pentafluoro phenoxy) silicon phthalocyanine (F_{10}-SiPc) and per-fluorinated para-sexiphenyl (*p*-6PF) was synthesized according to a previously reported literature procedure.[17,55] Manganese and silver metal pellets were purchased from Angstrom Engineering.

Synthesis

All reactions were performed under a nitrogen atmosphere unless otherwise indicated and glassware was flame- or oven-dried before use. All chemicals were purchased from Millipore-Sigma or Oakwood unless otherwise indicated. The reaction pathways for all the synthetic work are shown below. Mass spectra of samples were collected at the Advanced Instrumentation for Molecular Structure (AIMS) Mass Spectrometry Laboratory at the University of Toronto. Direct Analysis in Real Time (DART) ionization was carried out on

a JEOL AccuTOF Plus 4 G JMS-T100LP-4G model time-of-flight mass spectrometer. EI analysis was performed using a JEOL AccuTOF GCx plus time-of-flight mass spectrometer. NMR experiments were performed on a Bruker Avance II 300 or 400 spectrometers (300MHz or 400 MHz for ^{1}H; 283 MHz for ^{19}F). All spectra were recorded at room temperature using deuterated chloroform as the NMR solvent. ^{19}F chemical shifts were referenced using = 0.9409401 relative to the ^{1}H resonance of trimethylsilane following the IUPAC recommendations.[59] Chemical shifts were measured in parts per million (δ scale). The coupling constants are reported in hertz. Multiplicities are reported as follows: singlet (s); doublet(d); triplet (t). All compounds were purified by train sublimation at 130-140 mTorr with CO_2 as the carrier gas.

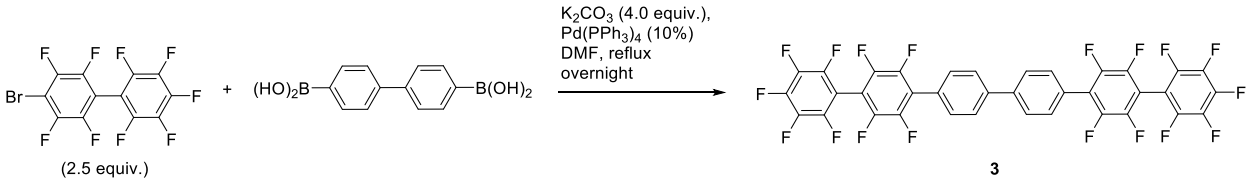

2',2'''',2'''',3,3',3'''',3'''',4,4'''',5,5',5'''',5'''',6',6''''-hexadecafluoro-1,1':4',1'':4'',1''':4''',1'''':4'''',1'''''-sexiphenyl (*p*-6PF$_4$)[55]

4-Bromo-2,2',3,3',4',5,5',6,6'-nonafluoro-1,1'-biphenyl was prepared according to literature procedure.[1]4-Bromo-2,2',3,3',4',5,5',6,6'-nonafluoro-1,1'-biphenyl (988 mg, 2.50 mmol), [1,1'-biphenyl]-4,4'-diyldiboronic acid (240 mg, 0.99 mmol), K_2CO_3 (553 mg, 4.00 mmol) and $Pd(PPh_3)_4$ (116 mg, 0.10 mmol) was charged into a 100 mL two-neck round bottom flask topped with a reflux condenser. The flask was evacuated and flashed with nitrogen three times before 30 mL of dried DMF was added. The mixture was degassed for 20 minutes. The reaction mixture was then stirred and heated at 120°C overnight. After the reaction was finished, the product was filtered and washed with H_2O (30 mL), EtOH (30 mL), MeOH (30 mL), DMF (30 mL), THF (30 mL) and CH_2Cl_2 (30 mL). This precipitate was then dried under and sublimed to give 30.5 mg of insoluble white powder. This compound is not soluble in any solvents, so no NMR data were collected. EI MS: m/z 782.03.

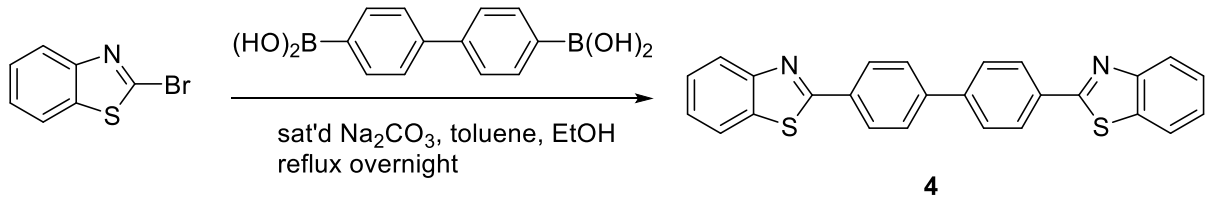

4

4,4'-bis(benzo[d]thiazol-2-yl)-1,1'-biphenyl - bisbenzothiazolylbiphenyl (BBTBP)

2-bromobenzothiazole (642.24 mg, 3.0 mmol), 4,4′-biphenyldiboronic acid (362.7 mg, 1.5 mmol), and Pd $(PPh_3)_4$ (347 mg, 0.3 mmol) were charged into a 500 mL two-necked flask. 120 mL of toluene, 30 mL of ethanol, and 30 mL of saturated Na_2CO_3 was added to the reaction flask. The reaction mixture was degassed for 20 mins and then refluxed overnight. The reaction was cooled down to room temperature, and the precipitate was filtered and washed with H_2O (50 mL), EtOH (50 mL), MeOH (50 mL), DMF (50 mL), THF (50 mL), and CH_2Cl_2 (50 mL). The grey precipitate was then dried under and sublimed to give 285.8 mg of insoluble white powder. The compound was not soluble in any solvents; hence no NMR data was collected. DART $[M+1]^+$: 421.1.

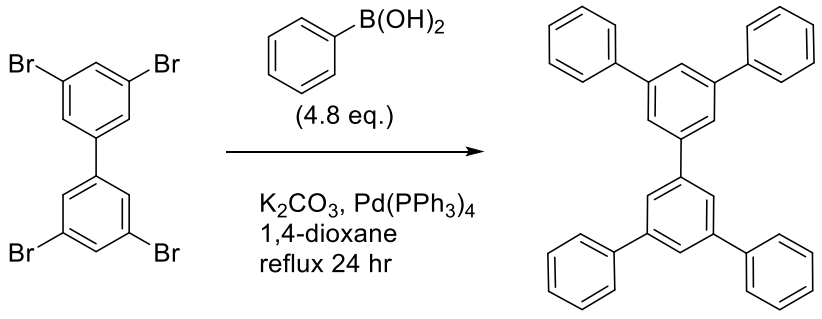

5

(1,1′:3′,1″:3″,1‴-quaterphenyl, 5′,5″-diphenyl-) (QPBP)

Phenylboronic acid (1.463 g, 12.0 mmol), 3,3′,5,5-tetrabromobiphenyl (1.16 g, 2.5 mmol), and Pd $(PPh_3)_4$ (50 mg, 0.043 mmol) were charged into a 250 mL two-necked flask. K_2CO_3 (3.0g, 21.7 mmol) in 8.7 mL of water and 40 mL of 1,4-dioxane were added to the reaction flask. The reaction mixture was degassed for 20 mins and then refluxed for 24 hrs. The reaction was cooled down to room temperature. 80 mL of water was added to the reaction mixture, and the resulting solution was extracted 3 times with 120 mL of $CHCl_3$. The combined organic layers were washed with water and dried over Na_2SO_4. The organic solvent was removed by rotary evaporation and dried under high vacuum

overnight to afford a light brown solid (2.0 g). The light brown solid was sublimed to give 198.0 mg of insoluble white powder. ^{1}H NMR was obtained for the crude material; the sublimed product was not soluble in any solvents, so no NMR data were collected.
^{1}H NMR of as-synthesized material (400 MHz, CDCl3): δ 7.87 (d, *J* = 1.4 Hz, 4H), 7.81 (t, *J* = 1.4 Hz, 2H), 7.69-7.72 (d, *J* = 7.7 Hz, 8H), 7.46-7.49 (t, *J* = 7.7 Hz, 8H), 7.37-7.40(t, *J* = 7.3 Hz, 4H), DART $[M+1]^+$: 459.2.

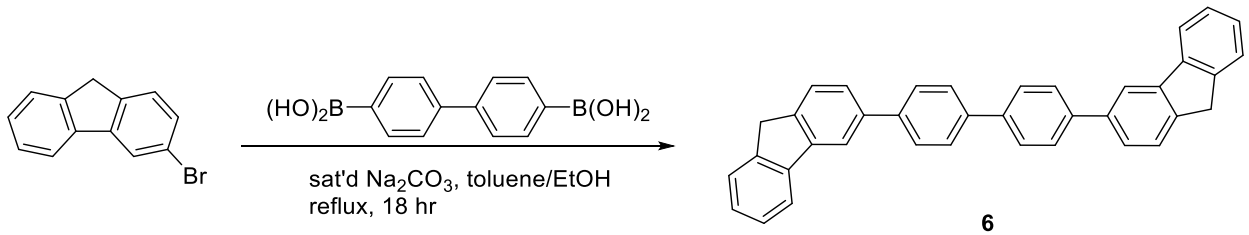

6

4,4'-di(9H-fluoren-3-yl)-1,1'-biphenyl – difluorenylbiphenyl (DFBP)

3-Bromo-9*H*-fluorene (245.1 mg, 1.0 mmol), 4,4′-Biphenyldiboronic acid (120.9 mg, 0.5 mmol), and Pd $(PPh_3)_4$ (116 mg, 0.1 mmol) were charged into a 250 mL two-necked flask. 40 mL of toluene, 10 mL of ethanol, and 10 mL of saturated Na_2CO_3 was added to the reaction flask. The reaction mixture was degassed for 20 mins and then refluxed for 18 hrs. The reaction was cooled down to room temperature, and the precipitate was filtered and washed with H_2O (20 mL), EtOH (20 mL), MeOH (20 mL), DMF (20 mL), THF (20 mL) and CH_2Cl_2 (20 mL). The grey precipitate was dried under high vacuum and sublimed to give 83.9 mg of insoluble yellow powder. The compound was not soluble in any solvents; hence no NMR data was collected. EI MS: m/z 482.2.

Synthesis of perfluorinated para-sexiphenyl (*p*-6PF)

The compound was prepared according to the published procedure.[58] ^{19}F NMR spectrum of the sublimed sample was obtained by dissolving part of the sample in refluxing $CDCl_3$.
^{19}F NMR (283 MHz, $CDCl_3$): -135.99 to -136.87 (m), -149.00 to -149.16 (t), -159.84 to -160.04 (m).

Device Fabrication

A 230 nm SiO_2 layer, which was thermally grown on N-doped silicon substrates obtained from Ossila, were cleaned by sequential rinsing with acetone and isopropanol, followed

by immediate drying using nitrogen. The dried substrates were sequentially sonicated in acetone and methanol for 5 minutes using a VWR ultrasonic cleaner (Model No: 97043-964), then dried using nitrogen before being placed in a Harrick oxygen plasma cleaner (PDC32G1 060198). The substrates were then plasma cleaned for 15 minutes under vacuum before being transferred to a dry nitrogen glove box with oxygen and moisture levels below 10 ppm. A square shadow mask with a cut designed for the silicon substrate was used for the physical vapor deposition of template layers (*p*-6PF, *p*-6P, *p*-6PF_4, BBTBP, QPBP, and DFBP), along with F_{10}-SiPc films. Template layer films were deposited using an Angstrom Engineering EvoVac evaporator. The substrate holder stage was set at a height of 50 cm, with the substrate holder heated to 100°C and soaked at this temperature for 1 hour to ensure thermal equilibrium before deposition. Each template layer was deposited at a rate of 0.05 Å/s under a base pressure ($P < 2\times10^{-6}$ Torr). The substrate holder was rotated at 10 RPM using an Oriental Motor (5IK60RGU-CU) during the deposition process. The thickness of each template layer reached 8 nm, as measured by a QCM. After the heated deposition process, the substrates were allowed to cool to room temperature overnight and were collected the following day. Each template layer underwent deposition in separate evaporations. After the template layer deposition, a 50 nm-thick layer of F_{10}-SiPc was thermally deposited at room temperature to serve as the organic semiconducting layer. This deposition occurred at a rate of 0.2 Å/s under a base pressure ($P < 2\times10^{-6}$ Torr), with the substrate holder set to rotate at 25 RPM. Before the deposition of the electrodes, a diamond-tipped pen was used to scratch the two corners along the width of the substrate to expose the Si base, allowing for the gate electrode deposition. The substrates were then placed in a source-drain mask (L = 30 μm, W = 1000 μm) obtained from Ossila. The electrodes were then thermally evaporated at a base pressure ($P < 2\times10^{-6}$ Torr) with a substrate holder rotation speed of 25 RPM. First a 10 nm-thick layer of manganese was deposited at a rate of 0.5 $Å/s^{-1}$ to serve as a contact layer for the semiconductor. Following the manganese deposition, a 50 nm-thick layer of silver was thermally deposited at a rate of 2 $Å/s^{-1}$. The shadow mask was patterned to have 20 transistors per substrate.

Device Characterization

OTFTs were transferred to and tested in a separate nitrogen filled glovebox with oxygen and moisture levels below 3 ppm. Electrical characterization was carried out using a custom-built auto tester and Keithley 2614B source meter controlled with a custom LabVIEW software for setting and sweeping voltages. Output curves were plotted by measuring the current (I_{SD}) while sweeping the source-drain voltage (V_{SD}) from 0 to 50 V and maintaining the gate voltage (V_{GS}) at a certain voltage between -10 and 50 V, stepping in intervals of 15 V. Transfer curves were generated by measuring the I_{SD} while maintaining a constant V_{SD} and sweeping the V_{GS} both forward and backward from 0 to 50 V. The sweeping of transfer curves was conducted four times to ensure device stability, using the fourth run to determine device performance parameters in the saturation regime using **Equation 3.1** shown below.

$$I_{DS} = \frac{\mu_e C_i W}{2L}(V_{GS} - V_T)^2 \qquad (3.1)$$

Where μ_e is the electron field effect mobility of the semiconductor, and L and W represent the length and width of the channel, respectively. C_i is the capacitance of the dielectric layer (SiO_2), and V_T is the threshold voltage. μ and V_T are calculated by measuring the slope and x-intercept respectively of the linearized transfer curve ($\sqrt{I_{DS}}\ vs\ V_{GS}$) using **Equation 3.2**.

$$\sqrt{I_{DS}} = \sqrt{\frac{\mu_e C_i W}{2L}}(V_{GS} - V_T) \qquad (3.2)$$

The on/off ratio of the OTFTs are calculated as the ratio of measured maximum and minimum current achieved in the operational voltage range of the transfer curves. The subthreshold swing of the OTFTs was calculated using the characteristic transfer curves of the respective template layer and the interfacial trap density was estimated by determining the maximum contribution of interfacial traps (D_{it}^{max}) using **Equation 3.3** as reported in literature.[60]

$$D_{it}^{max} = \frac{c_i}{q^2}\left(\frac{qSS}{k_B T \ln(10)} - 1\right) \qquad (3.3)$$

Where C_i is the capacitance of the dielectric layer (SiO_2), q is the electronic charge, SS is the subthreshold swing, k_B is Boltzmann's constant, and T is the temperature in Kelvin.

Thermogravimetric analysis (TGA)

TGA was performed on a Discovery TGA5500 thermal analysis system in a platinum pan with N_2 as the carrier gas at a flow rate of 25 mL min^{-1}.

X-Ray Diffraction

XRD measurements were performed on 50 nm thick F_{10}-SiPc films on an 8 nm thick template layer deposited on SiO_2 substrates. The analysis was performed using a Bruker D8 Endeavor Polycrystalline X-Ray Diffractometer equipped with a Cu Kα sealed-tube (λ = 1.5418Å) X-ray source and a LynxEye XE-T 1-D silicon strip detector. The crystallite size (D_{hkl}) estimated using the Scherrer equation shown in **Equation 3.4**.

$$D_{hkl} = \frac{K\,\lambda}{\beta\,\cos\theta_{hlk}} \qquad (3.4)$$

Where K is the Scherrer constant, λ is the wavelength of incoming x-ray, β is the full-width half-maximum of the diffraction peak and θ is the diffraction angle of incoming x-ray.

Grazing-Incidence Wide-Angle X-ray Scattering (GIWAXS)

GIWAXS experiments were performed at the Brockhouse X-ray Diffraction and Scattering Beamlines–Low Energy Wiggler (BXDS–WLE) beamline at the Canadian Light Source (CLS) with a photon energy of 9.8 keV (λ = 1.2592 Å) and in grazing-incidence (reflection) geometry. All samples were collected using a Rayonix MX300 CCD detector (73.242 μm × 73.242 μm pixel size), with an angle of incidence of θ = 0.05° and a 5 second exposure time. All samples were collected in a helium filled chamber to reduce air scattering. Silver behenate (AgBeh) and poly(3-hexylthiophene-2,5-diyl) (P3HT) standards were used to calibrate all data using the GIXSGUI software package in MATLAB.[61]

Raman Microscopy Mapping

Both non-polarized and polarized Raman spectra measurements (Z (X, X) Z' and Z (X, Y) Z') reported in this study, were acquired using a Renishaw in Via InSpec confocal Raman microscope. The microscope used was a DM2700 light source Leica Microsystems bright field microscope. A 500 mW 532 nm wavelength laser equipped with a 2400 l mm^{-1} grating was used to measure across the spectral range of 570-1700 cm^{-1}. The laser was focused on the sample through a Leica Microsystems bright field microscope with a DM2700 light source with a X50L objective with an aperture of 0.5. Using the combined objective and

laser setup described here, the Raman microscope achieves a spectral resolution of 0.3 cm^{-1} (FWHM), an estimated spatial resolution of 640 nm, and an estimated theoretical depth of focus of 3.0 μm. Prior to each measurement, calibration was done against the 520 cm^{-1} silicon reference peaks within 0.5 cm^{-1}. Unpolarized measurements were acquired using 10 % laser power (50 mW), and a 1-second exposure time (**Figure 3.22**). Each polarized Raman spectrum was collected at the same location on each film. Raman maps (20 x 20 μm) were constructed from 400 individual spectra using a 1.0 μm step size, 5 % laser power (25 mW), and a 2-second exposure time. Subsequently, each spectrum was fitted to the theoretical Lorentz curve using Wire 5.6 inVia software to obtain a map of the integral intensity (I_{XX} and I_{XY}) of the $B1_g$ pyrrole stretch Raman mode. **Equation 3.5** was employed to calculate the angle (β) of the F_{10}-SiPc molecule deposited on various template layer molecules with respect to the substrate. All collected data were processed to eliminate cosmic ray disturbances.

A degradation test was performed on the film to ensure that films did not suffer from any damage due to the extended exposure to the laser during mapping because of the repeated Raman acquisitions carried out with each change in step size. As a mapping measurement for a film will require a total of 800 scans it important to show the data collected and used to solve for the molecular angle of the F_{10}-SiPc on the substrate is not affected by any film damages. **Figure 3.23** shows no notable change in the Raman spectra of a film ran twice on the same location with the same laser conditions (5 % power with 1 second exposure time) used for mapping acquisition with an addition two runs with a laser power of 10 % and 1 second exposure time resulting in a total of 1600 scans.

$$\frac{I_{XX}}{I_{XY}} = 2\cot^2\beta \qquad (3.5)$$

Where I_{XX} is the peak intensity in the XX direction, I_{XY} is the peak intensity in the XY direction and β is the molecular angle relative to the substrate.

Acknowledgements

The authors are grateful for support from the Natural Sciences and Engineering Research Council of Canada given to B.H.L (NSERC, RGPIN-2020-04079 to B.H.L.), to R.R.C (CGSD-569930-2022 to R.R.C) and to H.L (PGS-D H.L.). We also acknowledge the support given by the University of Ottawa to B.H.L. who is a Canada Research Chair. The

Canadian Light Source (CLS) is supported by CFI, NSERC, the University of Saskatchewan, the Government of Saskatchewan, Western Economic Diversification Canada, and the Canadian Institutes of Health Research. We also thank mass spectroscopy scientist Dr. Matthew W. Forbes from AIMS mass spectrometry laboratory. The authors acknowledge technical support and training from the BXDS beamline scientist Dr. Adam Leontowich.

Supporting Information

Nuclear Magnetic Resonance Spectroscopy

Full spectrum:

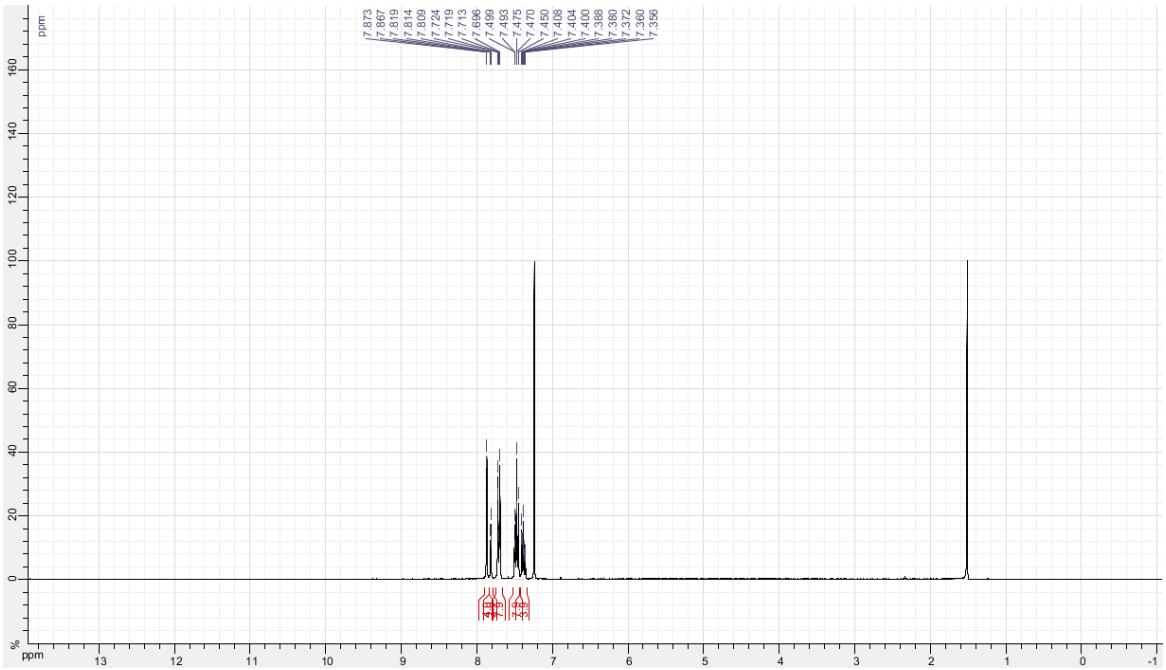

Aromatic region:

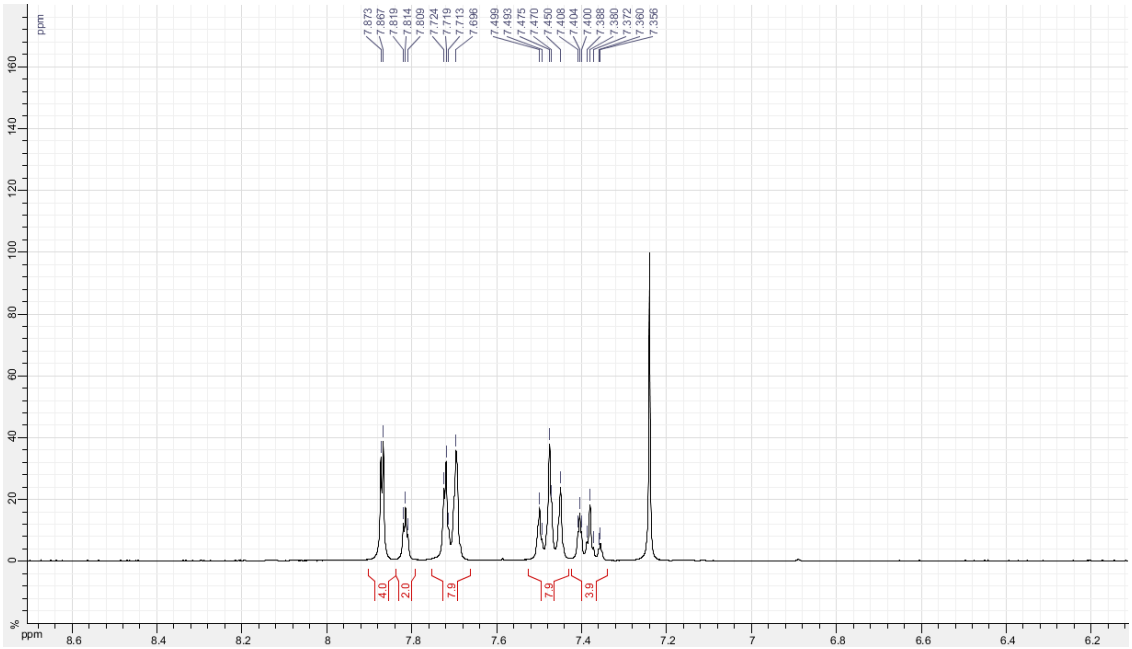

***Figure 3.5**. [1]H NMR of QPBP in $CDCl_3$.*

^{1}H NMR of *p*-6PF$_4$ ($CDCl_3$)

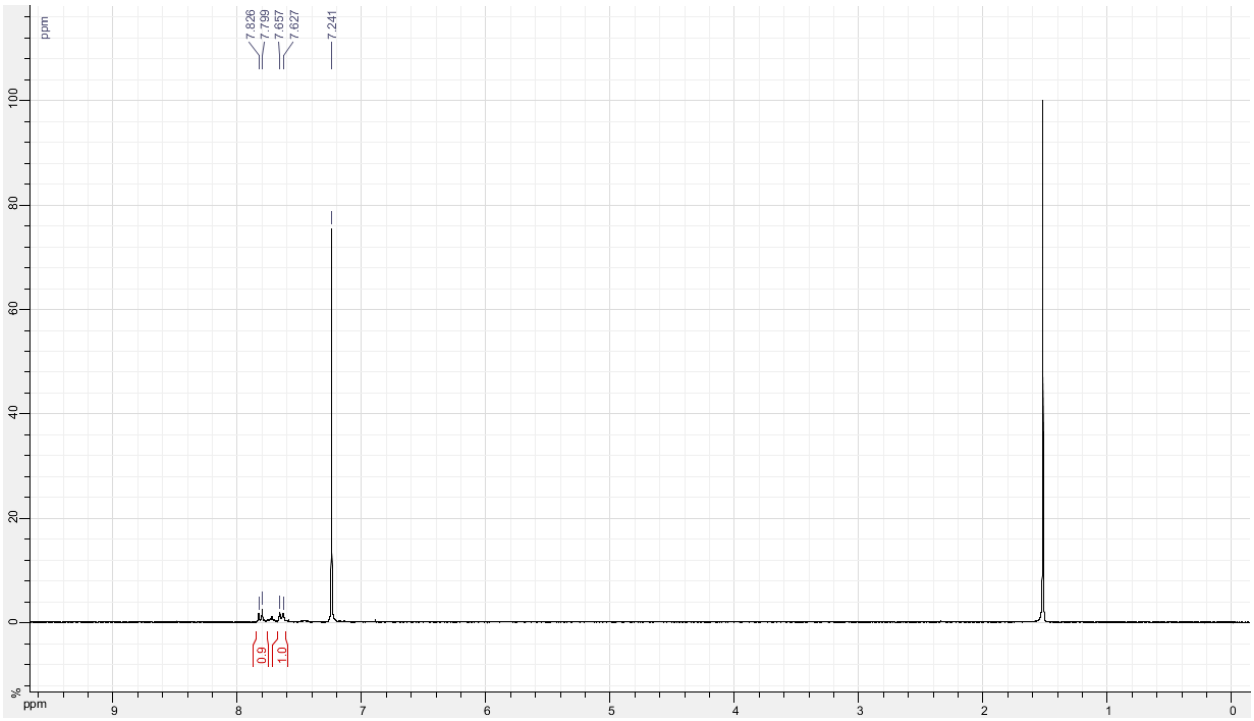

^{19}F NMR of *p*-6PF$_4$ ($CDCl_3$)

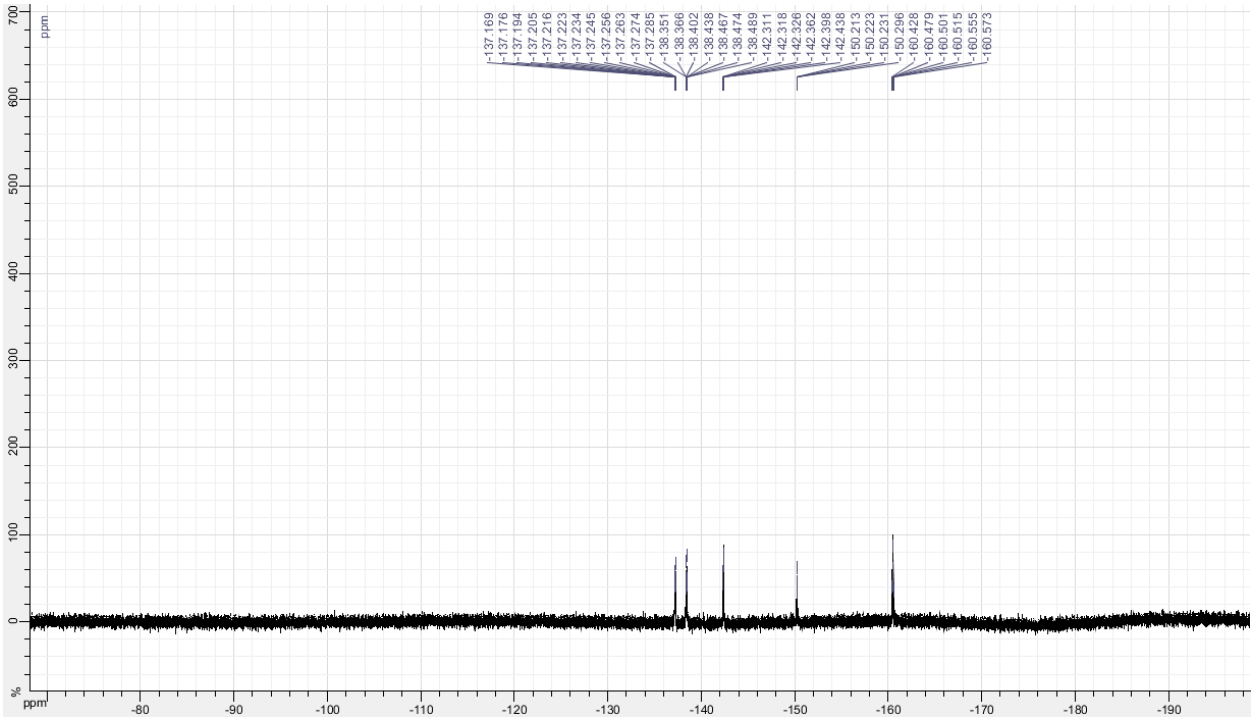

Figure 3.6. *^{1}H NMR and ^{19}F NMR of p-6PF$_4$ in $CDCl_3$.*

^{1}H NMR of *p*-6PF ($CDCl_3$)

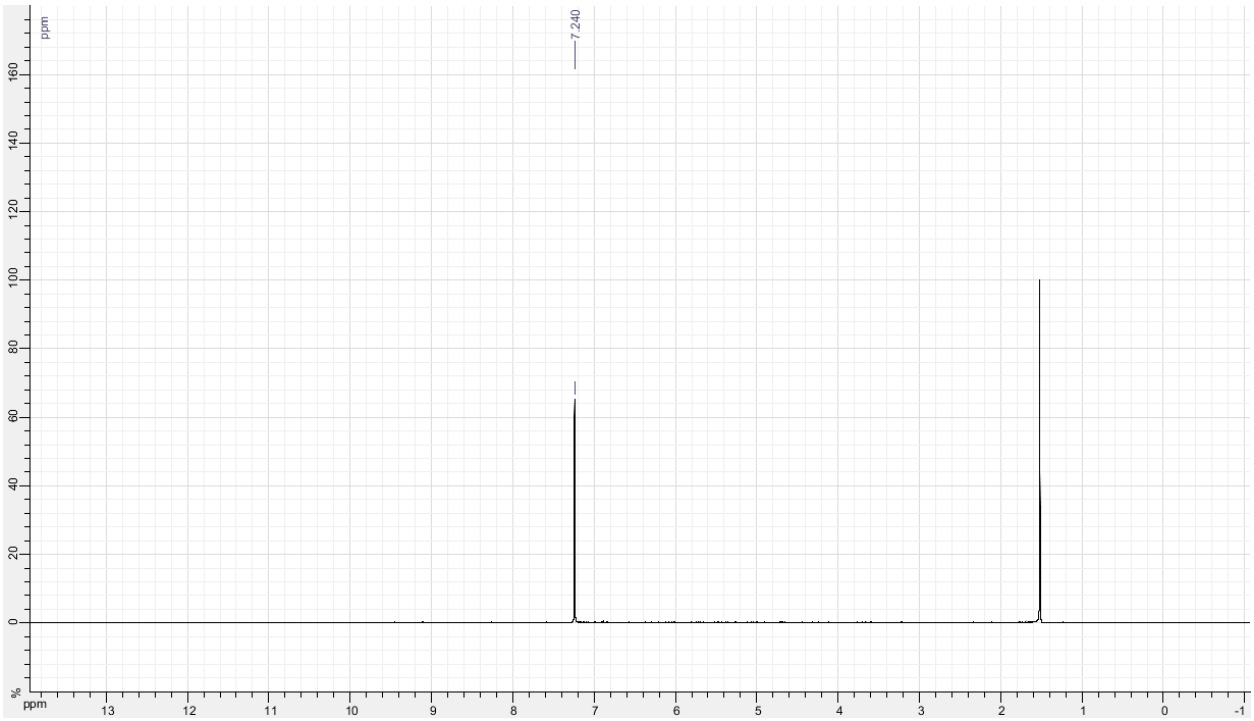

^{19}F NMR of *p*-6PF ($CDCl_3$)

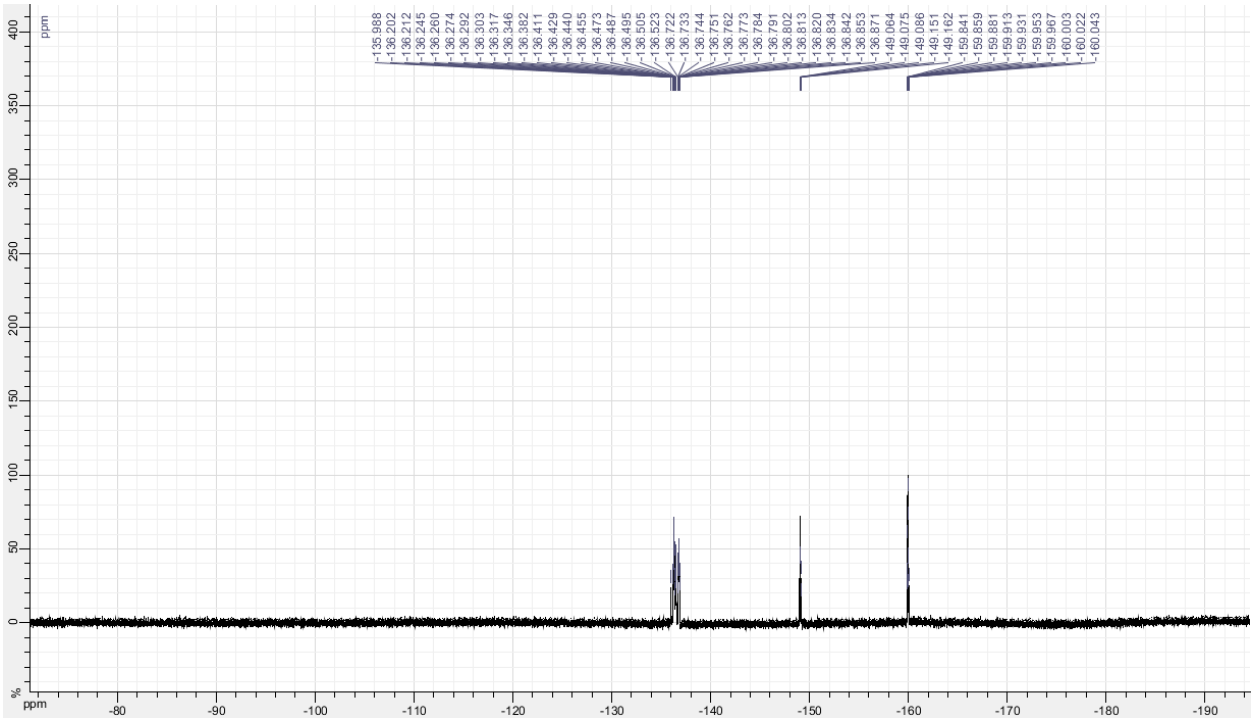

Figure 3.7. *^{1}H NMR and ^{19}F NMR of p-6PF in $CDCl_3$.*

Mass Spectrum Data

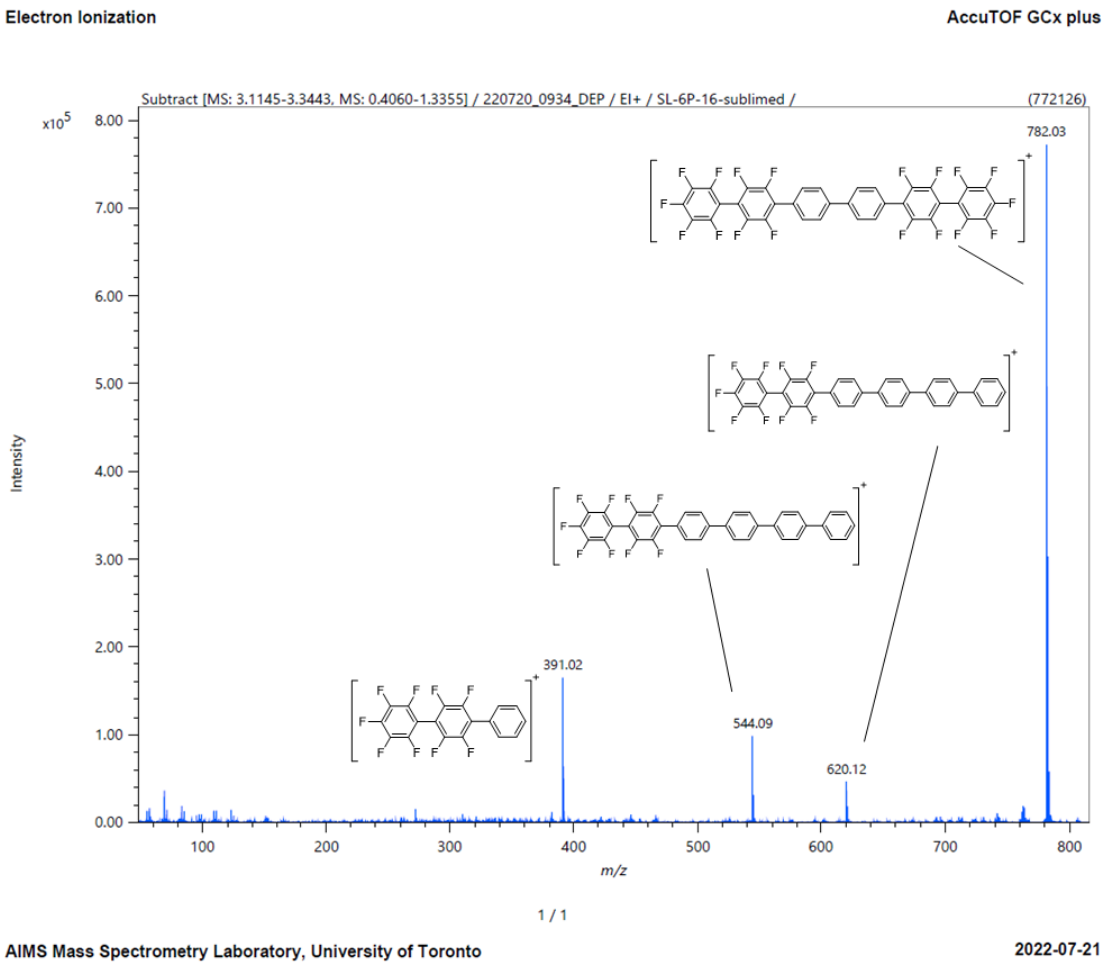

Figure 3.8. *Mass Spectrum of p-6PF$_4$.*

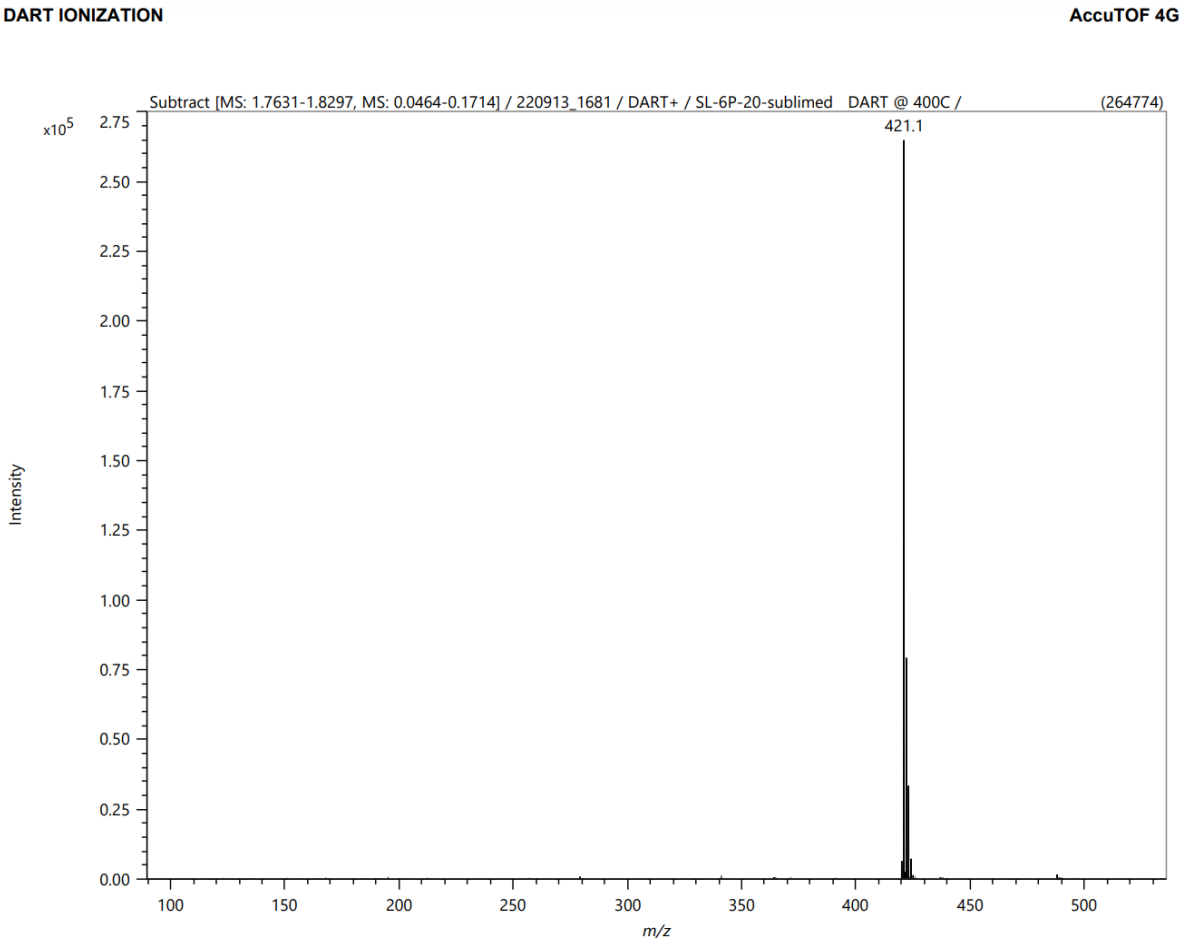

Figure 3.9. *Mass Spectrum of BBTBP.*

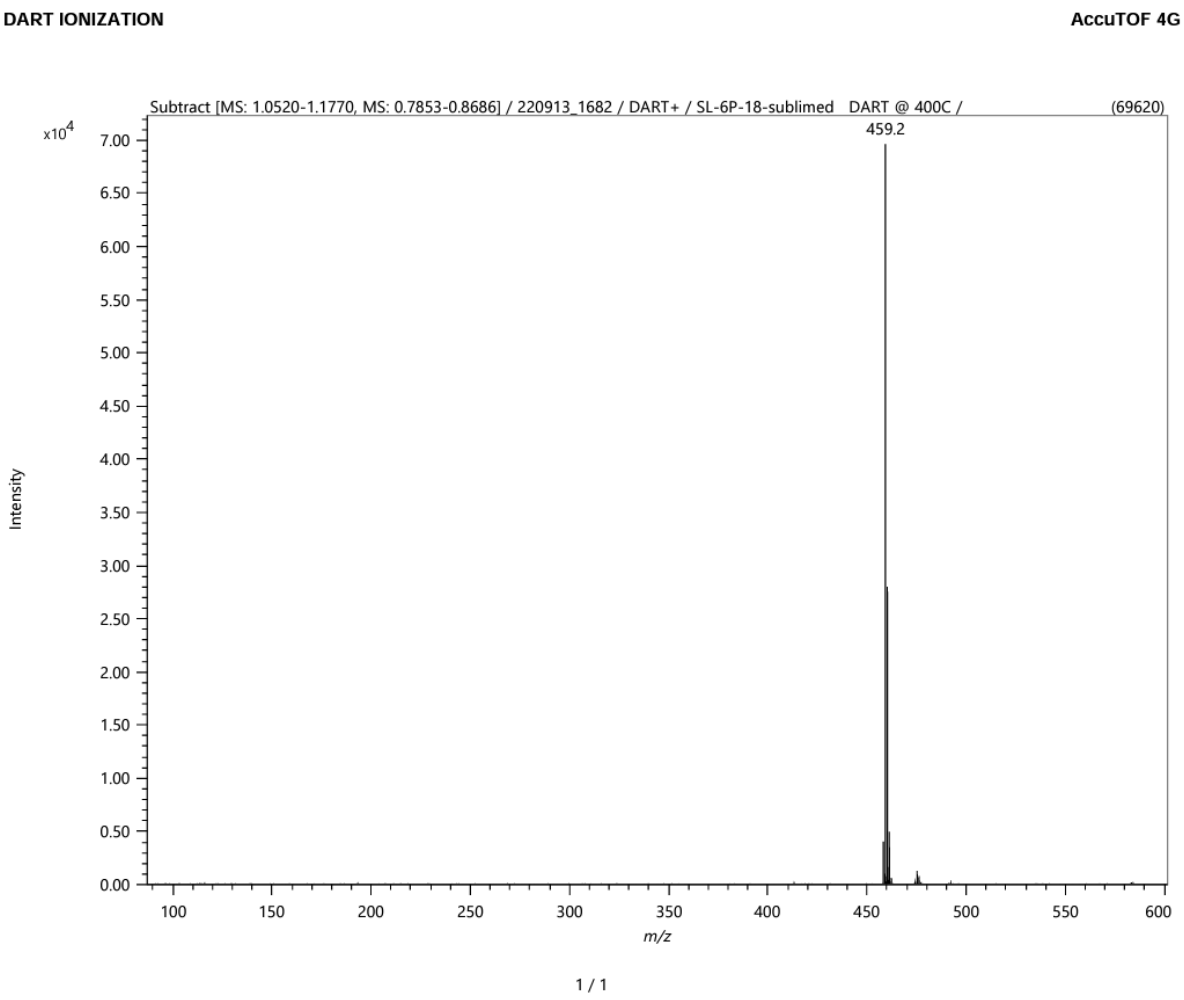

Figure 3.10. *Mass Spectrum of QPBP.*

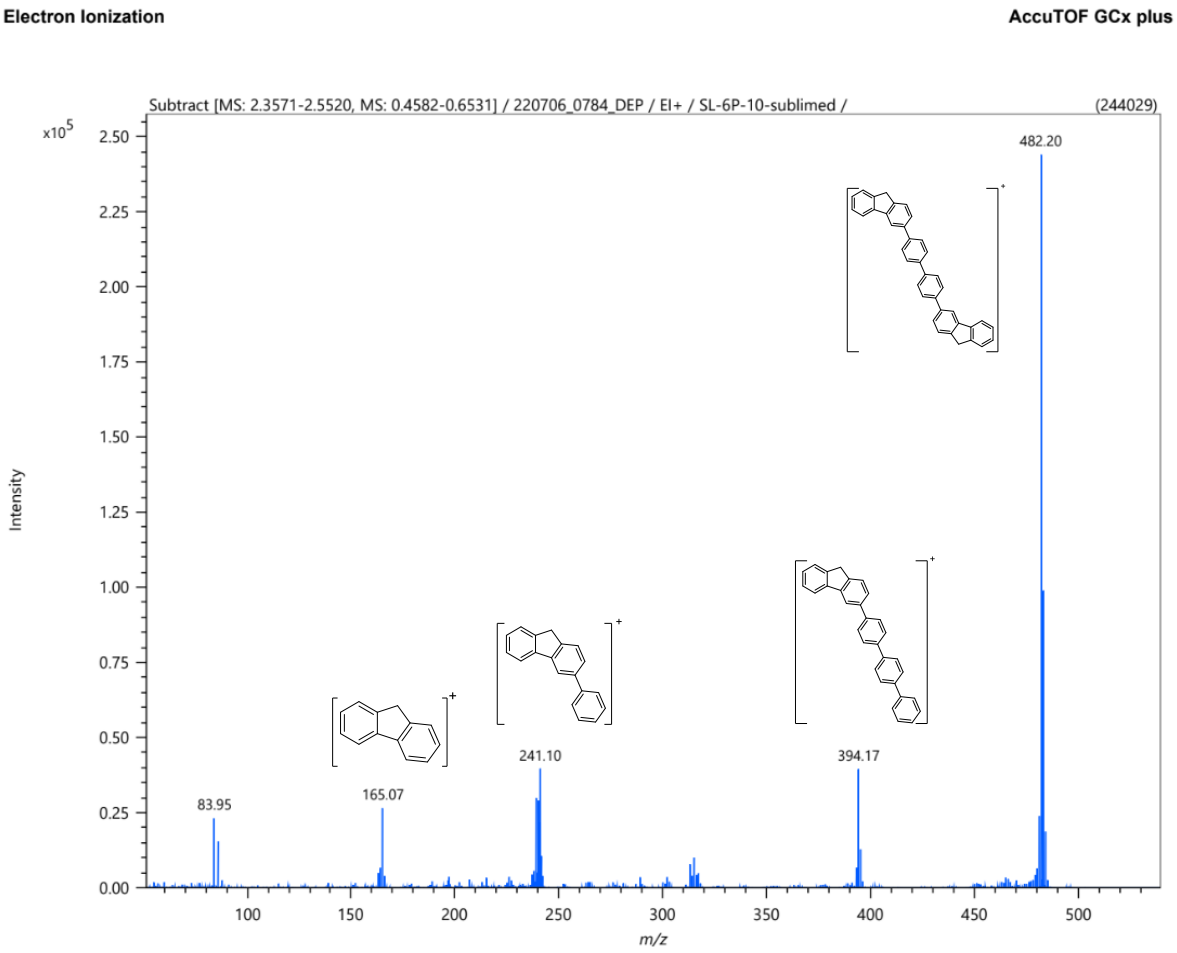

***Figure 3.11**. Mass Spectrum of DFBP.*

Thermogravimetric Analysis (TGA)

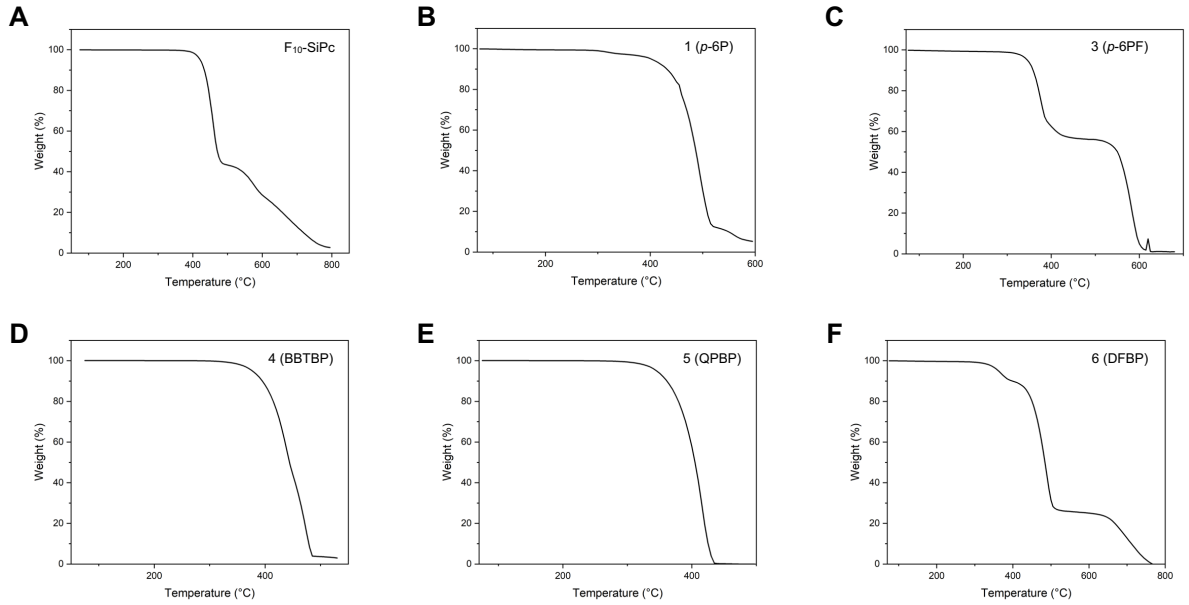

Figure 3.12. *TGA of (A) F_{10}-SiPc, (B) p-6P, (C) p-6PF, (D) BBTBP, (E) QPBP, and (F) DFBP. *TGA for p-6PF4 was not collected due to sensitive light weight powder form of compound.*

Output and Transfer Curve Data

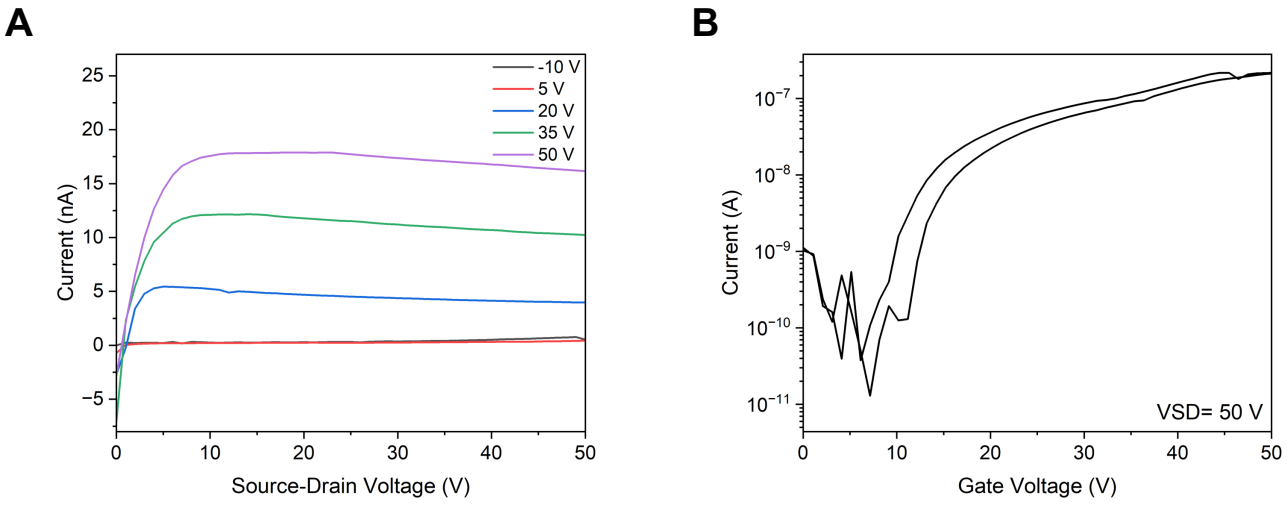

Figure 3.13. *(A) Output curve and (B) transfer curve of F_{10}-SiPc OTFTs fabricated on p-6P template layer.*

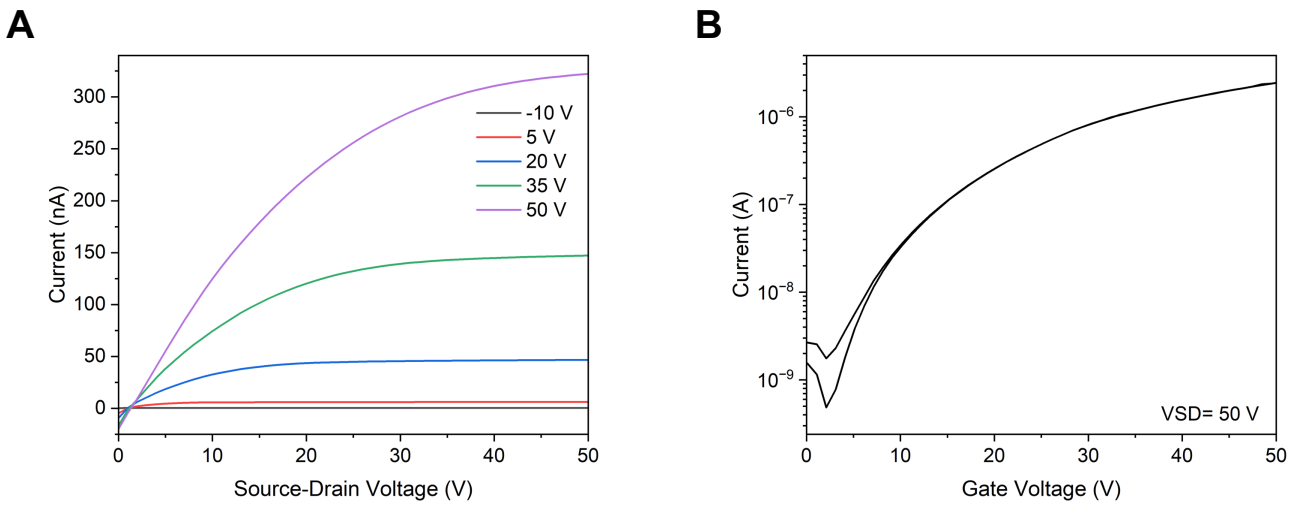

Figure 3.14. *(A) Output curve and (B) transfer curve of F_{10}-SiPc OTFTs fabricated on p-$6P_4$ template layer.*

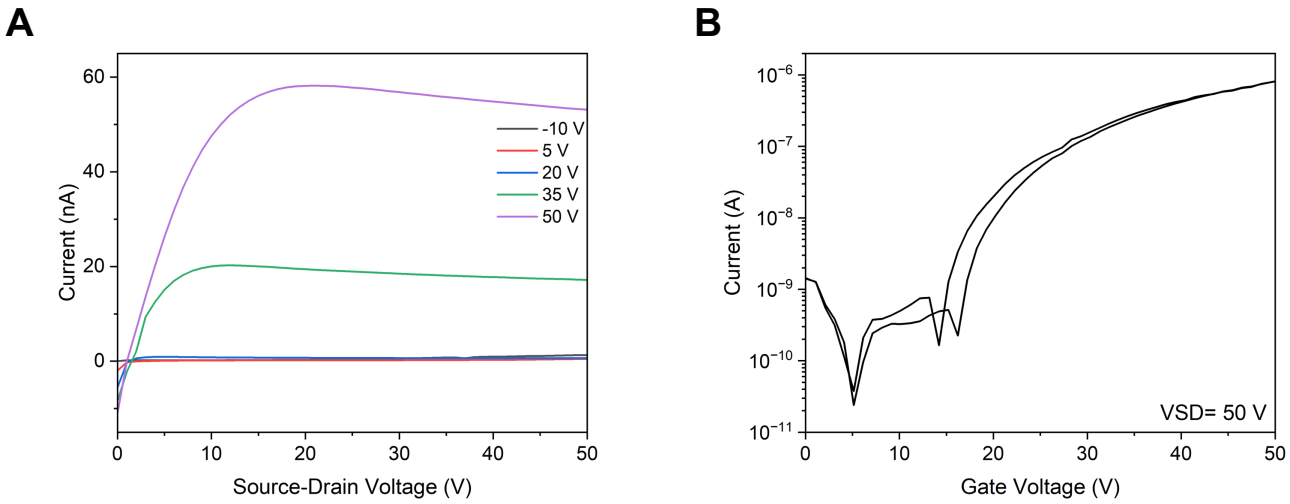

Figure 3.15. *(A) Output curve and (B) transfer curve of F_{10}-SiPc OTFTs fabricated on BBTBP template layer.*

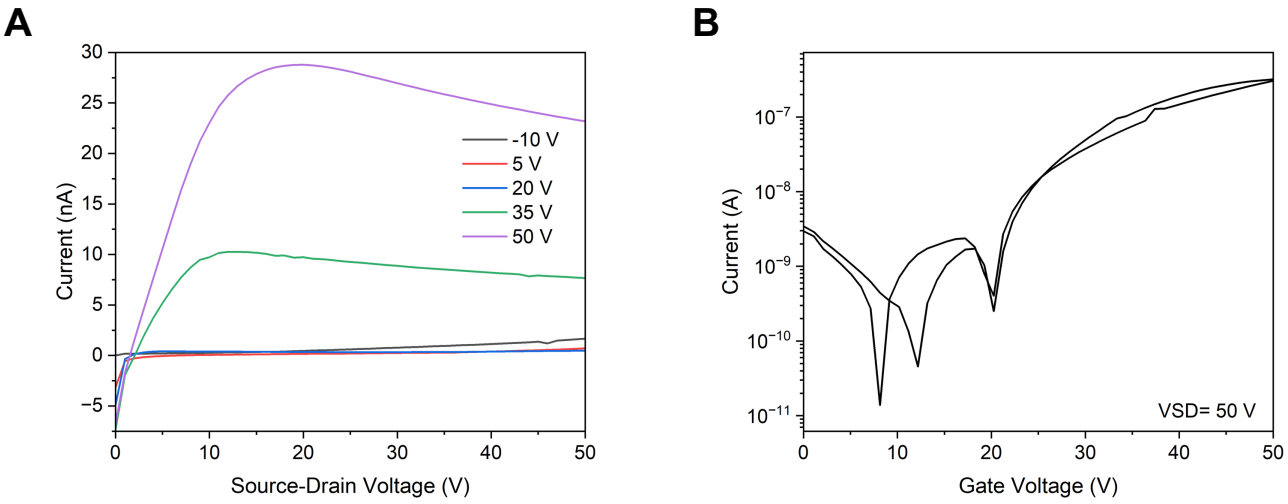

Figure 3.16. *(A) Output curve and (B) transfer curve of F_{10}-SiPc OTFTs fabricated on QPBP template layer.*

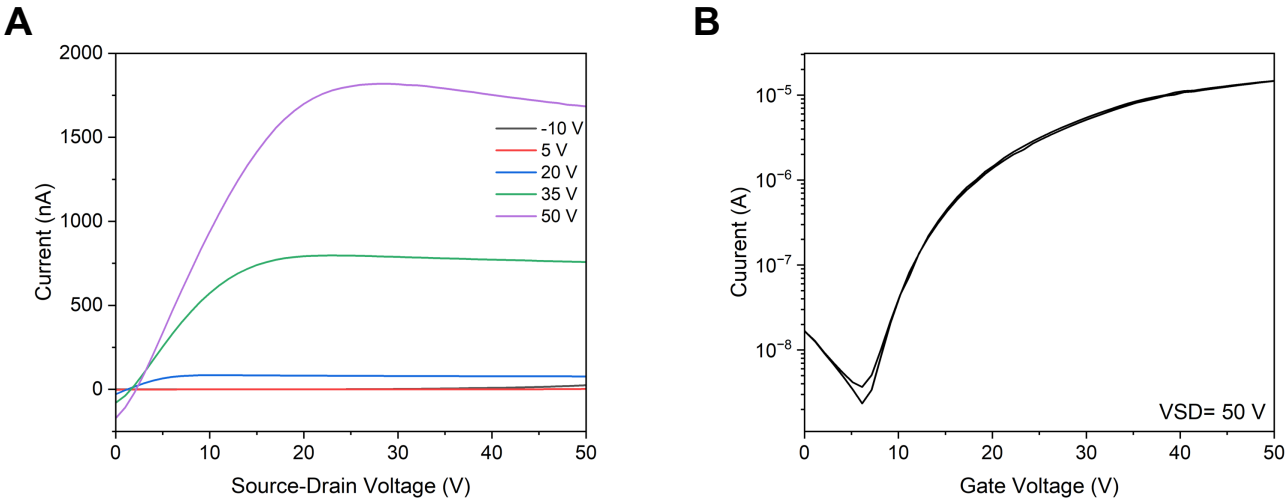

Figure 3.17. *(A) Output curve and (B) transfer curve of F_{10}-SiPc OTFTs fabricated on DFBP template layer*

Table 3.2. *Subthreshold swing and maximum contribution of interfacial traps of F_{10}-SiPc OTFTs measured using characteristics transfer curves of OTFTs.*

Template Layer	SS (mV/decade)	D_{it}^{max} (cm^{-2} eV^{-1})
SiO_2	2.48	2.45×10^{43}
p-6P	3.02	3.02×10^{43}
p-$6PF_4$	2.80	2.76×10^{43}
p-6PF	3.30	3.26×10^{43}
BBTBP	1.37	1.36×10^{43}
QPBP	2.16	2.14×10^{43}
DFBP	3.21	3.18×10^{43}

Table 3.3. *Summary of peak analysis from XRD shown in* ***Figure 3.2***

Template Layer	Peak Height	Peak Area	FWHM[a] (º)	D_{001}[b] (nm)
SiO_2	1604	444.81	0.27	29.53
p-6P	2286	574.34	0.23	34.67
p-$6PF_4$	2537	561.39	0.20	39.87
p-6PF	15537	3252.79	0.18	44.30
BBTBP	2048	562.10	0.24	33.23
QPBP	1297	391.27	0.28	28.48
DFBP	5017	1237.51	0.21	37.97

a) Full-width half-maximum (FWHM). b) Crystallite size (D_{001}) estimated using the Scherrer equation and a Scherrer constant of 0.9 .

GIWAXS Data

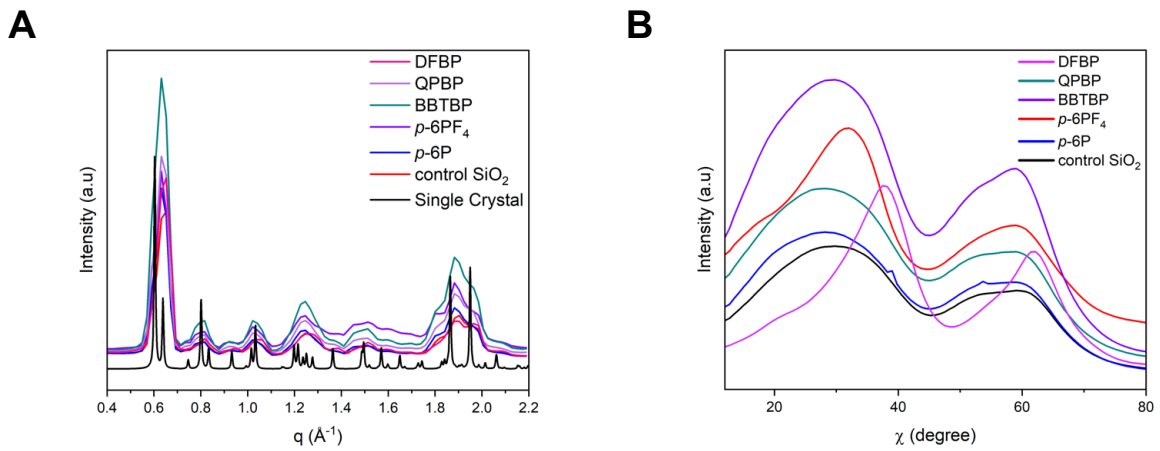

Figure 3.18. *Azimuth linecuts of (A) F_{10}-SiPc evaporated on SiO_2 and template layers p-6P, p-6PF₄, BBTBP, QPBP, and DFBP against the single crystal X-ray diffraction pattern of F_{10}-SiPc (CCDC #1034275). (B) Corresponding linecuts in the χ-direction linecuts of at q = 1.90 $Å^{-1}$ corresponding to the (132) plane.*

Table 3.4. *Peak centres and integrated area of χ linecuts at q = 1.9 $Å^{-1}$ encompassing the (132) plane of F_{10}-SiPc evaporated on SiO_2 and template layers p-6P, p-6PF₄, BBTBP, QPBP, and DFBP in* ***Figure 3.18B****.*

Template Layer	Primary Orientation (°)	Area 1	Secondary Orientation (°)	Area 2
SiO_2	29.75	45878.16	59.09	24801.95
p-6P	28.20	52672.45	53.68	27724.52
p-6PF₄	32.06	60634.63	59.09	30118.16
BBTBP	29.74	103134.83	59.09	53449.62
QPBP	28.20	64699.11	59.08	33481.78
DFBP	37.36	43947.67	62.17	22800.24

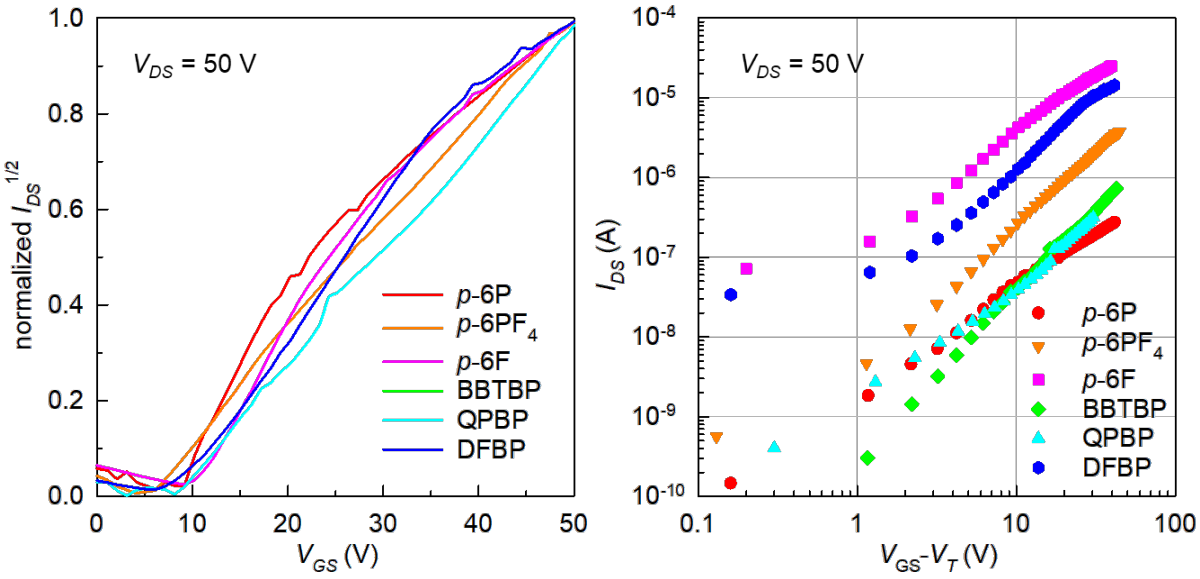

Figure 3.19. *Linearity of saturation-regime* $I_{DS}^{1/2}$–V_{GS} *curves (left) and slopes approaching 2 on saturation-regime log-log* I_{DS} *vs.* (V_{GS}–V_T) *curves (right) indicating nearly ideal field-effect switching in all templated* F_{10}*-SiPc OTFTs.*

Raman Spectra Data

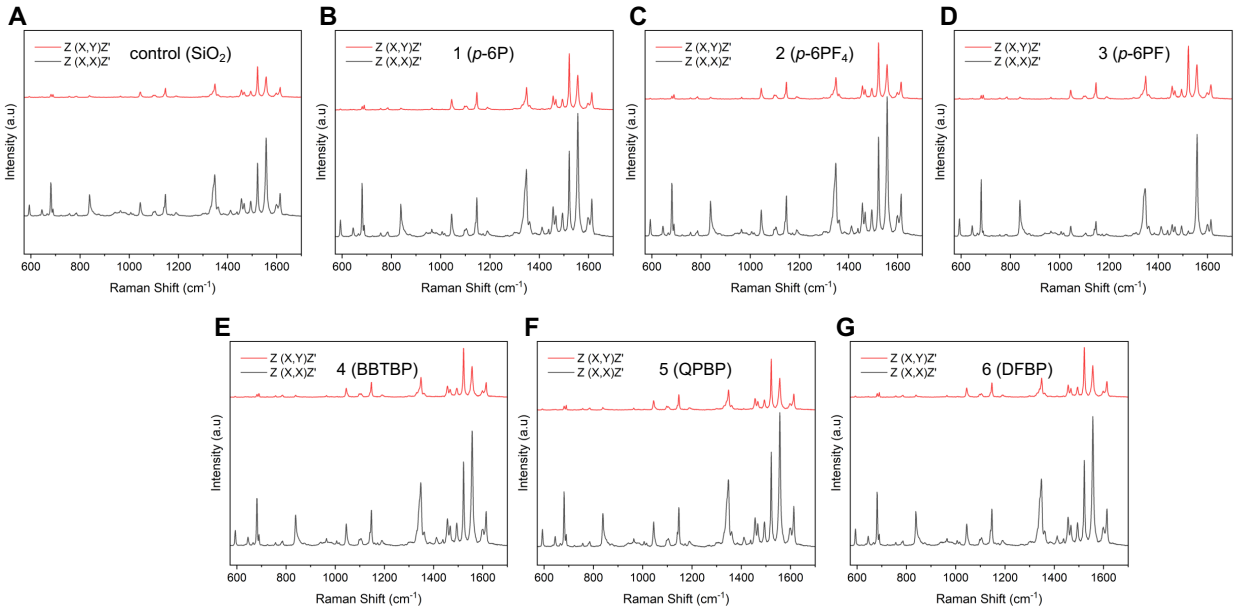

Figure 3.20. *Polarized Raman spectra of* F_{10}*-SiPc thin-films thermally evaporated on (A)* SiO_2*, (B) p-6P, (C) p-6PF4, (D) p-6PF, (E) BBTBP, (F) QPBP and (G) DFBP.*

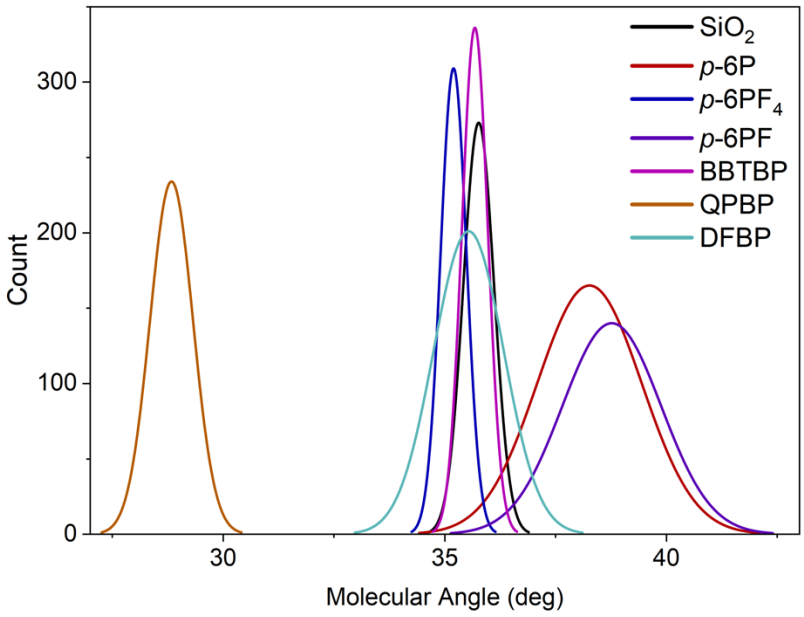

Figure 3.21. *The distribution of angles from deposition on template compounds control, p-6P, p-6PF$_4$, and p-6PF, BBTBP, QPBP, and DFBP*

Table 3.5. *Molecular angle summary of F$_{10}$-SiPc deposited on different templates layers calculated using polarized Raman microscopy.*

Template Layer	Average (deg°)	Maximum (deg°)	Minimum (deg°)	FWHM[a]
SiO_2	35.8 ± 0.3	36.8	34.9	0.83
p-6P	38.3 ± 1.2	41.2	34.1	2.83
p-6PF$_4$	35.2 ± 0.3	36.1	34.3	0.70
p-6PF	38.8 ± 1.1	41.3	35.5	2.68
BBTBP	35.7 ± 0.3	36.6	35.0	0.70
QPBP	28.8 ± 0.5	30.6	27.4	1.16
DFBP	35.5 ± 0.8	37.6	32.9	1.89

a) The FWHM was determined using the same number of counts for histograms for all surface

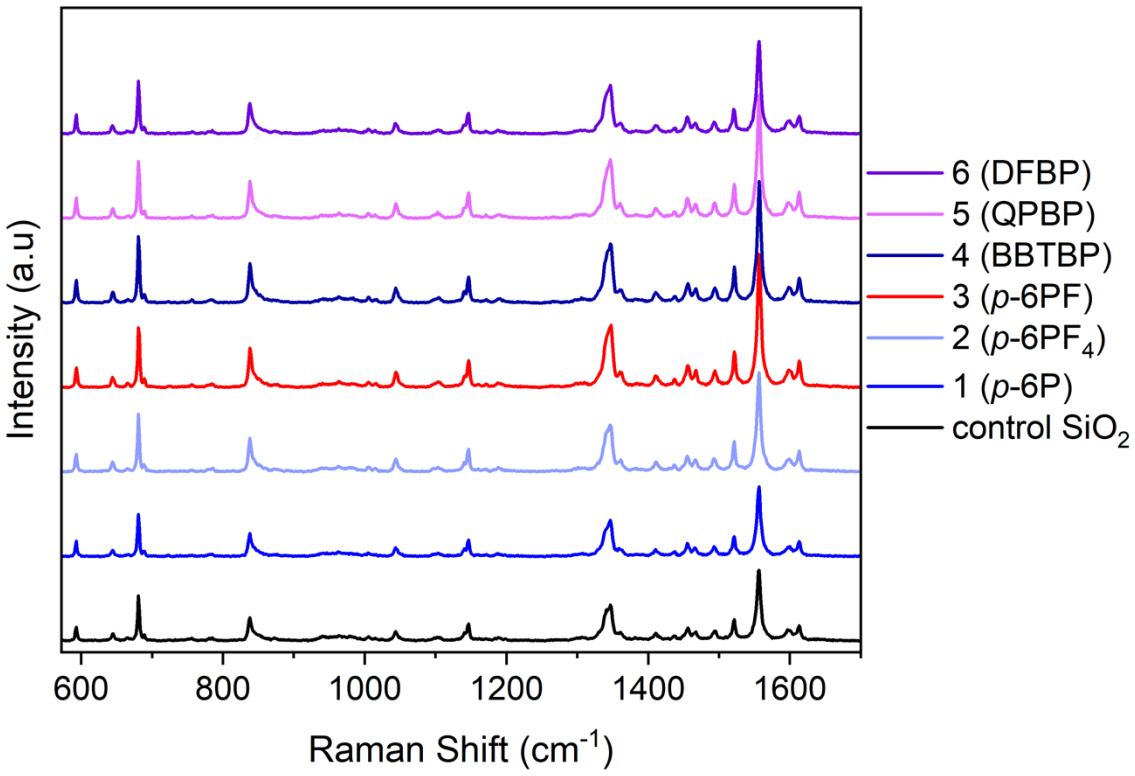

Figure 3.22. *Non-polarized Raman spectra of F_{10}-SiPc thin-films thermally evaporated on SiO_2, p-6P, p-6PF_4, p-6PF, BBTBP, QPBP, and DFBP.*

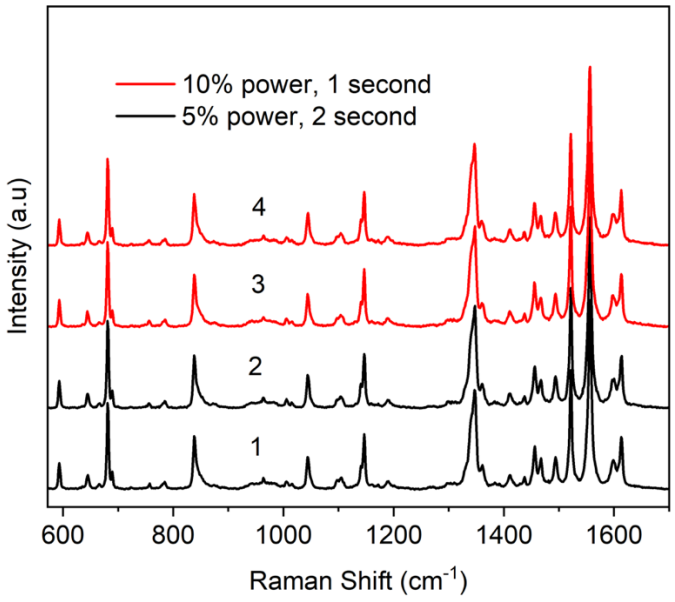

Figure 3.23. *Polarized Raman spectra (Z (X, X) Z') of F_{10}-SiPc thin-films collected sequential with different measuring conditions.*

References

(1) Lamontagne, H. R.; Comeau, Z. J.; Cranston, R. R.; Boileau, N. T.; Harris, C. S.; Shuhendler, A. J.; Lessard, B. H. Chloro Aluminum Phthalocyanine-Based Organic Thin-Film Transistors as Cannabinoid Sensors: Engineering the Thin Film Response. *Sensors & Diagnostics* **2022**, *1* (6), 1165–1175. https://doi.org/10.1039/D2SD00071G.

(2) Li, S.; Tang, W.; Chen, S.; Si, Y.; Liu, R.; Guo, X. Flexible Organic Polymer Gas Sensor and System Integration for Smart Packaging. *Advanced Sensor Research* **2023**, *2* (11), 2300030. https://doi.org/10.1002/adsr.202300030.

(3) King, B.; Vebber, M. C.; Ewenike, R.; Dupuy, M.; French, C.; Brusso, J. L.; Lessard, B. H. Peripherally Fluorinated Silicon Phthalocyanines: How Many Fluorine Groups Are Necessary for Air-Stable Electron Transport in Organic Thin-Film Transistors? *Chem. Mater.* **2023**, *35* (20). https://doi.org/10.1021/acs.chemmater.3c01342.

(4) Jeong, W.; Lee, K.; Jang, J.; Jung, I. H. Development of Benzobisoxazole-Based Novel Conjugated Polymers for Organic Thin-Film Transistors. *Polymers* **2023**, *15* (5). https://doi.org/10.3390/polym15051156.

(5) Cyr, M.; Brixi, S.; Ganguly, A.; Lessard, B. H.; Brusso, J. L. Synthesis of Thieno[3,4-c] Pyrrole-4,6-Dione-Based Small Molecules for Application in Organic Thin-Film Transistors. *Dyes and Pigments* **2023**, *210*. https://doi.org/10.1016/j.dyepig.2022.110964.

(6) Choi, J.; Kang, J.; Lee, C.; Jeong, K.; Im, S. G. Heavily Crosslinked, High-k Ultrathin Polymer Dielectrics for Flexible, Low-Power Organic Thin-Film Transistors (OTFTs).

Advanced electronic materials **2020**, *6* (8), 2000314-n/a. https://doi.org/10.1002/aelm.202000314.
(7) Guo, J.; Liu, D.; Li, W.; Yu, B.; Tian, H.; Zhu, F.; Yan, D. High-Performance 2,9-DPh-DNTT Organic Thin-Film Transistor by Weak Epitaxy Growth Method. *Organic Electronics* **2021**, *93*, 106170. https://doi.org/10.1016/j.orgel.2021.106170.
(8) Tousignant, M. N.; Rice, N. A.; Niskanen, J.; Richard, C. M.; Ritaine, D.; Adronov, A.; Lessard, B. H. High Performance Organic Electronic Devices Based on a Green Hybrid Dielectric. *Advanced Electronic Materials* **2021**, *7* (10). https://doi.org/10.1002/aelm.202100700.
(9) de la Torre, G.; Claessens, C. G.; Torres, T. Phthalocyanines: Old Dyes, New Materials. Putting Color in Nanotechnology. *Chem. Commun.* **2007**, No. 20, 2000–2015. https://doi.org/10.1039/B614234F.
(10) Bruder, I.; Schöneboom, J.; Dinnebier, R.; Ojala, A.; Schäfer, S.; Sens, R.; Erk, P.; Weis, J. What Determines the Performance of Metal Phthalocyanines (MPc, M=Zn, Cu, Ni, Fe) in Organic Heterojunction Solar Cells? A Combined Experimental and Theoretical Investigation. *Organic Electronics* **2010**, *11* (3), 377–387. https://doi.org/10.1016/j.orgel.2009.11.016.
(11) Wang, Y.; Liang, D. Solvent-Stabilized Photoconductive Metal Phthalocyanine Nanoparticles: Preparation and Application in Single-Layered Photoreceptors. *Advanced Materials* **2010**, *22* (13), 1521–1525. https://doi.org/10.1002/adma.200903120.
(12) Melville, O. A.; Lessard, B. H.; Bender, T. P. Phthalocyanine-Based Organic Thin-Film Transistors: A Review of Recent Advances. *ACS Applied Materials and Interfaces* **2015**, *7* (24), 13105–13118. https://doi.org/10.1021/acsami.5b01718.
(13) Kim, K.; Kwak, T. H.; Cho, M. Y.; Lee, J. W.; Joo, J. Comparison of Electrical Characteristics for P-Type and n-Type Organic Thin Film Transistors Using Copper Phthalocyanine. *Synthetic Metals* **2008**, *158* (13), 553–555. https://doi.org/10.1016/j.synthmet.2008.03.028.
(14) King, B.; Melville, O. A.; Rice, N. A.; Kashani, S.; Tonnelé, C.; Raboui, H.; Swaraj, S.; Grant, T. M.; McAfee, T.; Bender, T. P.; Ade, H.; Castet, F.; Muccioli, L.; Lessard, B. H. Silicon Phthalocyanines for N-Type Organic Thin-Film Transistors: Development of Structure-Property Relationships. *ACS Applied Electronic Materials* **2021**, *3* (1), 325–336. https://doi.org/10.1021/acsaelm.0c00871.
(15) Lessard, B. H. The Rise of Silicon Phthalocyanine: From Organic Photovoltaics to Organic Thin Film Transistors. *ACS Applied Materials and Interfaces* **2021**, *13* (27), 31321–31330. https://doi.org/10.1021/acsami.1c06060.
(16) Melville, O. A.; Grant, T. M.; Mirka, B.; Boileau, N. T.; Park, J.; Lessard, B. H. Ambipolarity and Air Stability of Silicon Phthalocyanine Organic Thin-Film Transistors. *Advanced Electronic Materials* **2019**, *5* (8). https://doi.org/10.1002/aelm.201900087.
(17) Melville, O. A.; Grant, T. M.; Lochhead, K.; King, B.; Ambrose, R.; Rice, N. A.; Boileau, N. T.; Peltekoff, A. J.; Tousignant, M.; Hill, I. G.; Lessard, B. H. Contact Engineering Using Manganese, Chromium, and Bathocuproine in Group 14 Phthalocyanine Organic Thin-Film Transistors. *ACS Applied Electronic Materials* **2020**, *2* (5), 1313–1322. https://doi.org/10.1021/acsaelm.0c00104.
(18) Zhao, X.; Zhang, Q.; Xia, G.; Wang, S.; Ouyang, J.; Zhou, J. Enhanced Performances of Organic Thin Film Transistors by Dual Interfacial Modification of

Dielectric Layer. *Applied Physics A* **2015**, *118* (3), 809–815. https://doi.org/10.1007/s00339-014-8802-8.

(19) Sun, Q.-J.; Zhuang, J.; Yan, Y.; Zhou, Y.; Han, S.-T.; Zhou, L.; Roy, V. A. L. Investigation on the Mobility and Stability in Organic Thin Film Transistors Consisting of Bilayer Gate Dielectrics. *physica status solidi (a)* **2016**, *213* (1), 79–84. https://doi.org/10.1002/pssa.201532380.

(20) Ronnasi, B.; King, B.; Brixi, S.; Swaraj, S.; Niskanen, J.; Lessard, B. H. Electron Donating Functional Polymer Dielectrics to Reduce the Threshold Voltage of N-Type Organic Thin-Film Transistors. *Advanced Electronic Materials* **2024**, 2300810. https://doi.org/10.1002/aelm.202300810.

(21) Xiao, K.; Liu, Y.; Guo, Y.; Yu, G.; Wan, L.; Zhu, D. Influence of Self-Assembly Monolayers on the Characteristics of Copper Phthalacyanine Thin Film Transistor. *Applied Physics A* **2005**, *80* (7), 1541–1545. https://doi.org/10.1007/s00339-003-2398-8.

(22) Liu, D.; Miao, Q. Recent Progress in Interface Engineering of Organic Thin Film Transistors with Self-Assembled Monolayers. *Mater. Chem. Front.* **2018**, *2* (1), 11–21. https://doi.org/10.1039/C7QM00279C.

(23) King, B.; Radford, C. L.; Vebber, M. C.; Ronnasi, B.; Lessard, B. H. Not Just Surface Energy: The Role of Bis(Pentafluorophenoxy) Silicon Phthalocyanine Axial Functionalization and Molecular Orientation on Organic Thin-Film Transistor Performance. *ACS Appl. Mater. Interfaces* **2023**, *15* (11), 14937–14947. https://doi.org/10.1021/acsami.2c22789.

(24) Cranston, R. R.; Vebber, M. C.; Faleiro Berbigier, J.; Brusso, J.; Kelly, T. L.; Lessard, B. H. High Performance Solution Processed N-Type OTFTs through Surface Engineered F–F Interactions Using Asymmetric Silicon Phthalocyanines. *Advanced Electronic Materials* **2022**, *8* (12). https://doi.org/10.1002/aelm.202200696.

(25) Huang, W.; Yu, J.; Yu, X.; Li, Y.; Zeng, H. Performance Enhancement of Organic Thin-Film Transistors with Improved Copper Phthalocyanine Crystallization by Inserting Ultrathin Pentacene Buffer. *Thin Solid Films* **2012**, *520* (21), 6677–6680. https://doi.org/10.1016/j.tsf.2012.06.084.

(26) Aghamohammadi, M.; Rödel, R.; Zschieschang, U.; Ocal, C.; Boschker, H.; Weitz, R. T.; Barrena, E.; Klauk, H. Threshold-Voltage Shifts in Organic Transistors Due to Self-Assembled Monolayers at the Dielectric: Evidence for Electronic Coupling and Dipolar Effects. *ACS Appl. Mater. Interfaces* **2015**, *7* (41), 22775–22785. https://doi.org/10.1021/acsami.5b02747.

(27) Pak, K.; Seong, H.; Choi, J.; Hwang, W. S.; Im, S. G. Synthesis of Ultrathin, Homogeneous Copolymer Dielectrics to Control the Threshold Voltage of Organic Thin-Film Transistors. *Advanced Functional Materials* **2016**, *26* (36), 6574–6582. https://doi.org/10.1002/adfm.201602585.

(28) Yang, J.; Yan, D. Weak Epitaxy Growth of Organic Semiconductor Thin Films. *Chem. Soc. Rev.* **2009**, *38* (9), 2634–2645. https://doi.org/10.1039/B815723P.

(29) Cranston, R. R.; Lessard, B. H. Metal Phthalocyanines: Thin-Film Formation, Microstructure, and Physical Properties. *RSC Advances* **2021**, *11* (35), 21716–21737. https://doi.org/10.1039/d1ra03853b.

(30) Yang, J.; Yan, D.; Jones, T. S. Molecular Template Growth and Its Applications in Organic Electronics and Optoelectronics. *Chem. Rev.* **2015**, *115* (11), 5570–5603. https://doi.org/10.1021/acs.chemrev.5b00142.
(31) Song, D.; Zhu, F.; Yu, B.; Huang, L.; Geng, Y.; Yan, D. Tin (IV) Phthalocyanine Oxide: An Air-Stable Semiconductor with High Electron Mobility. *Applied Physics Letters* **2008**, *92* (14), 143303. https://doi.org/10.1063/1.2903486.
(32) Yang, J.; Wang, T.; Wang, H.; Zhu, F.; Li, G.; Yan, D. Ultrathin-Film Growth of Para-Sexiphenyl (I): Submonolayer Thin-Film Growth as a Function of the Substrate Temperature. *J. Phys. Chem. B* **2008**, *112* (26), 7816–7820. https://doi.org/10.1021/jp711455u.
(33) Qiu, F.; Deng, W.; Shi, X.; Ai, D.; Ren, X.; Dong, A.; Zhang, X.; Jie, J. Large-Area Deposition of Highly Crystalline F4-Tetracyanoquinodimethane Thin Films by Molecular Step Templates. *Small Science* **2024**, *4* (7), 2400038. https://doi.org/10.1002/smsc.202400038.
(34) Sheng, F.; Deng, W.; Ren, X.; Liu, X.; Meng, X.; Shi, J.; Grigorian, S.; Jie, J.; Zhang, X. Breaking Fundamental Limitation of Flow-Induced Anisotropic Growth for Large-Scale and Fast Printing of Organic Single-Crystal Films. *Advanced Materials* **2024**, *36* (25), 2401822. https://doi.org/10.1002/adma.202401822.
(35) Ewenike, R. B.; King, B.; Battaglia, A. M.; Quezada Borja, J. D.; Lin, Z. S.; Manion, J. G.; Brusso, J. L.; Kelly, T. L.; Seferos, D. S.; Lessard, B. H. Toward Weak Epitaxial Growth of Silicon Phthalocyanines: How the Choice of the Optimal Templating Layer Differs from Traditional Phthalocyanines. *ACS Appl. Electron. Mater.* **2023**. https://doi.org/10.1021/acsaelm.3c01389.
(36) Gu-Ping, O.; Zhen, S.; You-Yu, W.; Xiao-Qiang, C.; Fu-Jia, Z. Analysis of the Injection Layer of PTCDA in OLEDs Using X-Ray Photoemission Spectroscopy and Atomic Force Microscopy. *Chinese physics (Beijing, China)* **2006**, *15* (6), 1296–1300.
(37) Kim, K.; An, T. K.; Kim, J.; Jeong, Y. J.; Jang, J.; Kim, H.; Baek, J. Y.; Kim, Y.-H.; Kim, S. H.; Park, C. E. Grafting Fluorinated Polymer Nanolayer for Advancing the Electrical Stability of Organic Field-Effect Transistors. *Chem. Mater.* **2014**, *26* (22), 6467–6476. https://doi.org/10.1021/cm5030266.
(38) Ward, J. W.; Lamport, Z. A.; Jurchescu, O. D. Versatile Organic Transistors by Solution Processing. *Chemphyschem* **2015**, *16* (6), 1118–1132.
(39) Dhar, J.; Salzner, U.; Patil, S. Trends in Molecular Design Strategies for Ambient Stable N-Channel Organic Field Effect Transistors. *Journal of materials chemistry. C, Materials for optical and electronic devices* **2017**, *5* (3), 744–743.
(40) Ward, J. W.; Loth, M. A.; Kline, R. J.; Coll, M.; Ocal, C.; Anthony, J. E.; Jurchescu, O. D. Tailored Interfaces for Self-Patterning Organic Thin-Film Transistors. *J. Mater. Chem.* **2012**, *22* (36), 19047–19053. https://doi.org/10.1039/C2JM33974A.
(41) DiBenedetto, S. A.; Facchetti, A.; Ratner, M. A.; Marks, T. J. Molecular Self-Assembled Monolayers and Multilayers for Organic and Unconventional Inorganic Thin-Film Transistor Applications. *Advanced Materials* **2009**, *21* (14–15), 1407–1433. https://doi.org/10.1002/adma.200803267.
(42) Wang, H.; Zhu, F.; Yang, J.; Geng, Y.; Yan, D. Weak Epitaxy Growth Affording High-Mobility Thin Films of Disk-Like Organic Semiconductors. *Advanced materials (Weinheim)* **2007**, *19* (16), 2168–2171. https://doi.org/10.1002/adma.200602566.

(43) Ma Feng; Wang Shi-Rong; Li Xiang-Gao; Yan Dong-Hang. Improved Performance of Fluorinated Copper Phthalocyanine Thin Film Transistors Using Para-Hexaphenyl as the Inducing Layer. *Chinese Physics Letters* **2011**, *28* (11), 118501. https://doi.org/10.1088/0256-307X/28/11/118501.
(44) Melville, O. A.; Grant, T. M.; Lessard, B. H. Silicon Phthalocyanines as N-Type Semiconductors in Organic Thin Film Transistors. *Journal of Materials Chemistry C* **2018**, *6* (20), 5482–5488. https://doi.org/10.1039/c8tc01116h.
(45) Rivnay, J.; Mannsfeld, S. C. B.; Miller, C. E.; Salleo, A.; Toney, M. F. Quantitative Determination of Organic Semiconductor Microstructure from the Molecular to Device Scale. *Chem. Rev.* **2012**, *112* (10), 5488–5519. https://doi.org/10.1021/cr3001109.
(46) Kim, C.-H.; Hlaing, H.; Hong, J.-A.; Kim, J.-H.; Park, Y.; Payne, M. M.; Anthony, J. E.; Bonnassieux, Y.; Horowitz, G.; Kymissis, I. Decoupling the Effects of Self-Assembled Monolayers on Gold, Silver, and Copper Organic Transistor Contacts. *Advanced Materials Interfaces* **2015**, *2* (2), 1400384. https://doi.org/10.1002/admi.201400384.
(47) Kim, C.-H.; Hlaing, H.; Payne, M. M.; Parkin, S. R.; Anthony, J. E.; Kymissis, I. Difluorinated 6,13-Bis(Triisopropylsilylethynyl)Pentacene: Synthesis, Crystallinity, and Charge-Transport Properties. *ChemPhysChem* **2015**, *16* (6), 1251–1257. https://doi.org/10.1002/cphc.201402750.
(48) Kim, C.-H.; Hlaing, H.; Payne, M. M.; Yager, K. G.; Bonnassieux, Y.; Horowitz, G.; Anthony, J. E.; Kymissis, I. Strongly Correlated Alignment of Fluorinated 5,11-Bis(Triethylgermylethynyl)Anthradithiophene Crystallites in Solution-Processed Field-Effect Transistors. *ChemPhysChem* **2014**, *15* (14), 2913–2916. https://doi.org/10.1002/cphc.201402360.
(49) Wood, S.; Wade, J.; Shahid, M.; Collado-Fregoso, E.; Bradley, D. D.; Durrant, J. R.; Heeney, M.; Kim, J.-S. Natures of Optical Absorption Transitions and Excitation Energy Dependent Photostability of Diketopyrrolopyrrole (DPP)-Based Photovoltaic Copolymers. *Energy & environmental science* **2015**, *8* (11), 3222–3232.
(50) Wood, S.; Hollis, J. R.; Kim, J.-S. Raman Spectroscopy as an Advanced Structural Nanoprobe for Conjugated Molecular Semiconductors. *Journal of physics. D, Applied physics* **2017**, *50* (7), 73001-.
(51) Tanaka, M.; Young, R. J. Review Polarised Raman Spectroscopy for the Study of Molecular Orientation Distributions in Polymers. *Journal of Materials Science* **2006**, *41* (3), 963–991. https://doi.org/10.1007/s10853-006-6595-7.
(52) Mino, T.; Saito, Y.; Yoshida, H.; Kawata, S.; Verma, P. Molecular Orientation Analysis of Organic Thin Films by Z-Polarization Raman Microscope. *Journal of Raman Spectroscopy* **2012**, *43* (12), 2029–2034. https://doi.org/10.1002/jrs.4118.
(53) Cranston, R. R.; Lanosky, T. D.; Ewenike, R.; Mckillop, S.; King, B.; Lessard, B. H. Polarized Raman Microscopy to Image Microstructure Changes in Silicon Phthalocyanine Thin-Films. *Small Science* **2024**, *4* (6), 2300350. https://doi.org/10.1002/smsc.202300350.
(54) Dindault, C.; King, B.; Williams, P.; Absi, J. H.; Faure, M. D. M.; Swaraj, S.; Lessard, B. H. Correlating Morphology, Molecular Orientation, and Transistor Performance of Bis(Pentafluorophenoxy)Silicon Phthalocyanine Using Scanning Transmission X-Ray Microscopy. *Chemistry of Materials* **2022**. https://doi.org/10.1021/acs.chemmater.2c00277.

(55) Heutz, S.; Cloots, R.; Jones, T. S. Structural Templating Effects in Molecular Heterostructures Grown by Organic Molecular-Beam Deposition. *Applied Physics Letters* **2000**, *77* (24), 3938–3940. https://doi.org/10.1063/1.1332820.
(56) Sakurai, T.; Kawai, S.; Fukasawa, R.; Shibata, J.; Akimoto, K. Influence of 3,4,9,10-Perylene Tetracarboxylic Dianhydride Intermediate Layer on Molecular Orientation of Phthalocyanine. *Japanese Journal of Applied Physics* **2005**, *44* (4R), 1982. https://doi.org/10.1143/JJAP.44.1982.
(57) Wang, Z.; Miyadera, T.; Yamanari, T.; Yoshida, Y. Templating Effects in Molecular Growth of Blended Films for Efficient Small-Molecule Photovoltaics. *ACS Appl. Mater. Interfaces* **2014**, *6* (9), 6369–6377. https://doi.org/10.1021/am405740c.
(58) Zheng, Sonia, Lin; Brusso, J.; Benoît H. Lessard. One-Step Synthesis of Perfluorinated Polyphenylenes Using Modified Ullmann Coupling Conditions. *Synthetic Communications* **2023**, *53* (20), 1730–1738. https://doi.org/10.1080/00397911.2023.2246084.
(59) Harris, R. K.; Becker, E. D.; Menezes, S. M. C. de; Granger, P.; Hoffman, R. E.; Zilm, K. W. Further Conventions for NMR Shielding and Chemical Shifts (IUPAC Recommendations 2008). *Pure and Applied Chemistry* **2008**, *80* (1), 59–84. https://doi.org/doi:10.1351/pac200880010059.
(60) Ren, X.; Qiu, F.; Deng, W.; Fang, X.; Wu, Y.; Yu, S.; Liu, X.; Grigorian, S.; Shi, J.; Jie, J.; Zhang, X.; Zhang, X. Topology-Mediated Molecule Nucleation Anchoring Enables Inkjet Printing of Organic Semiconducting Single Crystals for High-Performance Printed Electronics. *ACS Nano* **2023**, *17* (24), 25175–25184. https://doi.org/10.1021/acsnano.3c08135.
(61) Jiang, Z. GIXSGUI: A MATLAB Toolbox for Grazing-Incidence X-Ray Scattering Data Visualization and Reduction and Indexing of Buried Three-Dimensional Periodic Nanostructured Films. *Journal of Applied Crystallography* **2015**, *48* (3), 917–926. https://doi.org/10.1107/S1600576715004434.

Chapter 4. Conclusion and Future Work

4.1 Thesis Conclusion

The use of MTG for the fabrication of highly ordered semiconductor films with controllable microstructure properties is a promising technique for the fabrication of high performance OTFTs. The synthesis of new molecular templates aids in understanding how structural properties of template layers influence resulting semiconductor films and device performance. This thesis shows the need for the careful selection of materials or pairs of materials used for the fabrication organic electronics. Beyond material selection it is important to optimize the fabrication condition for newly synthesised molecules to yield high performing organic electronics devices.

In **Chapter 2**, the WEG fabrication of R_2-SiPc-OTFTs is first reported using a per-fluorinated *p*-6P (*p*-6PF), moving from the standard literature template layer *p*-6P. The combination of different substrate temperatures during deposition and deposition times of the *p*-6PF enabled the optimization of F_{10}-SiPc OTFT with a maximum μ of 0.14cm^2/Vs with 8 nm *p*-6PF at 100ºC. AFM was used to determine the surface coverage and growth morphologies of resulting films. PXRD was used to correlate crystallinity of F_{10}-SiPc film to *p*-6PF thickness. GIWAXS was used to determine the molecular orientation of F_{10}-SiPc and F_{16}-CuPc using *p*-6P and *p*-6PF. This study shows the superiority of *p*-6PF over *p*-6P as a template WEG of R_2-SiPc in OTFTs.

Chapter 3 builds on the results of **Chapter 2**, focusing on the novel synthesis of template layers (*p*-6PF_4, BBTBP, QPBP, and DFBP) in addition to bare SiO_2, *p*-6P, and *p*-6PF, for the fabrication of F_{10}-SiPc-OTFTs. Maintaining identical deposition conditions for all template layers highlights the impact of the choice of template layer. These findings show the varied electrical performance and crystallinity of F_{10}-SiPc, as determined through PXRD and GIWAXS. Notably, the incorporation of partially fluorinated *p*-6P (*p*-6PF_4) achieved a low V_T of 5.52 V, and *p*-6PF exhibiting the highest μ_e. The results show that increasing fluorine atoms on the template layer enhances the fluorine-fluorine interactions, consequently increasing device μ. Furthermore, polarized Raman spectroscopy is employed to determine the molecular orientation of F_{10}-SiPc films,

revealing that rod-like template layers are more effective in inducing edge-on orientation for WEG-based OTFTs, whereas box structures are better suited for face-on orientations.

Overall, this thesis shows the significance of interface engineering in the development of WEG-based R_2-SiPc OTFTs, particularly in the synthesis and application of novel template layers for understanding the relationships between the semiconductor and dielectric interface. These results have demonstrated the need for deposition optimization of the template layer particularly using substrate temperature during deposition and deposition time to maximize surface coverage and growth morphologies to increase the templating effect on the semiconductor. Beyond, design optimization my results show the differing electrical performances and film properties can arise from the choice of different template layers using identical deposition conditions. This study shows how template layers can be used to induce and control microstructure properties such as crystallinity, molecular orientation, and interface properties for the semiconductor for WEG-based OTFTs.

4.2 Ongoing and Future Work Recommendation

Interface engineering serves as a versatile tool, capable of extending its application beyond BGTC-OTFTs, potentially benefiting various organic electronic devices or OTFTs with different design structures. Apart from the research conducted during my studies, I have identified two areas where the use of WEG-based OTFTs remains relatively unexplored in existing literature. The first relates to the production of organic inverters using WEG-functionalized semiconductors, while the second involves their application in fabricating vertical organic field-effect transistors (VOFETs) which will be further explained in the **Section 4.2.1** and **4.2.2** respectively.

4.2.1 Molecular Templating Growth for Organic Inverters

An organic inverter functions through a tandem connection of two OTFTs. Like its counterpart, the OTFT organic inverter manages input and output voltage signals. Each transistor links to a supply voltage (V_{DD}), while they collectively contribute to an input (V_I) and output voltage (V_O). By arranging the OTFTs in series, various architectures can emerge, including combinations like *n*-type/*p*-type OTFTs, dual ambipolar transistors, or

unipolar transistors (either two *p*-type or two *n*-type).[1] In most cases, the V_{DD} is supplied through the *p*-type OTFT, while the *n*-type OTFT typically grounds its supply source. The transfer characteristics of both OTFTs, in particular their threshold voltage (V_T), determines the output signal of the inverter. The inverter operates in pull-up and pull-down configuration. The *n*-type OTFT acts as the pull-down because its V_O bias is closer to ground than that of the *p*-type OTFT, which acts as the pull-up due to its V_{DD} bias bringing the output voltage (V_O) closer to the supply.[2] However, in organic inverters, symmetry in response to input signals affects performance factors like speed, power consumption, and noise margin necessitating similar transfer characteristics for both *p*-type and *n*-type OTFTs. A study conducted by Yadav demonstrates the use of CuPc and F_{16}-CuPc OTFTs, manufactured on bare SiO_2, for the production of a complementary inverter. The study reports the mobility values of 0.00127 and 0.00033 cm^2/vs for CuPc and F_{16}-CuPc, respectively. Using this method, they successfully produced an organic inverter that achieved a maximum gain of approximately 20.[3] I propose the use WEG-based OTFTs to enhance this work by incorporating *p*-6P, resulting in improved performance of CuPc and F_{16}-CuPc OTFTs, as well as overall higher performance in inverters. In **Figure 4.1**, I demonstrate the use of varying thicknesses of *p*-6P on both CuPc and F_{16}-CuPc to achieve identical transfer qualities in OTFTs, while simultaneously enhancing OTFT performance. Additionally, WEG could be employed to align various semiconductors that typically do not possess similar transfer characteristics. One can potentially accomplish this by employing various template layers and modifying deposition conditions to properly match these transfer properties.

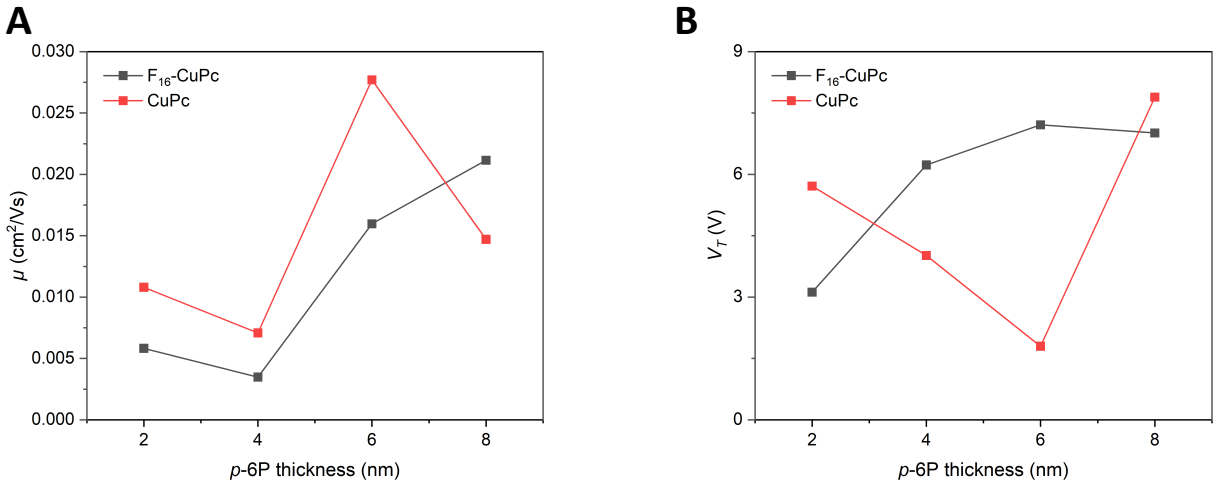

Figure 4.1. *Matching of A) μ and B) V_T of F_{16}-CuPc and CuPc OTFTs using p-6P template layer with different thicknesses at a substrate temperature of 180ºC during deposition. * The V_T for CuPc OTFTs are reported in positive values.*

4.2.2 Molecular Templating Growth for Vertical Organic Field-Effect Transistors (VOFETs)

Based on the results presented in **Chapter 3**, which demonstrates the effectiveness of using a box-structured template to align semiconductors in a face-on orientation, it can be beneficial to consider a change in device architecture towards VOFETs. VOFETs, which operate similarly to OTFTs, with a significant difference in the layout where the semiconductor is placed vertically in between the source and drain electrodes (**Figure 1.6**). This design causes the charge transport to mainly occur perpendicular to the substrate. This unique architectural design enables the reduction the length of the channel to match the thickness of the film.[4] For example, compared to the reported 30 μm channel length of OTFTs in this thesis, a shift to the VOFET architecture shows potential for decreasing the channel thickness to 500 Å, which matches the thickness of the film. This structural arrangement promotes charge transport and is not limited to interactions only at the interface between the semiconductor and dielectric materials. However, it involves a combined interplay of both horizontal and vertical orientations with respect to the said interface.[5] The use of existing box-structured template layers or the creation of new ones could potentially result in a face-on orientation of the semiconductor in VOFETs. This could lead to significantly improved device performance.

Supporting Information

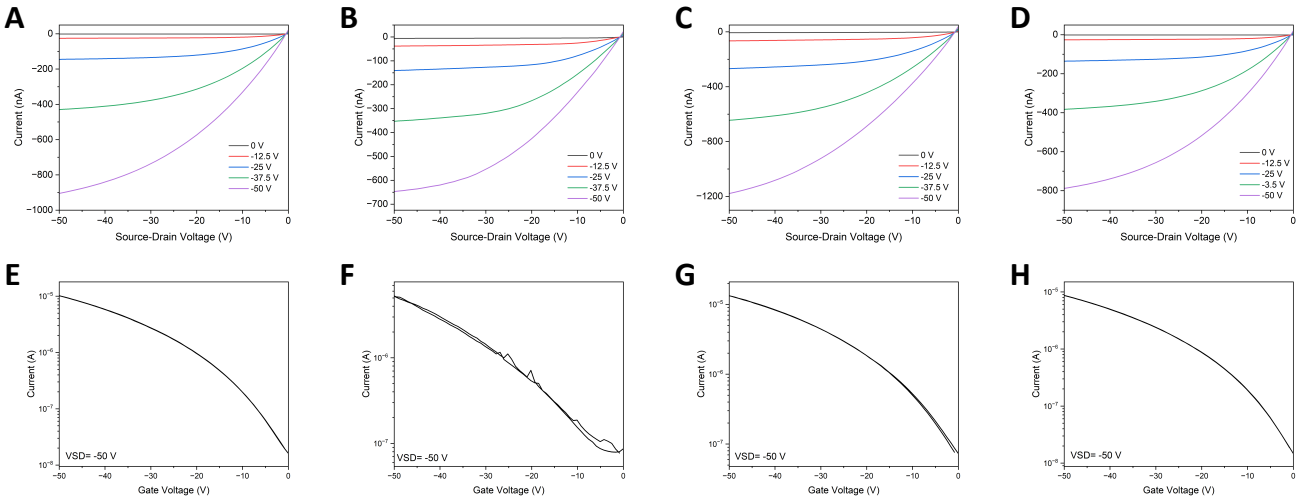

Figure 4.2. *Output curves of CuPc OTFTs on p-6P substrates prepared at 180 °C with thicknesses of A) 2, B) 4, C) 6 and (D) 8 nm, respectively. Corresponding transfer curves for each device are shown in E), F), G) and (H).*

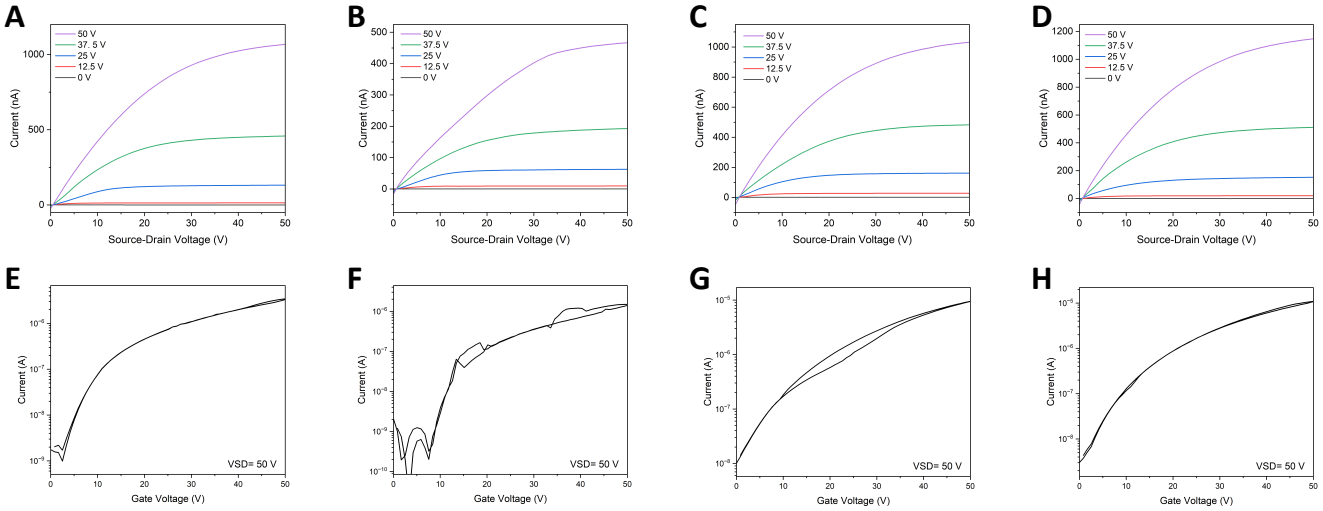

Figure 4.3. *Output curves of F_{16}-CuPc OTFTs on p-6P substrates prepared at 180 °C with thicknesses of A) 2, B) 4, C) 6 and (D) 8 nm, respectively. Corresponding transfer curves for each device are shown in E), F), G) and (H).*

References

(1) Leydecker, T.; Wang, Z. M.; Torricelli, F.; Orgiu, E. Organic-Based Inverters: Basic Concepts, Materials, Novel Architectures and Applications. *Chem. Soc. Rev.* **2020**, *49* (21), 7627–7670. https://doi.org/10.1039/D0CS00106F.
(2) Yadav, S.; Ghosh, S. Fabrication of Organic Complementary Inverter; SPIE, 2012; Vol. 8549, pp 854931-854931–854933.
(3) Kumar, B.; Kaushik, B. K.; Negi, Y. S. Static and Dynamic Analysis of Organic and Hybrid Inverter Circuits. *Journal of Computational Electronics* **2013**, *12* (4), 765–774. https://doi.org/10.1007/s10825-013-0476-5.
(4) Liu, J.; Qin, Z.; Gao, H.; Dong, H.; Zhu, J.; Hu, W. Vertical Organic Field-Effect Transistors. *Advanced Functional Materials* **2019**, *29* (17), 1808453. https://doi.org/10.1002/adfm.201808453.
(5) Kleemann, H.; Krechan, K.; Fischer, A.; Leo, K. A Review of Vertical Organic Transistors. *Advanced Functional Materials* **2020**, *30* (20), 1907113. https://doi.org/10.1002/adfm.201907113.